ASDEX - UG

ASDEX Upgrade Project Proposal

Phase II

ASDEX Upgrade Project Team

IPP 1/217 Mai 1983

MAX-PLANCK-INSTITUT FÜR PLASMAPHYSIK

8046 GARCHING BEI MÜNCHEN

MAX-PLANCK-INSTITUT FÜR PLASMAPHYSIK

GARCHING BEI MÜNCHEN

ASDEX - UG

ASDEX Upgrade Project Proposal

Phase II

ASDEX Upgrade Project Team

IPP 1/217 Mai 1983

Die nachstehende Arbeit wurde im Rahmen des Vertrages zwischen dem Max-Planck-Institut für Plasmaphysik und der Europäischen Atomgemeinschaft über die Zusammenarbeit auf dem Gebiete der Plasmaphysik durchgeführt.

6. Mai 1983

A S D E X - U G

ASDEX Upgrade Project Proposal

Project Team:
Köppendörfer,Blaumoser,O.Gruber,J.Gruber,Jandl,Kluger,
Kollotzek,Kotzlowski,Krause,E.Lackner,K.Lackner,Martin,
Neuhauser,Pillsticker,Preis,Röhr,Ryll,Schneider,Seidel,
Springmann,Streibl,Vernickel,Werner,Wunderlich

Contributions from other IPP groups:
Brambilla,Croci,Parmeyer,Haubenberger,Kottmair,Kutsch,
Mahl,Poschenrieder,Söll,Wesner

Contributions from outside IPP:
KfA Jülich: Kaleck
TU Stuttgart: Salzmann,Wilhelm
FOM/Nieuwegein : Braams

ASDEX Upgrade Project Proposal

Application for EURATOM Preferential Support Phase II

1. Introduction

The needs for and the justification of an ASDEX Upgrade (ASDEX UG) as a follow-up experiment to ASDEX were described in the application for EURATOM Preferential Support Phase I /1, 2/. The objective of ASDEX UG is to investigate the problems relating to tokamak divertor physics and the boundary layer of hot plasmas which cannot be covered otherwise by either ASDEX or other EUROPEAN tokamaks, including JET, but whose investigation is indispensable for NET and INTOR /3/. The ASDEX UG project extends the ASDEX poloidal divertor experiment in essentially two directions: With regard to the poloidal configuration and with regard to the plasma parameters. Both are necessary in order to meet reactor requirements.

ASDEX has shown that it is at least the closed poloidal divertor which has clearly the potential to guide the particle and energy fluxes in a way to the material environment in which impurity sources are sufficiently reduced so that clean plasmas can be produced even for megawatt heating powers. This identifies the possibility to sufficiently reduce the wall erosion of fusion reactors by sputtering which would otherwise be unacceptable.

The configuration of ASDEX UG is changed as compared with ASDEX. This is due to the requirement that all poloidal field (PF) coils are located outside the toroidal field (TF) magnet. This leads to a highly elongated D-shaped plasma with an "open" divertor, which does not allow to close the divertor chamber by such simple means as in ASDEX. The elongated plasma is vertically unstable and provisons have to be taken to stabilize the plasma. As shown in the INTOR study, this is the only configuration which promises sufficient reactor potential, and therefore an experimental investigation of these problems is mandatory.

The plasma parameters are extended in order to ensure a sufficiently high plasma density and temperature and a reactorlike energy flux density from the plasma, which in this case is provided by sufficient auxiliary heating. Enhancing the plasma current of ASDEX UG by up to a factor of 4 as compared to ASDEX makes it possible to both increase the line density and the temperature at the poloidal β-limit by about a factor of 3.

Calculation of double null (DN), single null (SN) and limiter controlled (L) configurations have produced SN configurations which are very similar to L configurations with respect to the multipole currents required. These are both in contrast to the DN configuration which requires higher multipole currents.

The technical concept as originally defined by the so-called reference system /1/ was developed further during the last year. Recent results and a better understanding of the divertor function, the plasma boundary layer and the poloidal field geometry allowed modifications to be made which led to great simplifications /2/.

Using the experience of competent manufacturers, it was possible to make sure that the technical solution and design concepts of major components are feasible.

In the following section 2, the aims of ASDEX UG are repeated briefly and the essential features and parameters of the tokamak system are summarized. The concept described is the result of a continuous and iterative optimization procedure and it is to be regarded as the simplest, smallest and least expensive system with respect to the aims and physical and technical boundary conditions. The summary of section 2 includes an overview of the tokamak design, the time schedule of design and construction concluding with the estimated investment cost and manpower required.

In section 3 the tokamak system components are treated. The circuits and energy supply for the different electrical components are described in section 4.

Auxiliary heating requirements and methods are discussed in section 5. Section 6 presents a survey over the periphery of the tokamak system including preparation of the building and radiation shielding. Section 7 outlines the physical programme. Section 8 is devoted to diagnostics. Finally, the principal concepts for control, data acquisition and handling are outlined in section 9.

2. Summary of the Asdex UG Project Proposal

2.1 Definition of the Concept

2.1.1 The aims

The aims of ASDEX UG cover essentially all plasma boundary and first wall problems which can be investigated by discharges without thermonuclear heating. In particular they encompass:

(a) the study of plasma boundary problems of a fusion reactor associated with the

- transfer of the energy flux to the walls;
- control of wall-produced impurities;
- investigation of the helium pumping problem;

(b) the utilization of the improved impurity and plasma density control of divertor configurations

- to study the confinement properties of clean, separatrix-bound plasmas in the high-current regime;
- to study long pulses and current drive;

(c) the provision of a sound basis for the final decision on the NET concept, in particular whether a pump limiter solution suffices or whether a divertor is needed and how it has to be designed.

Plasma boundary layer studies should compare different promising solutions for the energy transfer and impurity balance problems like

- high-density scrape-off layer with protection of the target plates by a zone of intensive localized recycling;
- a hot boundary layer in front of a low-Z-coated pump

limiter taking the major fraction of the energy flux, with nearly unattanuated sputtering but sufficiently small impurity confinement time;

- a radiation zone formed by a saturated concentration of medium-Z impurities forming a protective cold plasma mantle in front of limiter and walls ("photosphere");

and examine whether a high enough neutral helium density can be achieved in the pumping chamber of a poloidal divertor and a toroidal pump limiter for efficient ash removal.

Passively stabilizing elements inside the main field coils and active feedback on PF coils outside the toroidal field coils will be provided to test and demonstrate the control needs of a divertor and toroidal pump limiter. This stabilizing method shall be optimized in conjunction with configurational changes, in particular the triangular distortion.

The favourable properties of a poloidal divertor demonstrated by ASDEX shall be utilized also for a study of plasma confinement, heating and current drive. In particular, we will pursue the studies of the so-called H regime found in ASDEX into the regime of plasma currents, densities and temperatures allowing a comparison with the results of non-divertor devices like JET, TFTR and TORE-SUPRA. The parameter space may be extended this way into confinement regimes inaccessible or difficult to reach for limiter-bound devices. The understanding of the basic features of these regimes may, hopefully, also benefit the pump limiter concept and even indicate a way for realizing it.

Theories and experiment for extremely long pulse or current drive scenarios indicate the importance of a control of plasma and impurity density like can best be achieved in a divertor tokamak. By having (from power supply and cooling of TF and PF coils) the potential for pulse lengths of several minutes for plasma currents in the range of present ASDEX values (500 kA) ASDEX UG should serve as test bed for further such studies.

2.1.2 Requirements and Definition of the Concept

The D-shaped plasma produced by multipole coils outside the TF magnet requires a vertically elongated vacuum chamber in order to incorporate divertor structure and target plates in addition to the D-shaped plasma. D-shaped TF coils were the appropriate choice to fit the chamber and to facilitate force support.

The required plasma parameters, as described in the

application for EURATOM priority support phase I /1/, of $\bar{n}_e a = 7.5 \cdot 10^{19} m^{-2}$, in order to provide for a sufficiently dense plasma boundary, and a sufficiently high plasma temperature in order to model the gradient $\langle T \rangle / a$ in the boundary layer, lead, for the critical density limit, to a certain minimum ratio of the magnetic field on axis over the aspect ratio. The choice of a reactor-like average density $\bar{n}_e = 2.2 \cdot 10^{20} m^{-3}$, as deduced from reactor studies, yielded a small plasma radius of a = 0.50 m. The line density, temperature and gradients of the plasma boundary should thus be reactor-like even representing the binary collision properties in the radial dimension. ASDEX UG is by this choice only slightly bigger in dimension than ASDEX.

The multipole coil system symmetric to the torus equatorial plane allows to produce poloidal flux configurations which extend from double null (DN) to single null (SN) and limiter (L) controlled configurations. Figure 2.1 shows poloidal flux surfaces for the three typical cases including the multipole currents for a plasma current of I = 1 MA. The total ampere turns of the multipole field system differ little between the single null and limiter configuration. The double null, however, requires about three times as much for equal plasma current. All configurations are vertically unstable, the driving force close to the plasma and feedback control of the multipole currents shall stabilize the plasma.

The attainable plasma currents and their duration which ultimately determine the attainable critical density and temperature - at the poloidal beta limit - differ between the three configurations. They are limited by several constraints: by the stresses exerted in the TF coils, by the poloidal field components, by the OH flux swing and the generator power supply. The limiting values are discussed further below.

For providing the reactor-like power flux density in the plasma boundary of ~ 0.3 MW/m^2, an auxiliary heating power of 12 MW is required into the plasma. Several heating methods are being investigated. However, preference is given to 2. harmonic ICRH for several reasons given in ref. /1/. The heating power needed for reaching the poloidal beta limit at the critical density depends on the yet unknown energy confinement properties of the hot ASDEX UG plasma. Applying the ALCATOR scaling, the Baltimore ($\propto I_p$) H discharge scaling and finally the Baltimore scaling in the L discharge regime yield for the heating power 7.5 MW, 8.7 MW and 17 MW for reaching these limits. This indicates that the 12 MW power or the 0.3 MW/m^2 power flux density are an appropriate value in accordance with experimental findings.

This power should be available for relevant parameters up

to 10 seconds. The vacuum vessel was designed with respect to the ports to be compatible with all heating methods conceivable. Those are: ICRH, neutral injection heating, LHRH and ECRH. The antenna design and computation as well as the definition of a generator development programme in industry has been started for 2. harmonic ICRH. The university of Stuttgart is exploring the possibility of using ECRH. With regard to LHRH, positive results from ASDEX would be needed to put more effort into this heating method. A particle energy of 80 keV for perpendicularly injected neutral hydrogen, as required for central deposition at $\bar{n}_e a = 7.5 \cdot 10^{19}\ m^{-2}$, leads to consider this heating method as fall back solution only.

Although preference is given to ICRH, the experimental progress is carefully observed in the area of all heating methods mentioned and the technical requirements considered along the design of the ASDEX UG tokamak system. The decision on the proper heating method does not need to be taken prior to the end of 1984.

Beside the physical requirements and constraints the size and magnetic field of ASDEX UG were determined by the choice of 25 MA/m average current density in the water-cooled copper conductors of TF and PF coils for maximum excitation. The essential part of the optimization, as decribed in ref./1/, was to minimize the aspect ratio A.

In table I, the basic machine dimensions and parameters are given. The values are maximum values for each component.

Table I: Main Plasma and Machine Parameters

Large plasma radius	R_o	1.65 m
Minor plasma radius	a	0.5 m
Plasma height	b	0.8 m
Plasma elongation	s=b/a	1.6
Plasma aspect ratio	A	3.3
Plasma current	I_p	2 MA
Toroidal magnetic field	B_o	3.9 T
OH flux swing		9.5 Vsec
Discharge duration (for I =0.5 MA: 2 min)	t_D	10 sec
Recess betw. discharges	t_C	10 min
Plasma line density at density limit (I_p=1.6 MA)	$\bar{n}_e a$ =	$7.5 \cdot 10^{19}\ m^{-2}$
Average plasma temperature at density limit and and β_p-limit (I_p=1,6 MA)	$\bar{T}_i = \bar{T}_e$	3.5 keV

Peak plasma temperatures		7 keV
Max. power flux density to the walls	P_w	0.3 MWm^{-2}
Auxiliary heating power	P_H	12 MW

Table II describes the reference modes of operation for DN, SN and L including the discharge durations attainable with the existing generator power supply.

Table II: The Operational Regimes of ASDEX UG

Shearing stress limit on TF coil 20 MPA
SN single null discharge
DN double null discharge
L limiter-operated discharge
CD long pulse (current drive) discharge

	SN	DN	L	CD
$I_p \cdot B_o$ (MAT)	4.5	3.9	6.5	--
I_p (MA)	1.6	1.2	2	0.5
B_o (T)	2.7	3.25	3.25	1
q_a	2.2	3.5	2.1	2.6
T_D (sec)	7	5	5	120

During the conceptual design of ASDEX UG the multipole field system turned out to be the limiting component because of its excessive power consumption. However, an optimization of the current distribution in the V1, V2 and V3 multipole field coils allowed to find a single null configuration, with the axis being shifted out of the equatorial plane, which differs little only in total multipole current from the limiter-controlled configuration (Fig. 2.1). This seemed to prove that a single-null divertor tokamak is comparably suited for a reactor than an equally elongated limiter plasma.

However, the force load on the TF coils exerted by the poloidal field and hence the stresses turned out to differ considerably between SN on one side, and DN and L configuration, on the other. The combination of symmetric and antimetric forces in the SN case yielded critical shear

stresses close to the central support region, which are strongly reduced under the antimetric load of the DN and L configuration.

The attainable toroidal fields and plasma currents are now, due to these shear stresses, defined by $I_p \cdot B_o \leq 4.5$ MAT for the SN configuration. The safety factor q then determines the particular value of I_p and B_o. For $q_a = 2.2$, a current of $I_p = 1.6$ MA can be realized. This is a 20 per cent smaller value than anticipated in the supplement /2/ to the proposal for application for EURATOM priority support phase I. Since the 2 MA exceeded the physically required value anyway, the physical objective of ASDEX UG is still fully covered by $I_p = 1.6$ MA.

Also the multipole field coils required ample support structure in order to balance the vertical forces. The ohmic heating coils consisting of the central OH 1 transformer coil and two stray flux shaping coils OH 2 and OH 3, were integrated into this support structure.

Figure 2.2 shows the design concept of ASDEX UG. It differs decisivley from ASDEX, although the dimensions are comparable, mainly by the following facts: a by a factor of 1.4 increased toroidal field, a 2.5 to 4 times increased plasma current - mainly on account of a 2.5 times enlarged plasma cross-section, and the increased toroidal field - and finally by the measure to put the multipole and OH coils outside the TF coils. The required sizeable structure which leaves the minimum acceptable space for the required ports and openings, gives evidence of a - with respect to force balance - optimized design.

2.2 Overview of the Design and the Components

2.2.1 The Toroidal Field (TF) Magnet

The toroidal field magnet consists of 16 D-shaped coils whose straight wedge-shaped inner legs form a vault for central force support. A spherical steel shell structure is embedding the outer legs of the D in order to balance lateral forces like overturning moments. This structure has, in principle, 16-fold symmetry. Shear bolts connect the sectors of the support structure. The toroidal field ripple at the plasma outer edge, produced by 16 coils, does not exceed 1.6 per cent.

The individual double pancake coil carries no casing. Three cooling channels in each conductor with a connection length of two windings allow steady-state excitation up to B_o

= 3.0 T at a water velocity of 9 m/sec .

The vault support, first chosen in order to minimize the aspect ratio, turned out to be necessary for smooth distribution of stresses produced by bending and twisting moments in the free part of the coil due to the poloidal field components of the SN and DN configurations.

The admissible machine parameters are determined by the stresses at the edge of the vault support. In the SN configuration torsion moments produce shearing stresses at the vault edge which are proportional to $I_p \cdot B_o$. Limiting those to $\leq$ 20 MPA requires the already quoted operational regime of $I_p \cdot B_o \leq 4.5$ MAT.
In the DN configuration the combined bending and tensile stresses are limiting which show a more involved dependence on I_p and B_o . But with the choice of $I_p \cdot B_o \leq 3.9$ MAT a safe operational regime could be defined. The choice of the safety factor then determines the actual plasma current and toroidal field values. Figure 2.3 shows the regime accessible within these stress limits for SN and DN discharges. The TF magnet stresses do not limit the I_p and B_o values for L discharges.

The TF magnet is modular in octant symmetry. However, assembly and disassembly are determined by the vacuum vessel symmetry which consists of quadrants. The assembly concept is discussed in section 3.4.

2.2.2 The Poloidal Field System

The PF system (Fig. 2.2) consists of the ohmic heating (OH) system and the multipole (V) coil system. From the beginning the aim was not to concatenate TF and PF systems geometrically but to put all PF coils outside the TF magnet instead. Sophisticated coil concepts were also discarded and simple water-cooled copper conductors chosen, wound with fibre glass tape and impregnated with epoxy resin.

The OH coil system is composed of three coils, the central air core transformer coil OH 1 and two stray flux shaping coils OH 2 and OH 3. The stray field in the plasma region was thus reduced to $B_s \leq 3 \cdot 10^{-3}$ T in order to allow breakdown already for 10 V loop voltage. The OH 1 solenoid is designed for a total flux swing of $\Phi_{OH} = 9.5$ Vsec. The ratio Ri/Ra 0.5 of the OH 1 radii keeps radial tensile stresses low. No force load of the TF coils acts on the OH 1 cylinder because those are by the vault self-supporting.

The multipole field (V) coils are arranged symmetrically to the equatorial plane and dimensioned for the maximum required coil currents and 25 MA/m^2 current density. Their position is optimized with regard to the plasma

configuration and minimum coil currents and, hence, minimum power losses.

The radial forces are balanced by hoop stresses in all coils. The large vertical forces, however, have to be taken up by a supporting frame with 16 radial beams, which embraces all coils. It requires a heavy steel bolt in its centre, through the bore of the OH 1 coil. The support bed for the coils has to provide sufficient area for vertical forces of up to 2.3 MN/m for the V 1 coil, 1 MN/m for the V 2 and 0.5 MN/m for the V 3 coil.

The required multipole currents can exceed at low beta those necessary at high beta for equal plasma current. To avoid this excessive current load, the plasma current and beta is simultaneously ramped up during the heating phase.

The multipole coil design considered the possibility of exchanging the multipole coils in the upper half by superconducting coils in a later stage of the experiment. The Kernforschungszentrum Karlsruhe (KFK) is presently starting a development project for superconducting poloidal field coils for ASDEX UG and TORE SUPRA. Both experiments should serve as realistic boundary conditions for such a development which is required for NET and other future devices. In case of ASDEX UG the discharge duration can then be extended because of the reduced power consumption of a tokamak system with superconducting poloidal field coils. However, it should be emphasized that the physical programme of ASDEX UG can be carried through with normal conducting PF coils.

2.2.3 Vacuum Vessel and its Interior Structure

The vacuum vessel system can be divided into the basic vessel structure, including ports, and into interior installation which serves several purposes. The basic vessel system is symmetric to the torus equatorial plane. According to the discharge programme (sec. 2.2.5), the first installation is designed for SN operation with the X-point in the lower half of the torus.

The vacuum vessel had to be adjusted to several requirements: to balance the force loads, especially by plasma disruptions, to provide sufficient toroidal resistance, to withstand the power flux density from the plasma, to allow sufficient ports for pumping, heating and diagnostics and to incorporate proper divertor structure. The rigid steel vessel is 16-fold polygonal with the edges being located under the TF coil legs. It is devided by 4 separation planes for assembly and disassembly and by four insulation planes.

The disruption shearing forces of up to 0.7 MN/m are taken up by formlocked flange connections. The insulated connection is protected from the plasma side by steel bellows which determine the 0.25 m Ω toroidal resistance. 8 ports of 0.4 x 0.8 m^2 in the equatorial plane and numerous smaller ports are foreseen. Since the original proposal the pumping of the divertor has been improved by providing 16 ports of 0.25 m diameter in each divertor half plane.

A large part of the vessel surface is covered by an actively cooled heat shield. The first installation is adjusted to SN operation with X-point in the lower half of the torus. The target plates and shields are positioned to reduce the heat load and facilitate pumping. The structure in the upper half of the torus is designed to give room for the SN plasma opposite the X-point but to allow also for limited heat flux DN plasma configurations.

Passive loops (Fig. 2.4) close to the plasma can vertically stabilize the plasma for up to about 200 m sec. A 0.15 m axial plasma shift produces a total load of 0.6 MN on the stabilizing conductors. Since the design considerations showed no clear solution up to now whether this force can be supported by the vacuum vessel, 4 beams connected to the PF support frame through 4 large ports, were chosen as a safe support concept. A development programme for heat shield and target plates is presently being carried through with industry. It concerns the water-cooled stainless steel structure eventually covered by graphite plates or other material.

An ICRH antenna system has been preliminarily designed and will be subject of a separate proposal for EURATOM priority support on auxiliary heating. This antenna system, consisting of 16 short single antennae, arranged in pairs at 8 locations along the toroidal circumference, has been integrated into the vacuum vessel. Calculations of both the antenna-to-plasma coupling and antenna matching and of the thermal load on the antennae have shown that the requirements imposed can be met with this system.

The divertor and the main chamber is pumped through 16 ports which provide a pumping speed of 1500 l/s each. A 10,000 l/s cryopump is installed at one main port for pumping vapours during glow discharge cleaning. The distribution of horizontal, vertical and inclined ports was designed compatibly with the diagnostic needs and in respect of the necessary TF coil support structure.

2.2.4 The Auxiliary Heating Concept

A preliminary analysis of auxiliary heating has revealed that the heating method should meet the following requirements:

- central deposition within the plasma;
- edge heating of the plasma should be avoided;
- applicability in a wider plasma parameter range; (e.g. $\omega_{pe} > \omega_{ce}$);
- high generator efficiency;
- applicable from the low field side.

ICRH at the 2. harmonic was found to be the heating method which fits best these requirements, which is technically sufficiently developed and which has been successfully tested in heating plasmas up to MW heating power.

The ICRH system of generators, transmitters and antennae shall be subject of a separate application for preferential support.

The frequency range $80 \leq f \leq 120$ MHz is defined by the plasma parameter regime as determined by the toroidal field $2.7 \leq B_o \leq 4$ T. This choice fits essentially an industrial development programme for ASDEX and W VII of 1.5 MW generator stages tuneable up to 100 MHz. The antennae calculated and designed for ASDEX UG compatibility with the vacuum vessel are described in Section 4.1.

Ray tracing calculations have been carried through for cold and warm plasmas showing a good focussing of the wave fronts towards the plasma center - location of the 2. harmonic resonance frequency - and absorption more or less localized at the center depending on the plasma temperature (Fig. 2.6).

The power of 12 MW is launched by 8 single antennae each consisting of two identical dipoles above and below the equatorial plane with a power capability of 1 MW per dipole.

Although ICRH was chosen as the appropriate heating method for ASDEX UG other heating methods have been considered as fall back solutions. Care has been taken that the vacuum vessel and port openings are compatible with each of these methods. These are, in order of priority,

- neutral injection (NI) by hydrogen with a beam particle

energy of 80 keV per box, 2 NI boxes, 5MW per box, injection angle close to 90 deg.;

- LHRH, 2.45 GHz, 40 cyclotrons, 12 MW;
- ECRH, 2. harmonic 150 GHz for B_o = 2.7 T, $n_e \leq 3 \cdot 10^{20}$ m^{-3} launched from the low field side.

Central power deposition by neutral injection heating requires for ASDEX UG at $\bar{n}_e a = 7.5 \cdot 10^{19}$ $\bar{m}^2$ hydrogen beams of 80 keV particle energy. The JET neutral injection system would fit therefore the ASDEX UG needs. Two JET injection boxes of 5 MW power output each could be used. However, the poor overall efficiency of sources in this energy range would demand 40 MW input power for each box. The power fraction in the low energy components (40 keV, 27 keV) could also lead to unacceptable plasma edge heating.

Helium injection at 40 keV particle energy for heating would provide considerably higher neutralization efficiency ($\sim$50%) and cause no problems with particles at low energy. The particle flux of $\Phi_{He} \approx 10^{19}$ sec , required for 10 MW heating power, however, would lead to a replacement of the hydrogen plasma by helium after about 2 seconds, since the helium is not pumped by the walls.

LHRH for heating is restricted to a limited parameter range because of fixed frequency and density limits depending on the toroidal field value. No evident experimental results encourage to choose this method although forthcoming results may change this situation.

ECRH heating with the ordinary wave from the low field side is by its relative physical simplicity an attractive method; however, applicable for $\omega_{pe} < \omega_{ce}$ only. Second harmonic heating in ASDEX UG at the low toroidal field limit B_o = 2.7 T requires a frequency of f = 150 GHz. A 150 GHz gyrotron development programme is planned by EURATOM at present. The fixed frequency of the gyratron limits the parameter margin of the experiment considerably in contrast to the tuneable ICRH generators.

2.2.5 Comments on the Discharge Programme

The configurational margin and the parameter regime have already been described in Section 2.1.2. The total number of discharges is limited by the design requirement of 20,000 full load discharges and 1,000 hard disruptions.

Hydrogen has to be the filling gas for the majority of discharges. For the maximum temperature at the critical density for I_p = 2 MA about 300 discharge seconds in deuterium would be permissible until the activation of the

vessel structure would reduce the hands on time to an unacceptable value. The neutron flux density for I_p = 2 MA and full plasma parameters requires a shielding of 2.1 m thick concrete walls and a 1.8 m thick - e.g. wooden - ceiling. If the deuterium discharges are limited in their parameters to $\bar{T}_i \lesssim 1$ keV; $\bar{n}_e \lesssim 10^{20}$ m^{-3}, concrete walls of 1.2 m and a wooden ceiling of 0.9 m thickness would suffice. 1.2 m thick concrete walls are required anyway for hard x-ray shielding The design for the building modifications covers both possibilities.

SN, DN and PL (pump limiter) discharges at full performance are not compatible with one and the same vacuum vessel installation and pumping arrangement. The primary objective is certainly the SN configuration. The use of DN configurations in a reactor is hardly conceivable because of their large poloidal field system effort and the inefficient use of the vacuum chamber by the plasma. In an experiment, however, the DN configuration is still of interest because it allows to produce plasmas symmetric to the equatorial plane and to separate the inner and outer scrape-off layer.

The discharge programme foresees therefore to equip the vacuum vessel from the beginning on with all structure adjusted to the single null configuration. This is in particular:

- target plates, aperture plates and heat shields at the vessel bottom adjusted to the SN flux pattern and the expected power flow;

- antennae contours and protection structure adjusted to the unsymmetric SN flux surfaces;

- passive stabilizing loops optimized in position and time constant to the unstable SN configuration;

- vacuum pumps concentrated at the bottom part of the torus.

Remote target plates in the upper torus allow DN configurations with reduced discharge duration or with reduced parameters.

2.2.6 Manufacturing Procedure and Time Schedule

In the conceptual design phase industrial know-how and experience were utilized by placing study contracts and material tests for the essential components. More conventional items like support structure were discussed with specialists of manufacturing companies. Realistic estimates on construction time schedule and costs could thus be obtained. The TF coils, in design similar to the JET

coils, were investigated by BBC and optimized with respect to fabrication in close cooperation with the IPP engineering group. The detailed design of the poloidal field coils (OH and V coils) is presently being worked out by three competent European producers after the functioning of the concept has been assured by common discussions. The structural shell of the TF coils was discussed with six steel and cast iron producers. This way the advice of industrial experts entered already during the design phase.

Figure 2.6 shows the ASDEX UG construction time schedule which assumes EURATOM priority phase II approval in the second half of 1983. The fabrication period would thus extend from 1984 into the year 1986, in which assembly of the system should be conducted. Preparation of the experimental building L6 starts also shortly after approval by the EURATOM boards. This time schedule is essentially assured by the choice of simple component design and the choice of a conventional and proven tokamak component technology.

2.2.7 Cost Estimates

The cost estimate is based on preliminary cost evaluation by producers (TF coils, TF magnet support structure) on comparison with the costs of comparable tokamak components already produced (e.g. for JET, ASDEX and others) and by material prices. In case a certain margin resulted within the price estimates, the upper limit was taken.

Figure 2.7 shows the cost distribution over the years of design and construction, reaching a total sum of 96 MDM, the costs for auxiliary heating being subject of a separate proposal. 59 MDM will be spent until 1986, the current financial period, the rest of 37 MDM until 1989.

2.2.8 Manpower

The manpower involved in the ASDEX UG project consists of the engineering design team, of experts from the IPP central technical services and other groups and of manpower hired from industry. The IPP effort in professionals, i.e. the design team and the manpower of engineers and physicists from other IPP groups, is shown in Fig. 2.7. Here three curves are given. Curve 1 represents the professionals inside or outside the construction team who fulfill specific long-term tasks for the construction of the experiment. Curve 2 summarizes the professional manpower in support of the first group. Curve 3 adds the manpower envisaged for the development and construction of the diagnostics. The total manpower for the first group amounts to 130 MY, for the support staff to 40 MY, and for diagnostics to 80 MY, totalling 250 professional MY for the construction of ASDEX

UG. These are backed up by about 450 MY from the technical staff available at IPP. Engineering support from outside IPP is not included here.

Collaboration with several European and other international institutions, especially in the field of development of diagnostics, is presently arranged and will be subject of a separate paper.

References:

/1/ ASDEX Upgrade, Definition of a tokamak experiment with a reactor-compatible poloidal divertor, IPP-Garching report 1/197, March 1982.

/2/ Supplement to "ASDEX Upgrade, Definition of a tokamak experiment with a reactor-compatible poloidal divertor", IPP-Garching report 1/211, November 1982.

/3/ Tokamak Symposium Schliersee, FUR FU 82/CCFP-PC8/3b, November 1982.

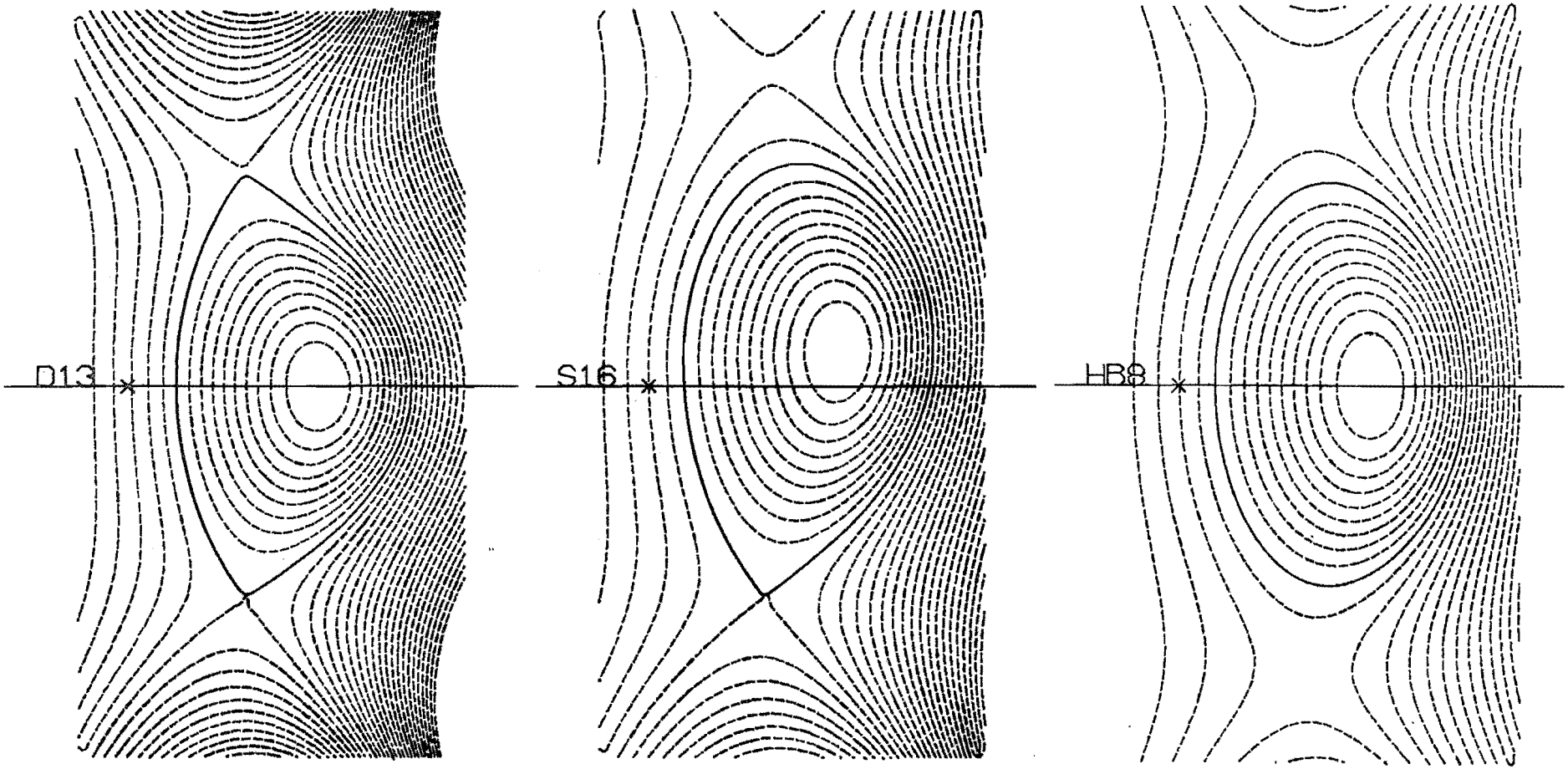

Fig. 2.1: Double null, single null divertor and limiter-controlled configurations for ASDEX UG produced by PF coils located outside the TF magnet.

$\Sigma|I_M| = 12.4 I_p$ $\Sigma|I_M| = 5.5 I_p$ $\Sigma|I_M| = 3.6 I_p$

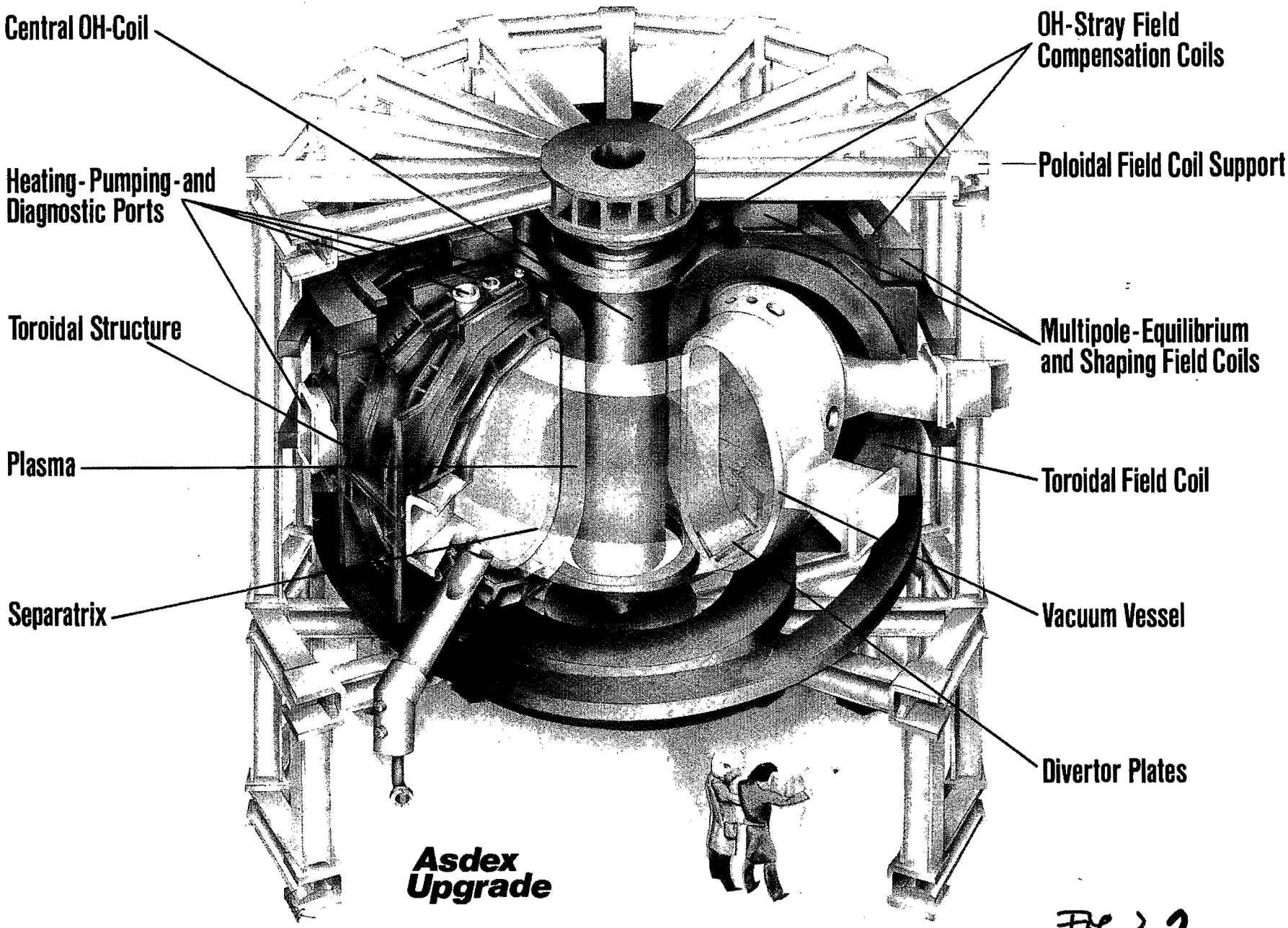
Central OH-Coil
Heating-Pumping-and Diagnostic Ports
Toroidal Structure
Plasma
Separatrix
OH-Stray Field Compensation Coils
Poloidal Field Coil Support
Multipole-Equilibrium and Shaping Field Coils
Toroidal Field Coil
Vacuum Vessel
Divertor Plates
Asdex Upgrade

Fig 2.2

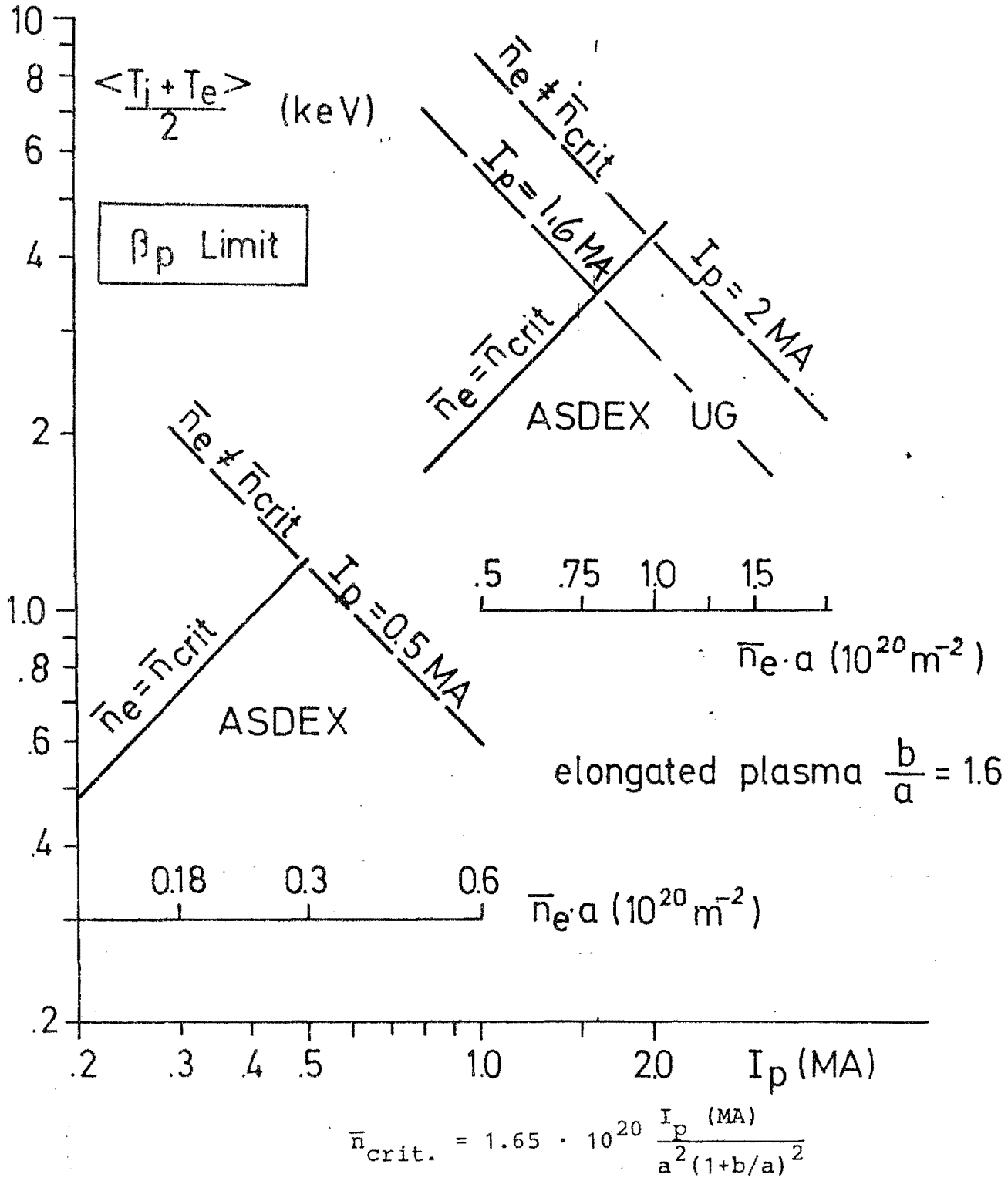

Fig. 2.3 Attainable temperatures at the β_p-limit ($\beta_p = \sqrt{A}$) for ASDEX and ASDEX UG at the Hugill density $n_{crit.}$ limit (solid line) for different plasma currents. The dashed lines give the temperature for fixed $I_{p\ max}$ but $n_e \neq n_{crit}$.

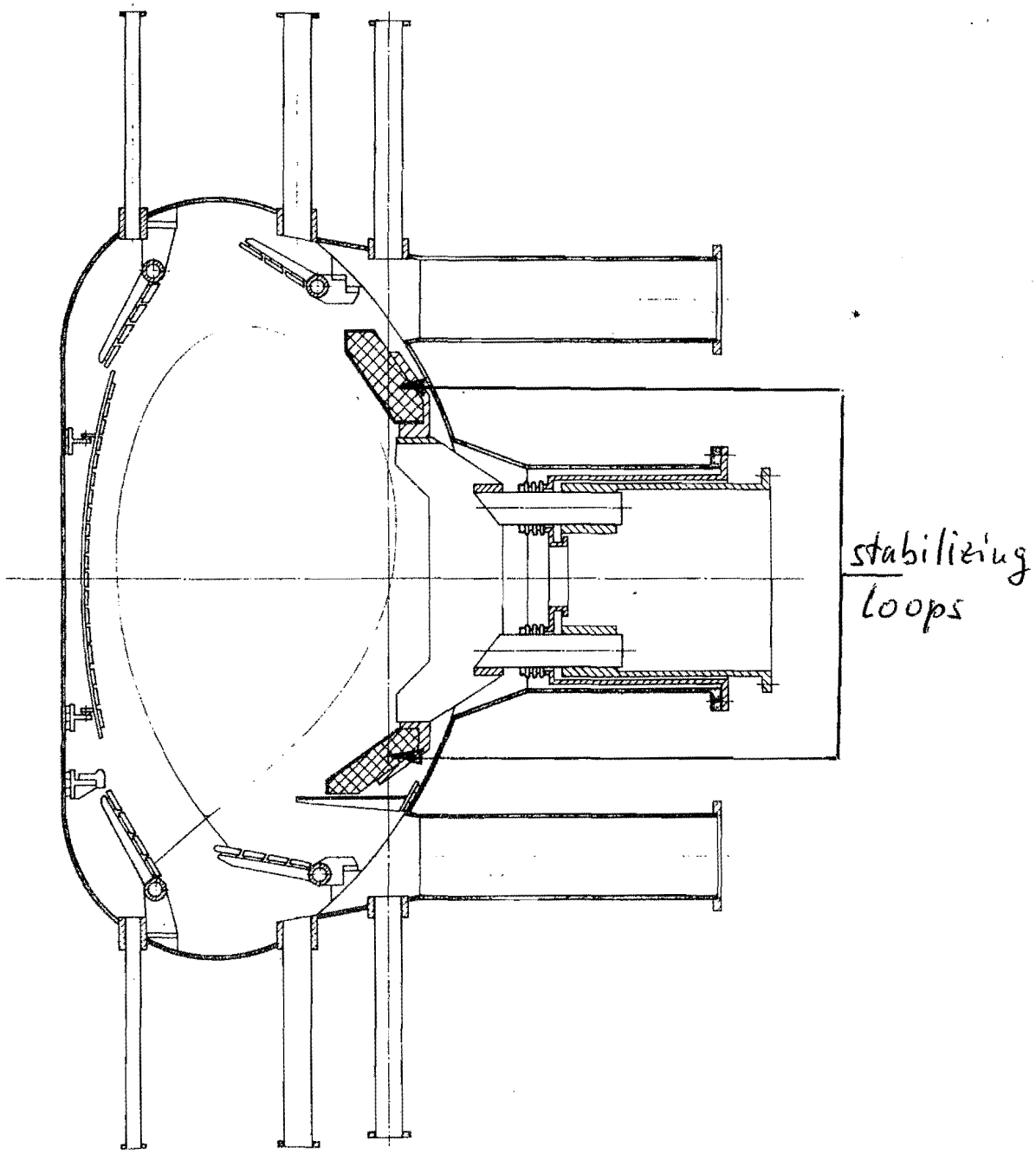

Fig 2.4 Vacuum vessel with passive stabilizing loops

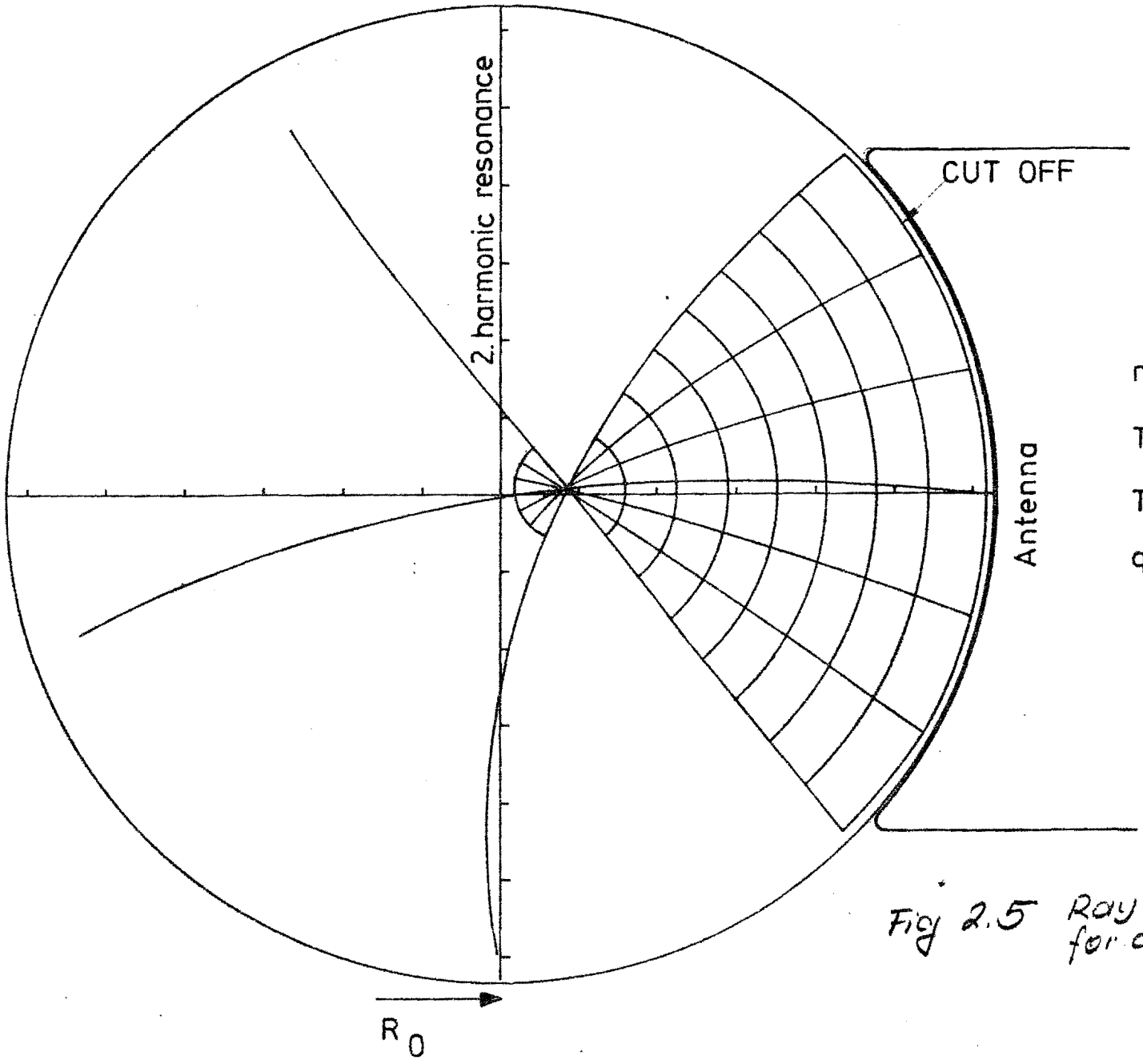

$n_0 = 10^{20}\ m^{-3}$

$T_{i0} = 0{,}8\ keV$

$T_{e0} = 0{,}8\ keV$

$q_a = 3$

Fig 2.5 Ray tracing calculations for a cold plasma

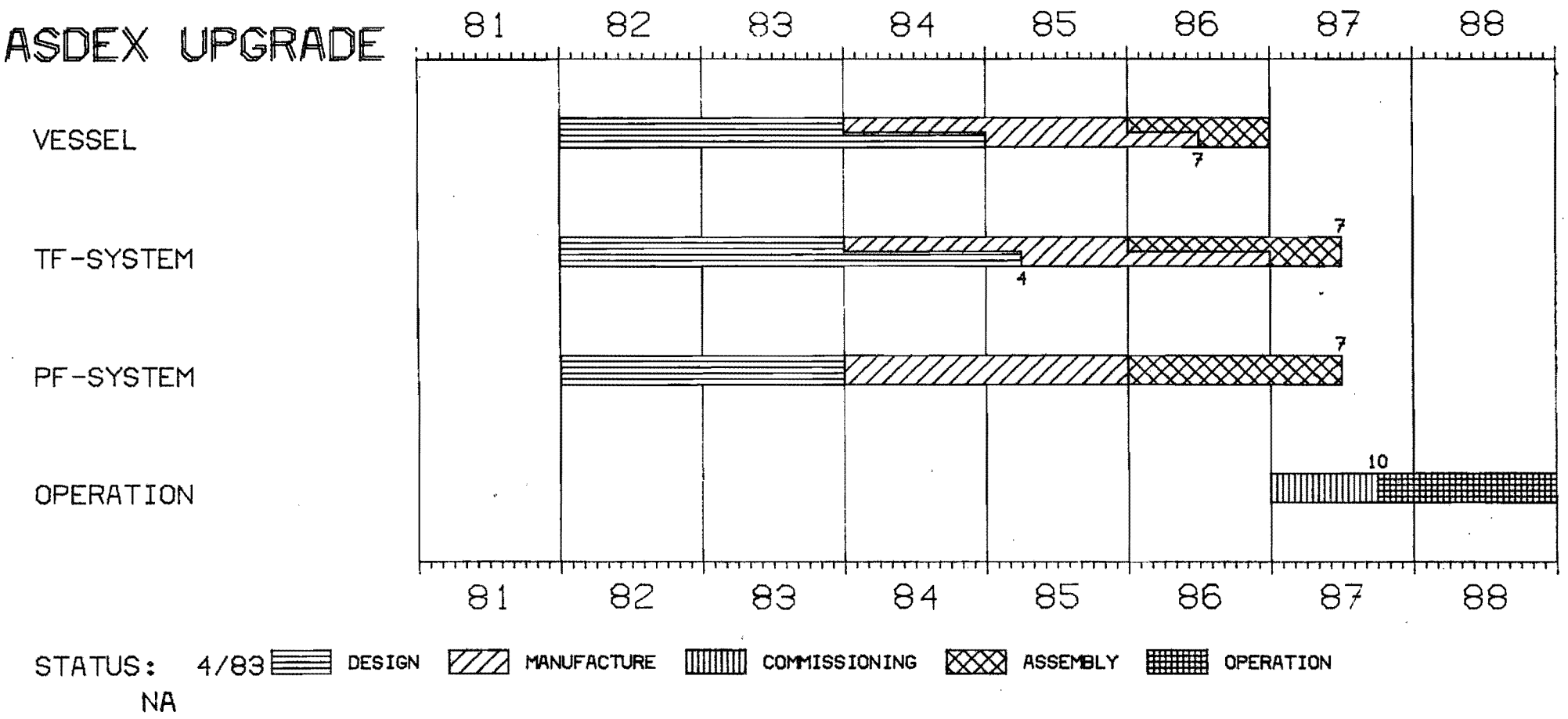

Fig. 2.6: Time schedule

STATUS: 4/83

ASDEX UPGRADE/CONSTRUCTION

PROFESSIONALS [MY/Y]

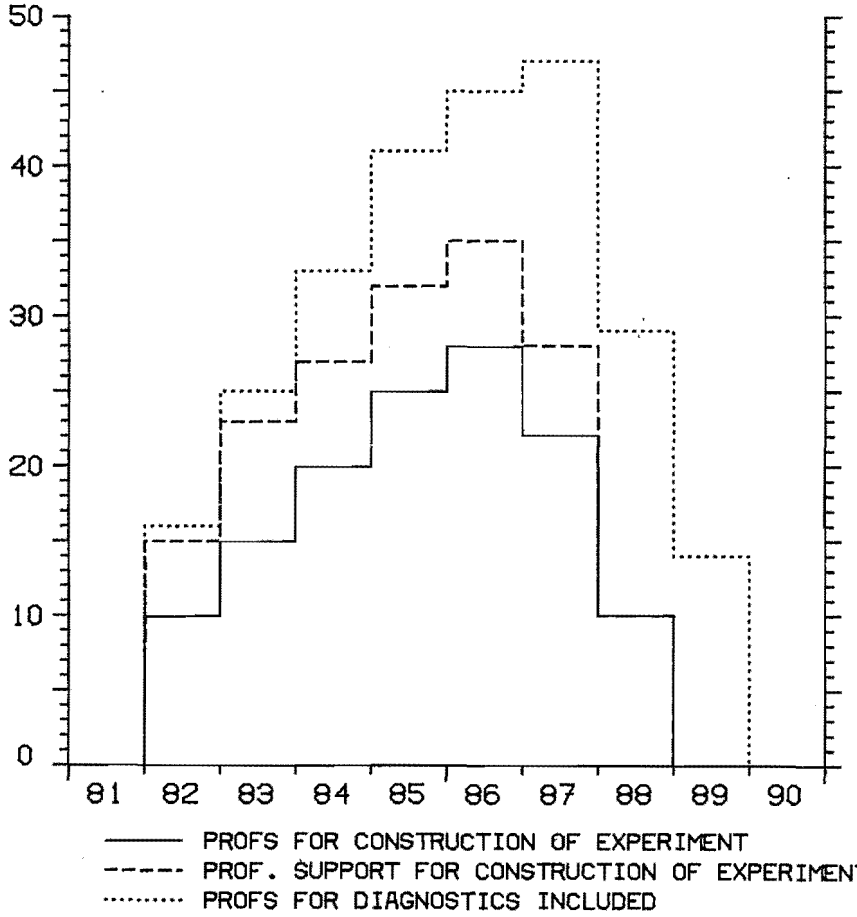

CAPITAL EXPENDITURE [MDM]

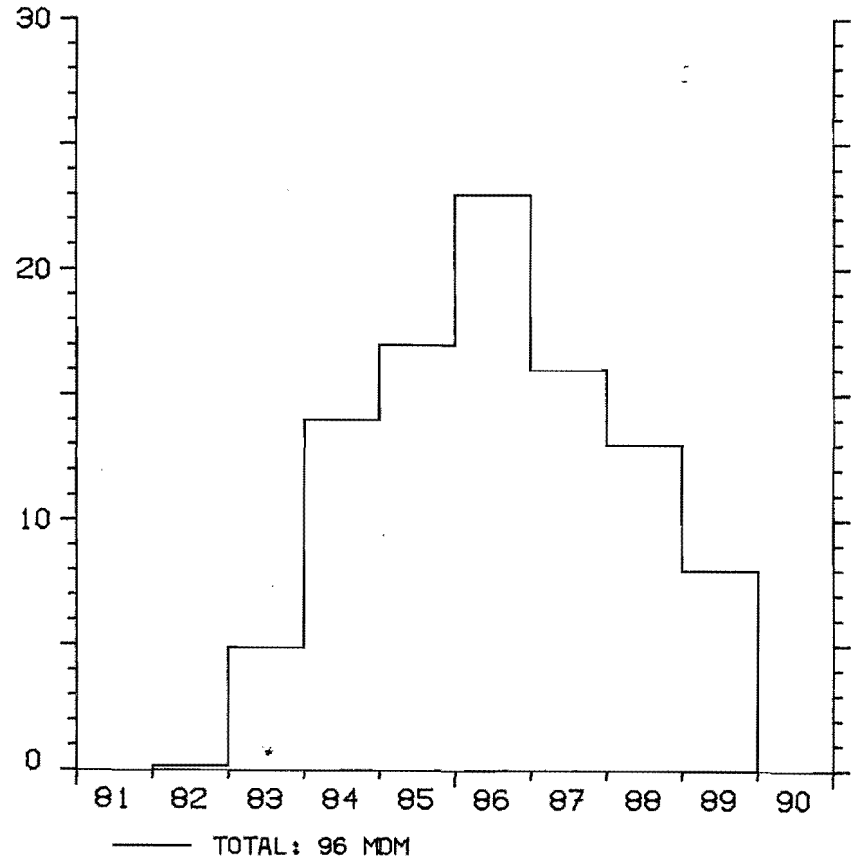

Fig. 2.7

3. The Tokamak System Components

3.1 The Toroidal Field (TF) Magnet

The toroidal magnet comprises 16 double pancake coils and the turn-over structure (TOS), which houses the outer parallel flanked part of the coils (Fig. 3.1.1). The TOS contains 8 large casings which are split in the torus plane by flanges. Each large casing includes two small casings which fix the enclosed coils and provide force locking in the toroidal direction. Typical parameters of the complete TF magnet are shown in Table 3.1.1.

3.1.1 Description of the Toroidal Field Coils

A maximum toroidal field of B_{ϕ} = 4 T can be produced at the geometric plasma axis R_{ϕ}= 1.65 m. The resulting coil forces and average mechanical stresses for this case are listed in Table 3.1.3.

To allow for plasma elongation and provide space for the divertor chamber, a vertically elongated TF coil aperture as provided by a constant-tension D-shape is required. This coil type supports the centering force (CF) exerted by the toroidal magnetic field entirely over the straight vertical part of the inner coil leg. To take up the CF of all 16 coils, a vault has to be formed within the gap between the central ohmic heating transformer and the plasma vessel. The width of this gap determines the size and hence the cost of the tokamak system in leading order. To make the best use of this gap, a separate CF support structure as well as coil casings have to be avoided there. Consequently, the 16 inner coil legs will be tapered over their full winding thickness and assembled to create a vault by force locking over the area CFSA shown in Fig. 3.1.4. In this way more than 70 % of the gap can be filled with copper.

As a consequence of the vault support via the inner coil legs, compressional stresses originate in the conductors and their insulation. These stresses are no problem for the insulation. However, oval cooling channels have to be chosen in order not to overstress the conductors within the vault area (Fig. 3.1.5). Circular cooling channels will be provided in the remainder of the coil.

For running an experiment it is most advantageous to keep

the TF magnet at ambient temperature like the peripheral experimental equipment. Water cooling is therefore envisaged for the TF coils. There are basically two cooling modes:

- Adiabatic pulses with recooling during puls intervals. The recooling time can be kept below 6 minutes.

- Long pulses with intense water cooling during the pulse. In this case a water throughput sufficient for absorbing the ohmic losses up to B_o = 3 T can be provided.

During adiabatic and long pulse operation the maximum insulation temperature at full magnetic loading will be kept below 70 C in anticipation of an initial copper and cooling water temperature of 20 C.

Most of the pulses will be adiabatic. To achieve a long pulse duration in this case, the conductor layout provides constant current density within any winding cross-section of a coil. The temperature development during a pulse with B_o = 4 T is shown in Fig. 3.1.7.

Long pulse cooling calls for a high water throughput during a pulse. To stay within the insulation temperature limit at reasonable cooling conditions, 3 cooling channels per conductor have to be provided. Additionally, lateral feeding of magnets calls for large water manifolds which consume valuable access area for the divertor pumping ports. Though the position of adjacent water manifolds will alternate with respect to the torus plane (Fig. 3.1.3), the available space is not sufficient for feeding every single turn of a coil with fresh water. A cooling length of two turns was therefore chosen. A cross-section of the resulting water manifold and the current terminals combined with it is shown in Fig. 3.1.6.

Under experimental conditions it is unrealistic to assume a total long pulse running time of more than 1000 hours. In contrast to generators, normally designed for running times of 30.000 hours, erosion by cooling water flow is a negligible effect. High water velocities are therefore permissible as proven by CERN magnets, which have already been operated for several thousand hours at 15 m/s. For the TF coils the water velocity within the cooling channels will be limited to 9 m/s. The development of cavitational effects is avoided by an outlet overpressure of 3 bar.

Figure 3.1.9 shows for B_o= 3 T and 9 m/s how the maximum temperature on the lateral conductor boundary (insulation temperature) develops with time. Steady-state conditions will be reached for a maximum insulation temperature of below 70 C. Since two turns are cooled in series, there

originates a maximum temperature difference of about 15 C between turns in succession. The thermal shearing stress resulting within the interturn insulation as well as the thermal compressional stress in the vault can be tolerated. An analytic estimate yields less than 20 MPa for both components.

Since the cooling system of the TF coils is designed for steady-state conditions, recooling of an adiabatic pulse within the recharging time of the flywheel generator is no problem at all. The development of the recooling temperature profiles after a pulse with B_o= 4 T is shown in Fig. 3.1.8. Recooling will be stopped after the outlet temperature has fallen below 25 C. The remaining temperature rise in the vault is then negligible. Further details of a TF coil and its cooling circuits are given in Table 3.1.2. The main dimensions of a coil are shown in Fig. 3.1.13.

3.1.2 Description of the Turnover Structure.

ASDEX UG is to be provided with a divertor of single null (SN) and double null (DN) configuration. The case of a pumping limiter (L) is also envisaged. The field components ($B_{p\perp}$) normal to a TF coil winding, produced by the poloidal field (PF) coils are for the divertor configurations (SN, DN) locally quite substantial. Figure 3.1.10 shows the distributions of $B_{p\perp}$ for a plasma current I_p = 1 MA along the center line of the upper half of a coil. The largest $B_{p\perp}$ values are encountered for the DN configuration. The maximum $B_{p\perp}$ values of the SN configuration reach only 60 % and those of the L case only 30 % of the DN case. The field component $B_{p\perp}$ interacting with the coil current (I_c) creates a line load ($I_c \times B_{p\perp}$) in the coils which is directed normal to the coil midplane (lateral direction). The forces integrated between zero points of the $B_{p\perp}$ distribution, and the moments (MX, MZ) integrated between the coil legs of the upper half of a coil are listed in Table 3.1.4 for B_o= 4 T and I_p = 1 MA. There is a moment Mx resulting from the line load $I_c \times B_{p\perp}$, which tries to turn over the coils in the lateral direction. The $I_c \times B_{p\perp}$ forces are therefore called turnover forces and the external structure which supports the coils is called the turnover structure (TOS). It is mainly the divertor configurations that call for as rigid as possible a TOS in the lateral direction in order to protect the TF coils from excessive bending and shearing stresses.

The ideal TOS would be a closed toroidal shell into which the TF coils are incorporated. Since the vault also provides turnover support by means of frictional forces, the ideal structure is rather well approximated by the combination of vault and external TOS shown in Fig. 3.1.4. Both structures together leave just a short region of the coil circumference unsupported.

As is well known from JET, the basic support reaction of the TOS is provided by a shear flow. The shearing shell of ASDEX UG surrounds the TF coils up to a distance of 1280 mm from the torus center. From this shell there extend strong box-like structures into the gaps between adjacent coils, which transfer the lateral forces from the coils to the shearing shell. To reduce bending deformations of the shell, where the force transfer boxes enter the shell, the shell is reinforced by stiffeners (Fig. 3.1.11). In order to maintain the shear flow of the shell on the casing flanges, laterally directed shear sleeves were chosen for the joints (Fig. 3.1.2). These sleeves also have the advantage of taking up out-of-plane forces of the shell resulting from force transfer moments.

The small casings provide the required space for the 8 large horizontal port openings in the torus plane. The full gap width of adjacent coils is available for these ports. The missing connection of the small casings via the torus plane calls for additional tension bolts on the casing connections. These bolts are arranged inside the shear sleeves. In the torus plane the flange connection of a large casing also has to transfer shearing forces caused by the moment Mz. As in JET, radial shear dowels (Fig. 3.1.2) were chosen there in order to provide space for the horizontal ICRH antenna ports.

All the access openings provided by the TOS are shown in Fig. 3.1.1. The ports are arranged symmetrically to the torus plane. However, the alternating water manifold recesses require for the 30 divertor pumping ports a small lateral shift (40 mm) out of the midplane between adjacent coils. The water manifolds are designed so that the TF coils and TOS can be assembled laterally as well as radially, parallel to the torus plane.

3.1.3 Assembly and Positioning of the TF Coils

The main aims in assembling are to achieve well defined force transfer to the vault and the TOS and to position the magnets precisely.

Manufacturing tolerances and thermal expansion of the coils require a gap of about 10 mm between the outermost turns of a coil and the TOS. Lateral force transfer across the areas, shown in Fig. 3.1.4, calls for tolerance-compensating elements such as epoxy-filled steel bladders (ESB). For the vault, ESB with a filling thickness of 3 mm are arranged between adjacent coils. The ESB can be fabricated for the complete support length of 2 m. For the turnover force supports the coils are flanked by ESB with a thickness of 5 mm.

The ESB shrink about 2 % in thickness during bakeout. The shrinkeage of the casing ESB causes a well-defined gap of 0.2 mm between the coils and the TOS. This gap permits free thermal expansion during adiabatic pulses. For long-pulse operation, the lateral expansion of the coils exceeds 0.2 mm. After a pulse the coils could thus become friction-locked inside the cold TOS. Since the CF support region of a coil recools much faster than the part between the inner leg and water exit (Fig. 3.1.8), small gaps would originate in the vault. To avoid undefined vault support conditions, the coil current must not be completely switched off after a long pulse. A power supply of about 10 % of the flat-top power should be maintained until sufficient recooling is achieved.

The vault ESB will be filled after all coils are assembled in their final position. The filling pressure of 4 bar creates an outward force of 0.14 MN per coil, which is taken up by the two back screws in Fig. 3.1.4. The radial shrinkeage of the vault during bakeout of the ESB (0.15 mm) is compensated by the prestressed rubber bearings in Fig. 3.1.4. These bearings, accessible for retightening, can exert on the vault nearly 1 % of the centering force. The resulting prestress safely fixes the coils in their initial position during pulse intervals.

At each large casing two coils can be adjusted and fixed in a preliminary way before the small casings are mounted and the casing bladders filled. The steel bracing tape in Fig. 3.1.4 together with the back screws are provided to adjust the rotation of the coil around the central axis normal to its midplane as well as its radial position. The bracing tapes are removed after the vault ESB are filled. The lateral screws indicated in Fig. 3.1.4 adjust the remaining degrees of freedom of the coil midplane. The vertical position will be corrected by the bottom screw.

3.1.4 TF Coil Design and Manufacture

Cooling conditions, coil tapering and large conductor cross-sections call for elaborate conductor and coil manufacturing procedures. These problems were therefore studied by Brown Boveri and Co., Mannheim, in collaboration with Kabelmetall, Osnabrueck.

Each of the 12 turns of a pancake comprises three typical parts, as can be seen from Fig. 3.1.12. Each turn of the vault region has the same copper cross-section, but it is different in thickness and width owing to the tapering of the inner coil leg (Fig. 3.1.5). The upper and lower intermediate turn sections vary in width and thickness along their length (<960 mm) to provide the transition to the parallel flanked sections. Consequently, 4 brazed joints are

required to create one full winding length (≤10.2 m). Care has been taken to avoid joints closer than 10 cm to the end of the support regions since the highest mechanical stresses occur there. The location of the joints is shown in Fig. 3.1.13.

The three cooling channels of a turn are everywhere evenly distributed over its width (Fig. 3.1.12). This requires laterally inclined channels drilled into the intermediate sections. The transition from the circular to the oval cooling channels is demonstrated in Fig. 3.1.12. The circular channels are widened in the lateral direction and the oval ones in the vertical direction. This results in congruent cross-sections in the brazed joints, section C-C in Fig. 3.1.12. To avoid too large cooling channel cross-sections on these joints, the diameters of the circular cooling channels are reduced to 11 mm on the vault-directed end of the intermediate piece.

The large turn thickness of the parallel-flanked section permits the use of screwed fittings to which copper pipes leading to the water manifold are brazed (Fig. 3.1.6). Currently, the tightness of the fittings is being tested with a 1:1 model of the conductor. First runs up to an average tension stress of 90 MPa with respect to the full cross-section 32 x 180 mm did not show any leakage under load conditions for the required number of cycles (20000).

Two cooling ducts with stepwise reduced diameters are drilled laterally into a conductor in order to feed the three parallel cooling channels. A total of 12 pairs of copper pipes convey the cooling water in two lateral planes to the water manifold.

The current connections of a coil (Fig. 3.1.6) consist of two strong copper plates with a cross-section of 240 x 42 mm . To take up the tension forces (0.2 MN) at the turn extremeties, the two copper plates are bolted across an inserted steel plate. The stiffness of this connection is comparable with that of the cross-over plate on the innermost winding. The lateral transition of the conductor tension from one pancake to the adjacent one develops a moment. To introduce this moment with little bending stresses into the coil former, the turn ends will be extended beyond the current connections. To avoid delamination of the bonded extensions, they continuously decrease in thickness towards zero, so that an increasing gap is formed with the turn underneath. This gap is closed with an epoxy wedge.

During winding of the coils considerable forces have to be exerted on a turn to keep it down on the mandrel (brazed joints) and to position it laterally (varying turn width).

To be able to exert these adjusting forces on the bare copper surface, only a tape as wide as the conductor will be wound in for inter-turn insulation. This tape will be composed of two epoxy prepreg and 7 glass fabric layers. The pancake insulation is to be composed of 14 layers. The coil insulation is taped semi-overlapped.

The strength of the BBC-Orlitherm insulation is only known at ambient temperature. A few static tests exist at 70 C, the maximum temperature at which the TF magnet should work at full load. An even higher temperature level could increase the adiabatic flat-top time. Dynamic shear tests, using a bar specimen, have therefore been started to measure the shear strength at 70 C, 80 C, and 90 C.

The manufacturing tolerances estimated by BBC on the basis of the JET coil fabrication are listed in Table 3.1.5. The manufacturing time for 1 fabrication test coil and 16 series coils is expected to be 127 weeks or roughly 2 1/2 years.

3.1.5 Manufacturing of the TOS

The TOS of ASDEX UG is rather similar to the JET structure, for which ample manufacturing experience is available.

The TOS design has been discussed with experts from industry. As a result, the structure can be manufactured by casting as well as by welding. A manufacturing time of 1 1/2 to 2 years including final machining and preassembly, has to be taken into account. The manufacturing precision required for the shear connections seems to be no problem. Preassembly was recommended.

3.1.6 Stress Analysis

Stress acceptance criteria will be based on the ASME Boiler and Pressure Vessel Code. This code distinguishes primary and secondary stresses.

The following stress analysis concerns the primary stresses. Thermal (secondary) stresses have already been briefly treated in sec. 3.1.1.

The load cases were subject to the following assumptions:

- for the toroidal field loading, that all 16 TF coils are correctly positioned and have equal current;

- for the turnover loadings, that unperturbed consistent plasma and PF currents are taken into account.

The results and their interpretation presented below mainly concentrate on the coils. There are two critical regions of a coil:

- the cross-section where it leaves the vault support. The maximum conductor and insulation stresses of this region, region 1, determine the upper limit of the product plasma current (I_p) times toroidal field (B_o);

- the water manifold region, region 2. There the tension and bending stresses have to stay below the level above which the screwed water manifold fittings could start to leak.

For the TOS the maximum equivalent stress and joint forces are determined.

3.1.7 Stressing by Turnover Forces

The stress analysis was performed with the finite element (FE) models of Fig. 3.1.14, model 1, and Fig. 3.1.15, model 2. The FE model 1 comprises the main force transfer properties between the coils and TOS as well as via the flange connection joints of the large and small casings and the support reactions of the vault. Truss elements connect coil and TOS at cross-sections which are stiffened by bulkheads (Fig. 3.1.14b). With a few iterations all trusses which transferred tension forces were eliminated. In order to assess the transition from the vault to the unsupported part of a coil more accurately, the three-dimensional (3 D) model 2, representing only a TF coil, was meshed. The reactions of the TOS were in this case represented by prescribed displacements, known from model 1. Model 2 will also be used for the toroidal field forces.

With respect to the stiffness properties of the TOS, model 1 represents the large port openings in the torus plane quite accurately. For the remaining ports a rough approximation is possible by means of void elements. For the sake of higher-order symmetry in the lateral direction, the alternating position of the water manifold with respect to the torus plane was neglected.

Both models assume symmetry to the torus plane. The SN loading was therefore split into two parts:

- A loading with even symmetry (SNA) originating from the horizontal flux contribution of the PF. This flux component results from the current difference of PF coils located opposite each other with respect to the torus plane.

- A loading with odd symmetry (SNB), which is equivalent

in symmetry to the DN and L cases. It originates from the PF flux penetrating the torus plane vertically.

In contrast to the real arrangement, it was assumed that the SN stagnation point is located above the torus plane. In this case the superpositioning of SNA and SNB loadings produces the larger forces above, the lower forces below the torus plane.

In Table 3.1.6 the critical stresses and maximum displacements of all three loading cases are quoted for the same product of $I_p \times B_o = 4$ MAT. Despite the 40 % smaller forces the SN case shows a larger maximum shearing stress in region 1 than the DN case. The comparatively higher maximum shear stresses of the SN case have to be attributed to the SNA loading. The lines of constant SNA in-plane shear stress are plotted in Fig. 3.1.16 for region 1.

The maximum equivalent stresses originating in the TOS for SN, DN and L conditions are quoted in Table 3.1.7. The available FE model is not suited for assessing stress concentrations in the corners of port openings or other places of structural discontinuities. However, for ductile materials these stress concentrations can be considered as secondary stresses. As known from the JET structure, even nodular castings can reach rupture strains of more than 20 % and a fracture toughness close to that of stainless steel.

3.1.8 Stressing of the Coils by TF Forces

The TF magnet is constant-tension optimized with respect to the magnetic pressure of the toroidal field. An appropriate model was developed for calculating the TF coil stresses (Fig. 3.1.15). The main concern up top now has been with the stressing of the conductors within the vault support.

The distribution of the lateral vault compression stress (VCS) was investigated with a two-dimensional FE model. The insulation and the polygonality of the coil cross-section were taken into account. The results, representative of the cross-section in the torus plane, yield a rather homogenous distribution of the VCS along the coil midplane. The deviation from the average VCS is less than 10 %.

The cooling channels imply a structural discontinuity for the flow of the VCS within a conductor. Significant strain concentrations (secondary strain, ASME) thus result in their vicinity. As long as the zero to maximum strains are limited to below 0.5 %, copper can carry a load as large as the yield strength (200 MPa) for the envisaged number of cycles (20000). The pattern of equivalent strain was computed with a nonlinear FE code and referred to the average compressive

stress (ACS) on the smallest copper cross-section of the cooling channel walls. Figure 3.1.17 shows the results for an ACS of 175 MPa and 200 MPa. At the larger value, where the ACS is equivalent to the yield strength, the strain limit is surpassed within the small region indicated. However, the load carrying capability of the cooling channel walls is not yet exhausted. This was shown by cyclic tests (up to 10^5 cycles), which were performed by IABG Ottobrunn. At ACS = 200 MPa, the cooling channel walls withstood 10^5 cycles without any sign of fatigue. Still at ACS = 220 MPa, three times the required number of load cycles were sustained.

As a consequence of these test results, the average compressive stress (ACS) was thus inserted for computing the safety margin of the cooling channel walls given in Tables 3.1.1 and 3.1.8.

3.1.9 Safety Margins

The safety margins of the conductors are referred to the minimum guaranteed yield strength of Cu Ag, i.e. 200 MPa. According to the ASME code a safety margin of 1.5 is desirable. For the insulation the calculated shear stress should not exceed 20 MPa. Fatigue tests (10^5 cycles) by BBC have yielded a permissible stress of 60 MPa at ambient temperature. With due allowance for manufacturing uncertainties, a safety margin of three is required.

Table 3.1.8 contains the equivalent stresses and the resulting safety margins of a TF coil for SN, DN and L. The limits of $I_p \times B_o$ indicated are given either by the energy supply (L, DN) or by the stresses (SN). For the $I_p \times B_o$ values listed the safety margins prescribed by the ASME code are achieved.

3.1.10 Summary

The basic problems of the TF magnet concept have been dealt with. On the basis of the present assessment, realization of the design is feasible with respect to manufacture, assembly and mechanical reliability.

Table 3.1.1: Main parameters of the Complete TF Magnet

Toroidal system	
number of coils	16
total weight of coils	150 t
magnetic field strength (B_o) at plasma centre	
steady-state conditions	3 T
adiabatic pulses	4 T
rise time to B_o = 4 T	8 s
adiabatic flat-top time (AFT) at B_o = 4 T	10.5 s
total number of ampère-turns at B_o = 4 T	33 MA
field ripple amplitude at plasma boundary	< 2 %
stored magnetic energy at B_o = 4 T	440 MJ
ohmic losses at B_o = 4 T	
start of AFT	103 MW
end of AFT (10.5s)	112 MW
maximum energy dissipated up to end of AFT (10.5 s)	1.4 GJ
max. cooling water flow rate, steady-state	504 l/s
max. permissible recooling time (AFT)	10 min
amount of water for recooling of max. pulse (AFT)	30 m^3
Turnover structure (TOS)	
small casings, total number	16
weight/casing	3.1 t
large casings, total number	16
weight/casing	4.8 t
Total weight of the TF magnet (coils and TOS)	280 t

Table 3.1.2a: Main Parameters of a Single TF Coil

Number of pancakes		2
number of turns per coil		24
turn current at B_o = 4 T		85.9 KA
veritical opening of coil bore		2.96 m
horizontal opening of coil bore		1.90 m
overall thickness of winding, including coil insulation		
outer leg, up to tapering edge		413 mm
inner leg, straight part		354 mm
overall width of winding, outer leg		373 mm
large radius of coil tapering edge		950 mm
conductor material		Cu Ag 0.1
0.2 % yield strength	200 to	220 MPa
conductivity at 20 C		57 $m/\Omega\,mm^2$
net turn copper cross-sections		
outer leg		5330 mm
inner leg		3274 mm
peak voltage (B_o = 4 T)		
between turns		6.5 V
between pancakes		155 V
to ground		2.5 kV
thickness of epoxy-glass insulation		
between turns		1.6 mm
between pancakes		4 mm
outer ground insulation		4.6 mm

Table 3.1.2b: Cooling Parameters of a Single Coil

Cooling medium (deionized)	water
number of parallel cooling channels	
per turn	3
per coil (2 turns in series)	36
shape of cooling channels	
inner leg, straight part	oval
elsewhere	circular
dimensions of oval cooling channels	
outermost turn (12),	
max. width and height (mm)	14 x 8
turns 1 to 11	17.5 x 6
diameter of circular cooling channels	
outer leg and following part of intermediate piece	13.5 mm
remainder of intermediate piece	11 mm
maximum water velocity in a turn	
steady-state (3 T)	9 m/s
recooling of max. adiabatic pulse	1.5 m/s
maximum steady-state pressure drop (2 turns)	13 bar
maximum temperature of copper (insulation)	
adiabatic pulse (initial temperature 20 C)	70 C
steady-state (water inlet temperature 20 C)	65 C

Table 3.1.3: Coil Forces at B_o = 4 T and Resulting Primary Stresses Caused by the Toroidal Field on its own.

Centering force per coil	15.7 MN
circumferential vault force	40.1 MN
vault copper compression stresses, coil midplane	
average	61 MPa
maximum, turn 10	66 MPa
cooling channel wall, turn 10	82 MPa
vertical tension force per coil leg	4.6 MN
turn tension stresses	
inner leg	58 MPa
outer leg	36 MPa
equivalent turn stresses, inner leg, turn to 10	
coil midplane	107 MPa*
cooling channel wall	122 MPa
allowable stress for Cu Ag	
small displacement, $N > 10^5$, Rp02	200 MPa
safety margin, channel wall	1.6

Table 3.1.4: Integral Turnover Forces and Moments at $I_p B_o$ = 4 MAT for the Upper Half of a TF coil

	Double Null	Single Null		Limiter
	DN	SN A	SN B	L
Lateral forces between points of zero B_{pl} *)				
P_1	1.15	0.33	0.36	0.33
P_2 [MN]	-1.62	-0.31	-1.06	-0.81
P_3	0.49	0.11	--	--
Center coordinates (X,Z) of lateral forces *)				
X_1/Z_1	1.03/1.50	0.98/1.39	1.02/1.52	1.04/1.53
X_2/Z_2 [m]	2.06/1.50	2.09/1.48	2.29/1.26	2.37/1.18
X_3/Z_3	2.78/0.66	2.85/0.43	--	--
Moments *)				
$\lvert M_z \rvert$	0.79	0.	2.11	1.62
[MNm]				
$\lvert M_x \rvert$	0.35	0.06	0.81	0.47

*) The zero points, meaning of indices and coordinates follow from Fig. 3.1.10.

Table 3.1.5 : Manufacturing Tolerances of a TF-Coil according to BBC

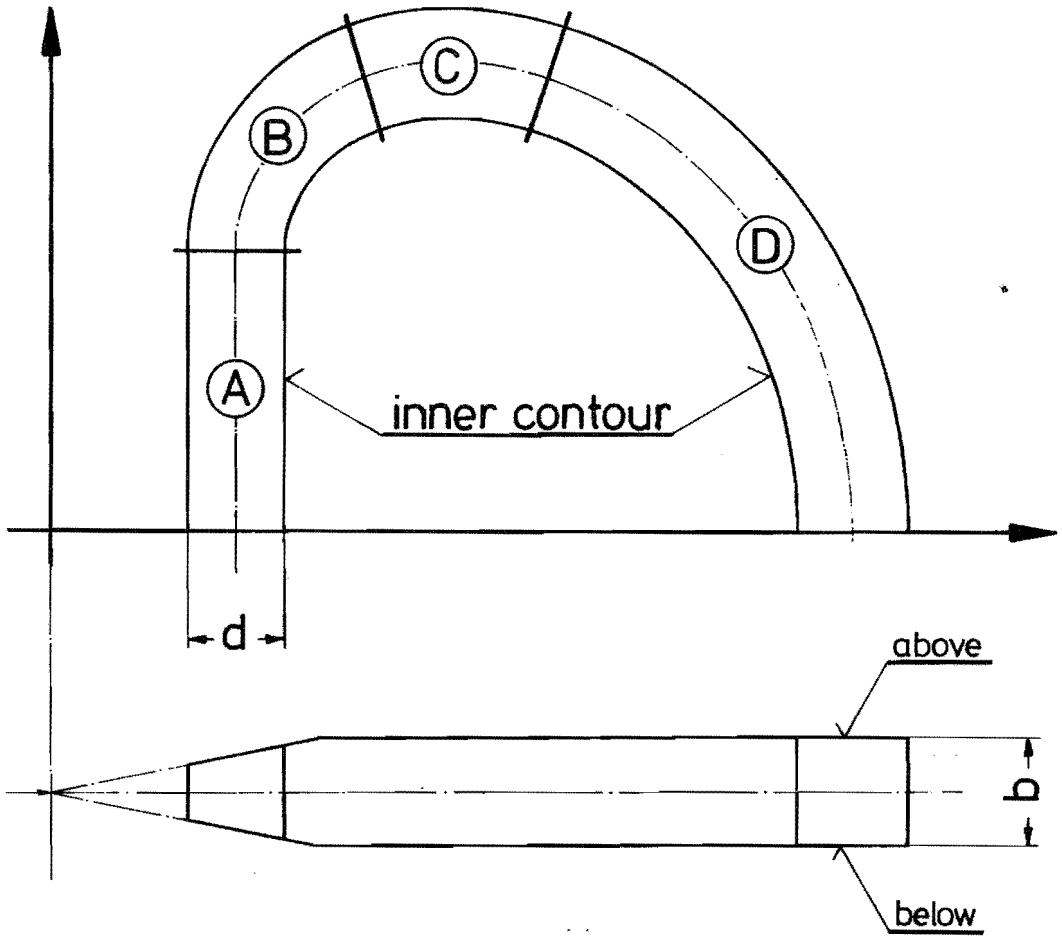

Dimension (mm)

coil region		A	B	C	D
inner contour		±2,5	±4		
thickness d		0/-2,5	+10/0		+/-3
width b		+/-1	—	+/-1	
evenness	above	1	—	2	
	below	1	—	1	

Table 3.1.6: Maximum Stresses and Displacements of a TF Coil at $I_p B_o$ = 4 MAT for DN, SN and L Turnover Load

	DN	SN	L
Bending stresses [MPa]			
Exit of vault			
outer cooling channel	20	15	5
conductor boundary	24	18	6
water manifold (fittings)	14	9	7
shearing stresses vault [MPa] (bending & torsion)	12	17	5
lateral displacement [mm]	1.	0.6	0.9

Table 3.1.7: Maximum Equivalent Stress and Joint Forces for the TOS at $I_p B_o$ = 4 MAT

	DN	SN	L
Maximum equivalent stress			
cross-section number *)			
structural component**)			
joint forces [MN] ***)			
tension		0.1	
at cross-section *)		3	
shearing		0.16	
at cross-section *)		3	

*) Refers to Fig. 3.1.14b.

**) Structural components of TOS (refers to Fig. 3.1.11)
UHP: upper horizontal plate (shearing shell)
LHP: lower horizontal plate (force transfer box)
LAP: lateral plates (force transfer box)
BUH: bulk heads (force transfer box, shearing shell)

***) The joints are dimensioned for a maximum tension and shearing force of 0.4 MN.

Table 3.1.8: Maximum Equiv. Coil Stresses and Safety Margins at the Operational Points (I_p B_o)

	double null		single null		limiter	
	stress MPa	margin	stress MPa	margin	stress MPa	margin
CONDUCTOR *)						
vault (cooling channel)	100	2	81	2.5	88	2.27
water manifold ***)	38	2.4	28	3.2	32	2.8
INSULATION **)						
shearing	12.3	4.9	19.	3.2	8.6	7
compression	43.6	4.8	32.3	6.5	43.6	4.8
tension	10.7	16.8	8.5	21.2	8.2	22
Tsai Hill margin		3.1		2.7		3.6
I_p B_o MAT	1.2 x 3.25		4.5		6.5	

*) Small displacement limit $R_{p0.2}$ = 200 MPa

**) N > 2 x 10^4 cycles limit, ambient
tension 180 MPa
compression 210 MPa

***) Preliminary limit 90 MPa

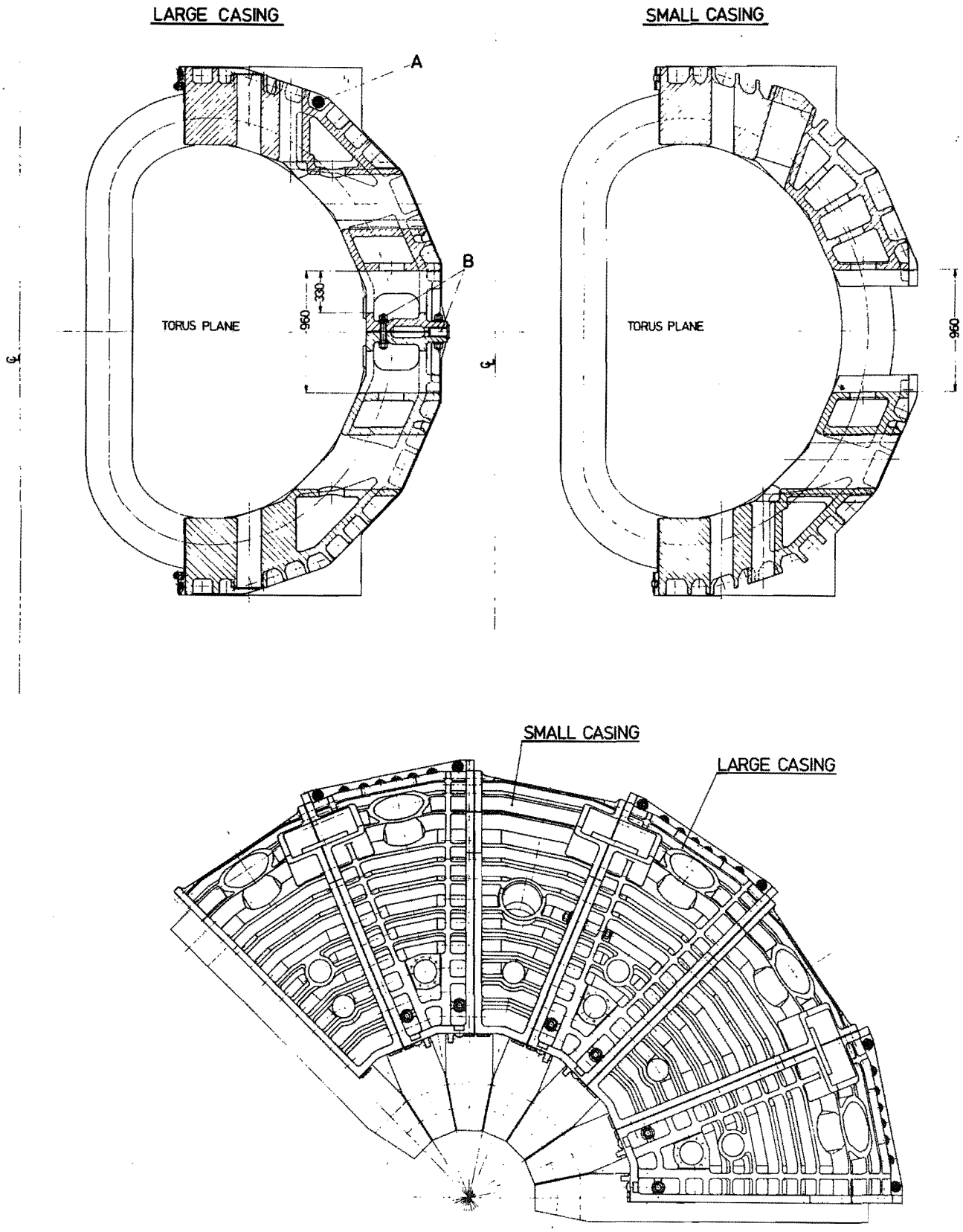

Fig. 3.1.1: Plan view and vertical cross-sections of the toroidal field magnet.

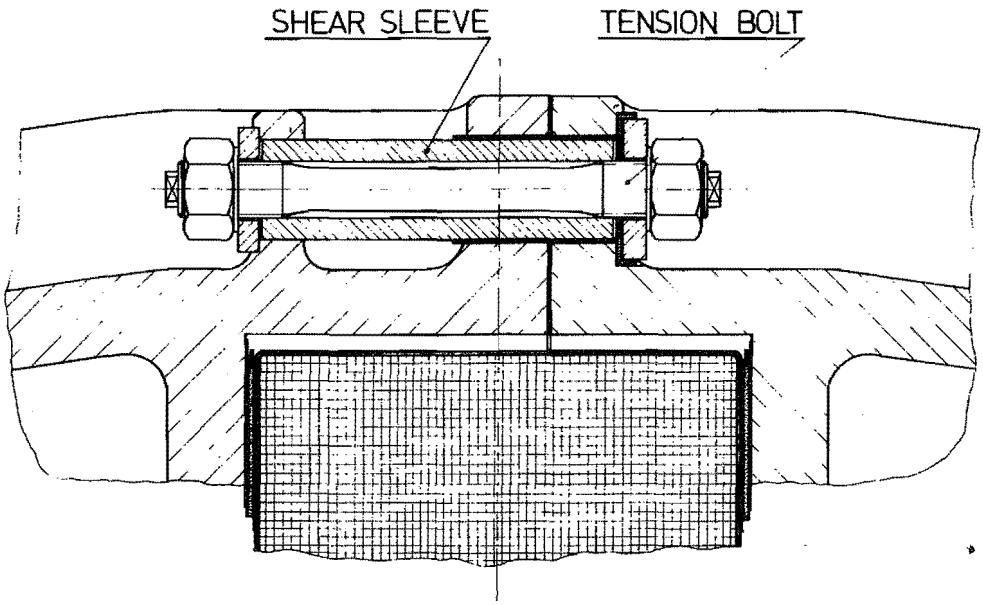

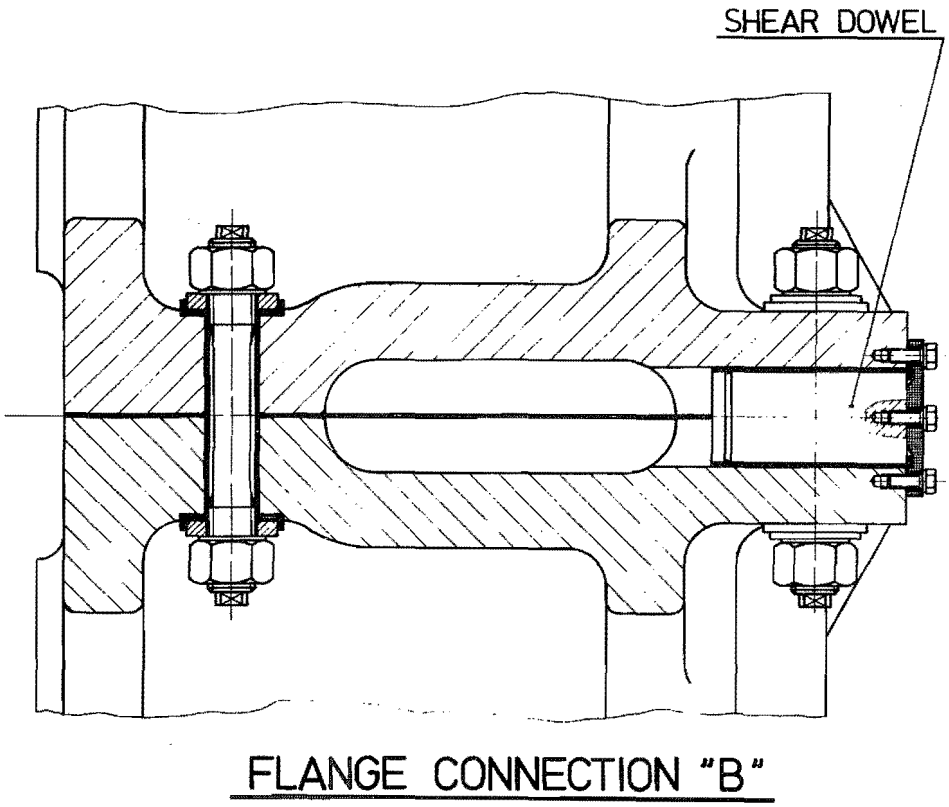

Fig. 3. 1. 2: Flange connections of adjacent casings (A) and in the torus plane (B).

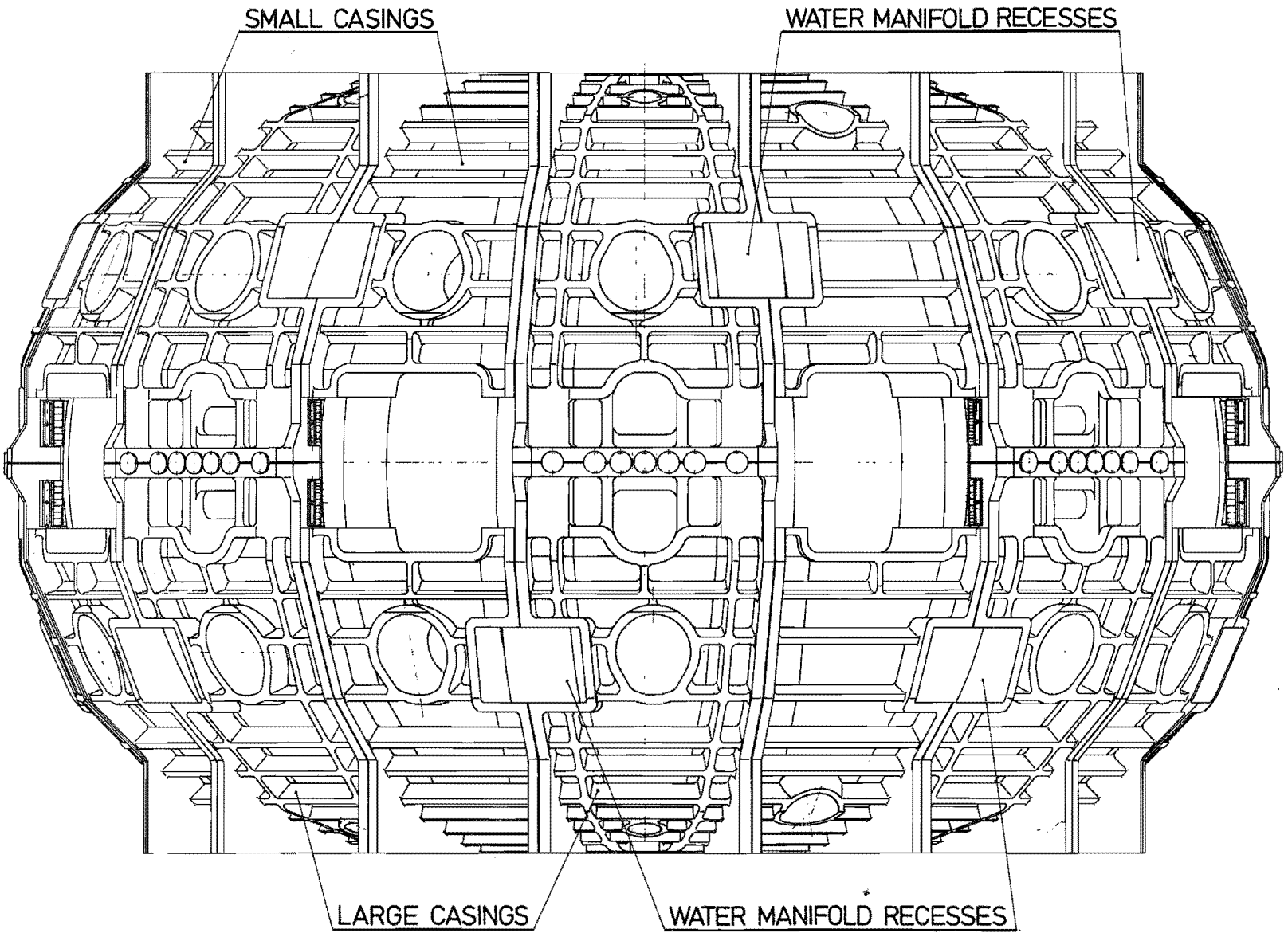

Fig. 3. 1. 3: Access openings and water manifold recess of the turnover structure.

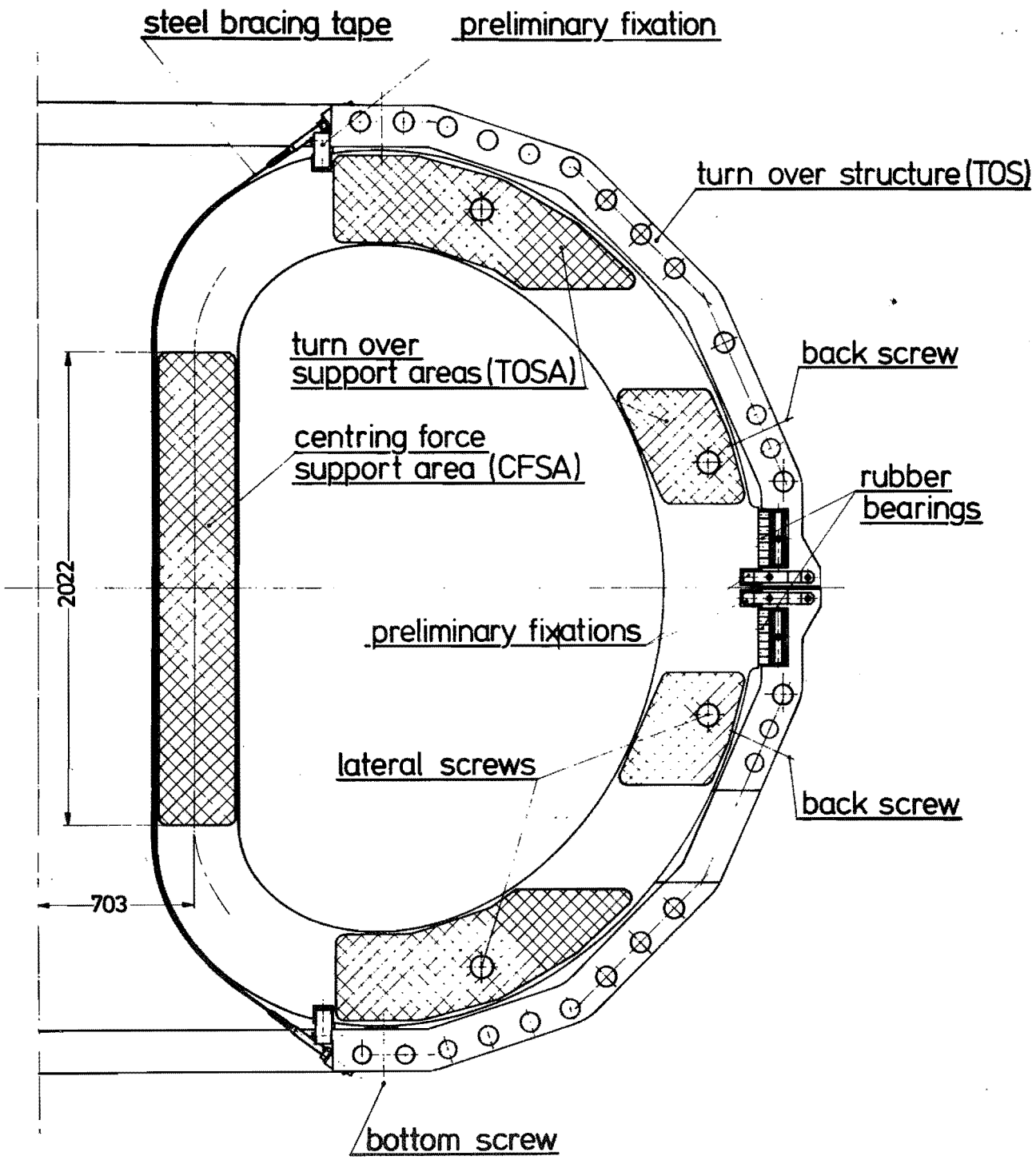

Fig. 3.1.4: Coil support areas and auxiliary assembly fixtures.

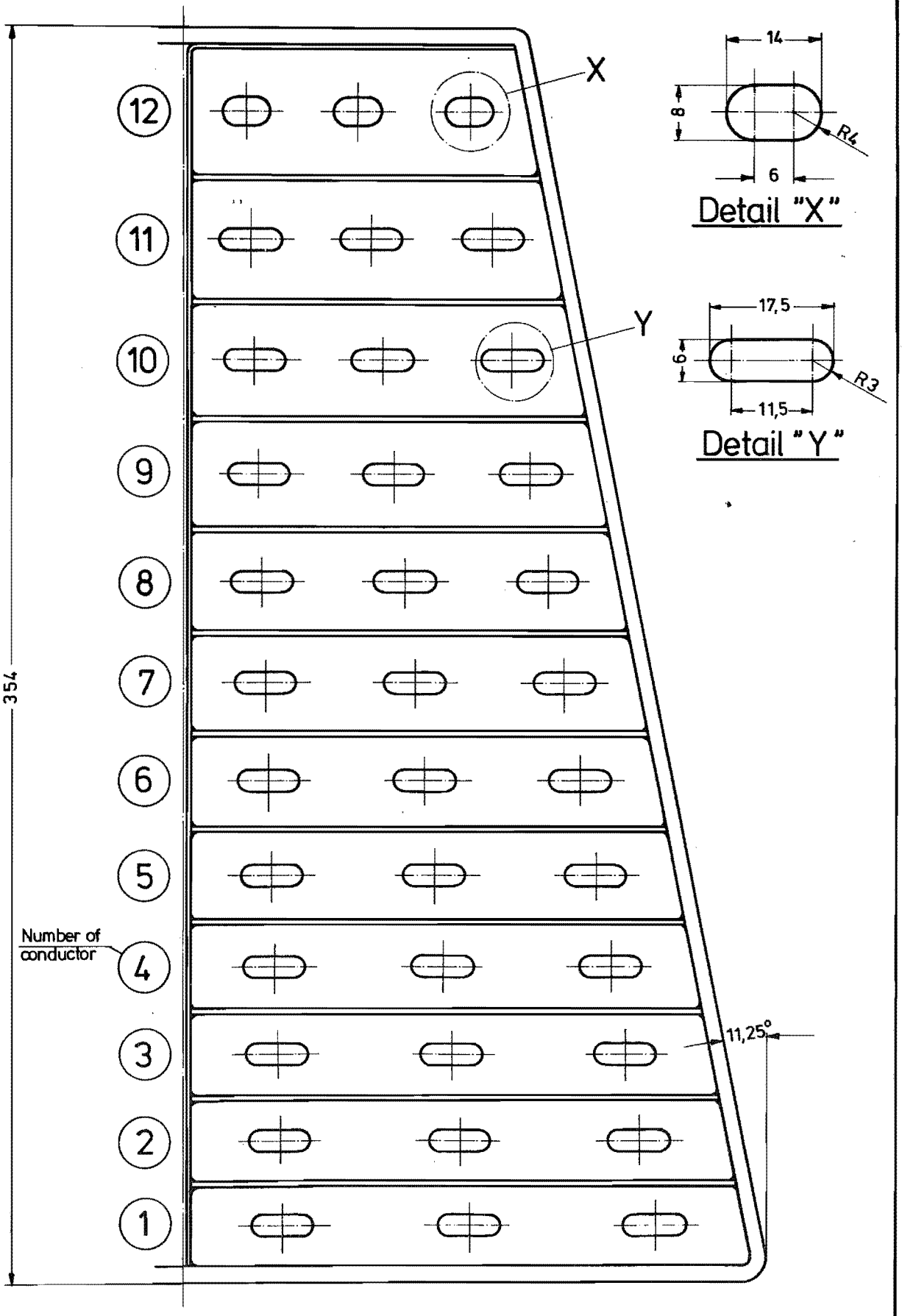

Fig. 3.1.5: Coil cross-section of the inner coil leg.

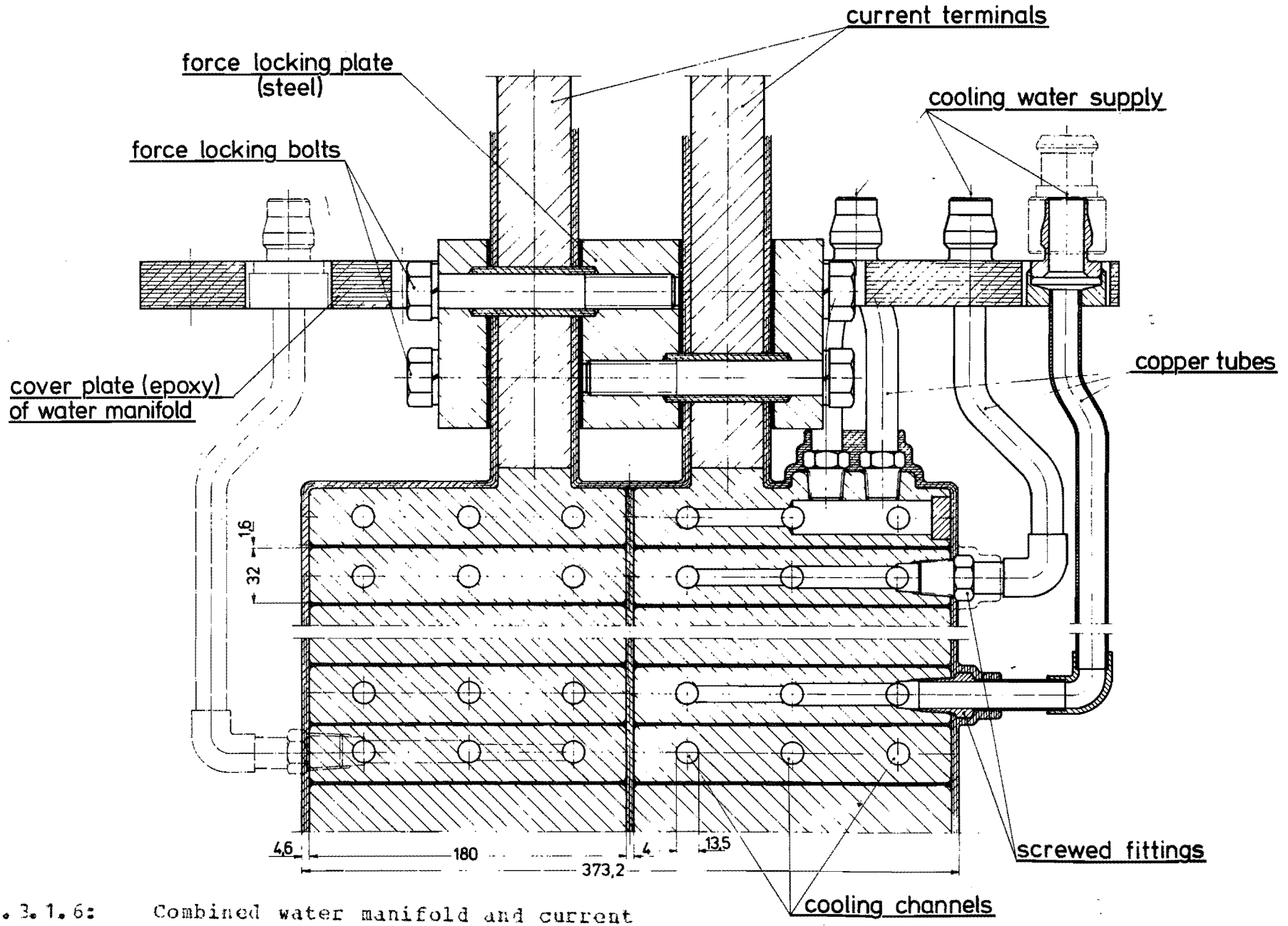

Fig. 3.1.6: Combined water manifold and current terminal.

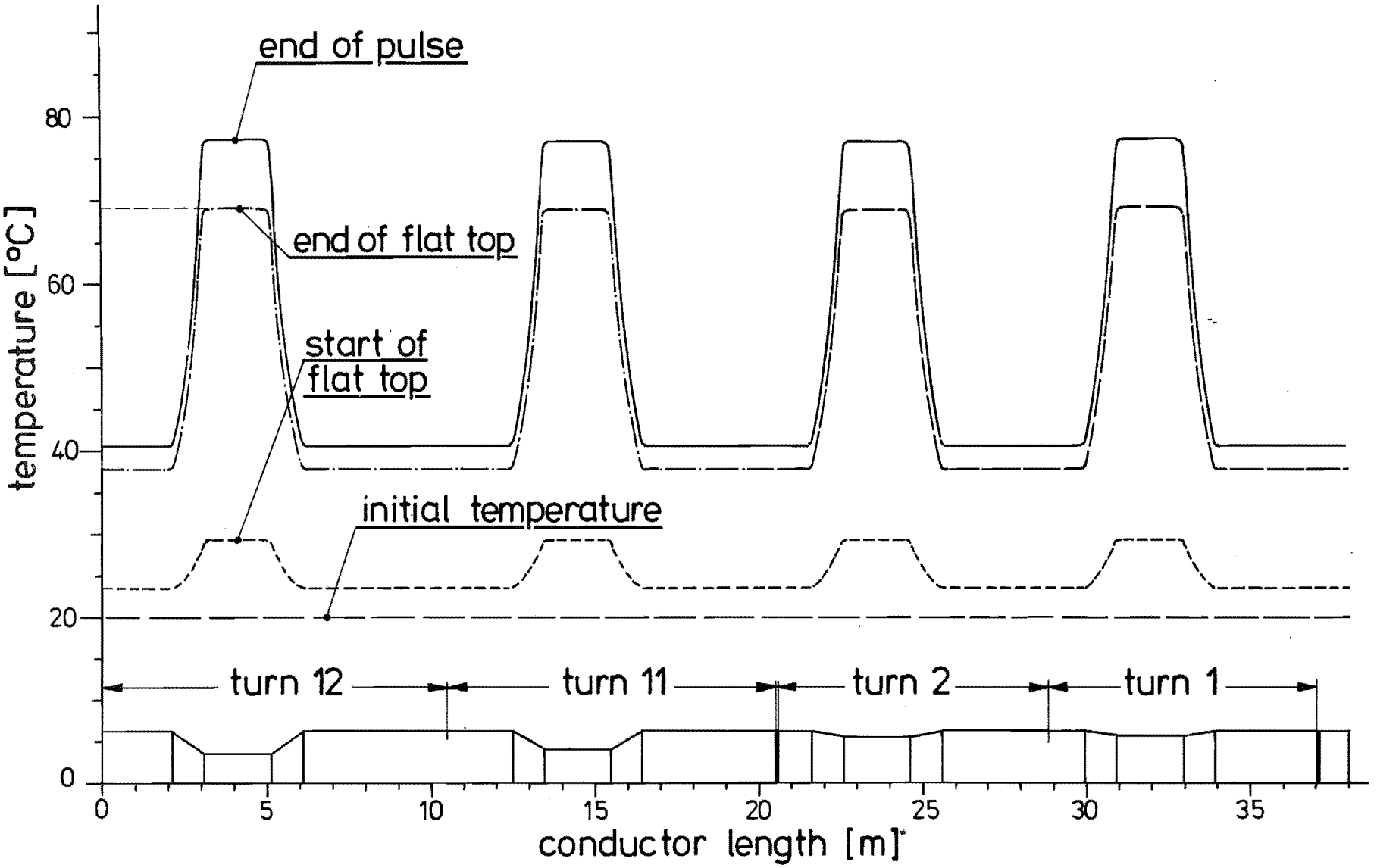

Fig. 3.1.7: Temperature profiles during an adiabatic pulse at B_o = 4 T; shape of ramp pulse: rise time 8 s, flat-top time 10.5 s, decay time 6 s.

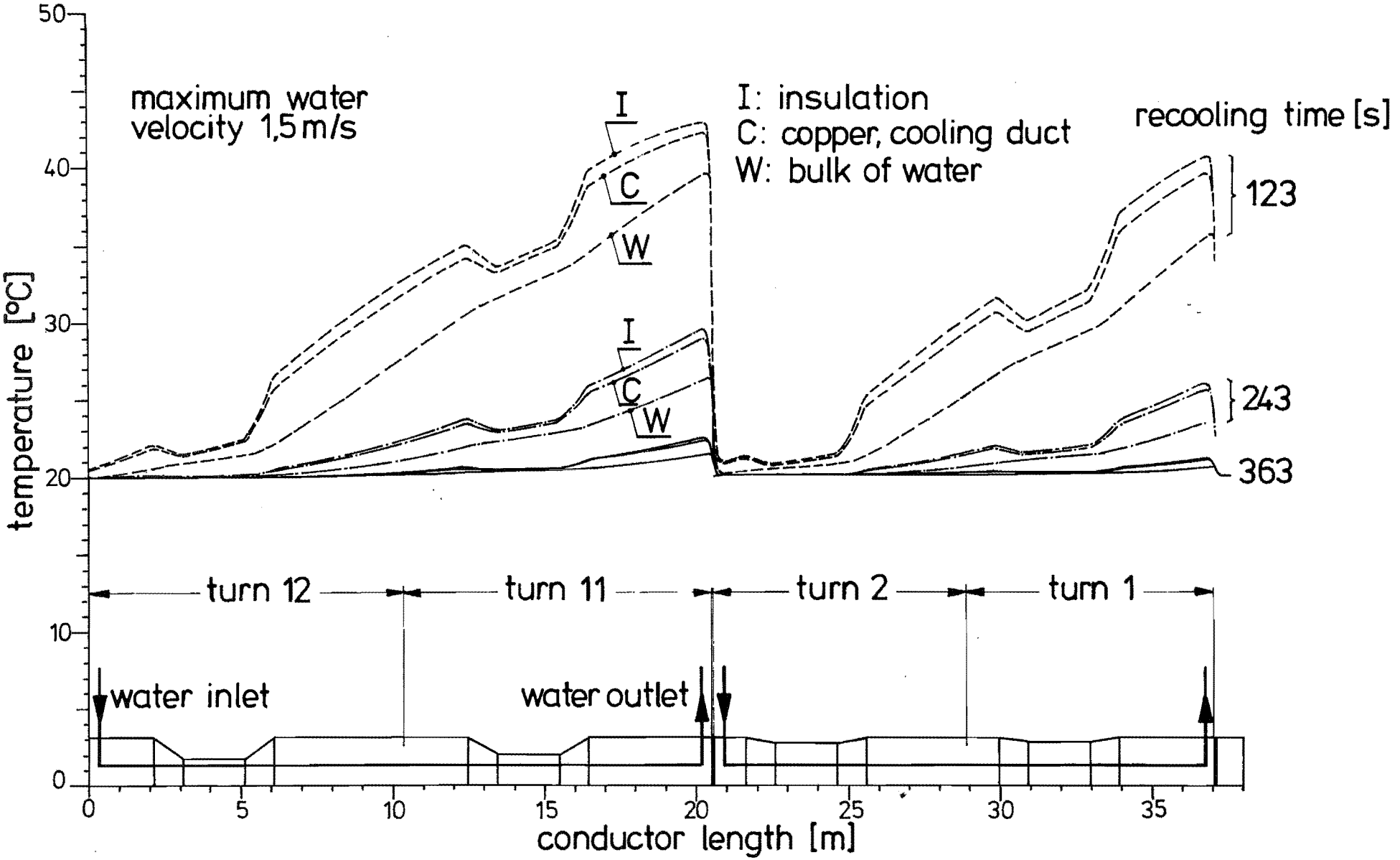

Fig. 3.1.8: Recooling temperature profiles after an adiabatic pulse at B_o = 4 T; shape of preceding pulse as for Fig. 3.1.7.

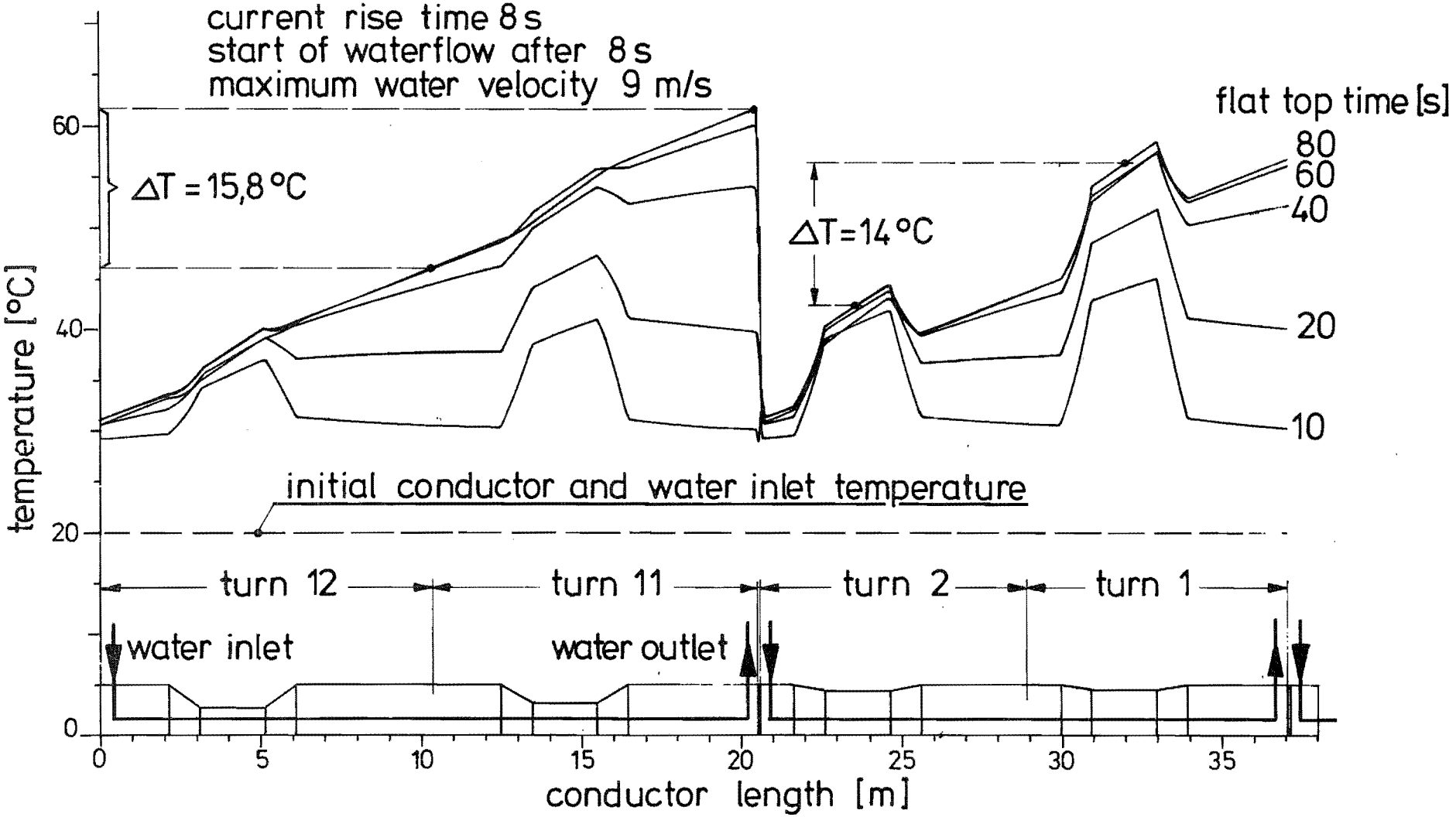

Fig. 3.1.9: Insulation temperature profiles for long pulse operation at B_o = 3 T.

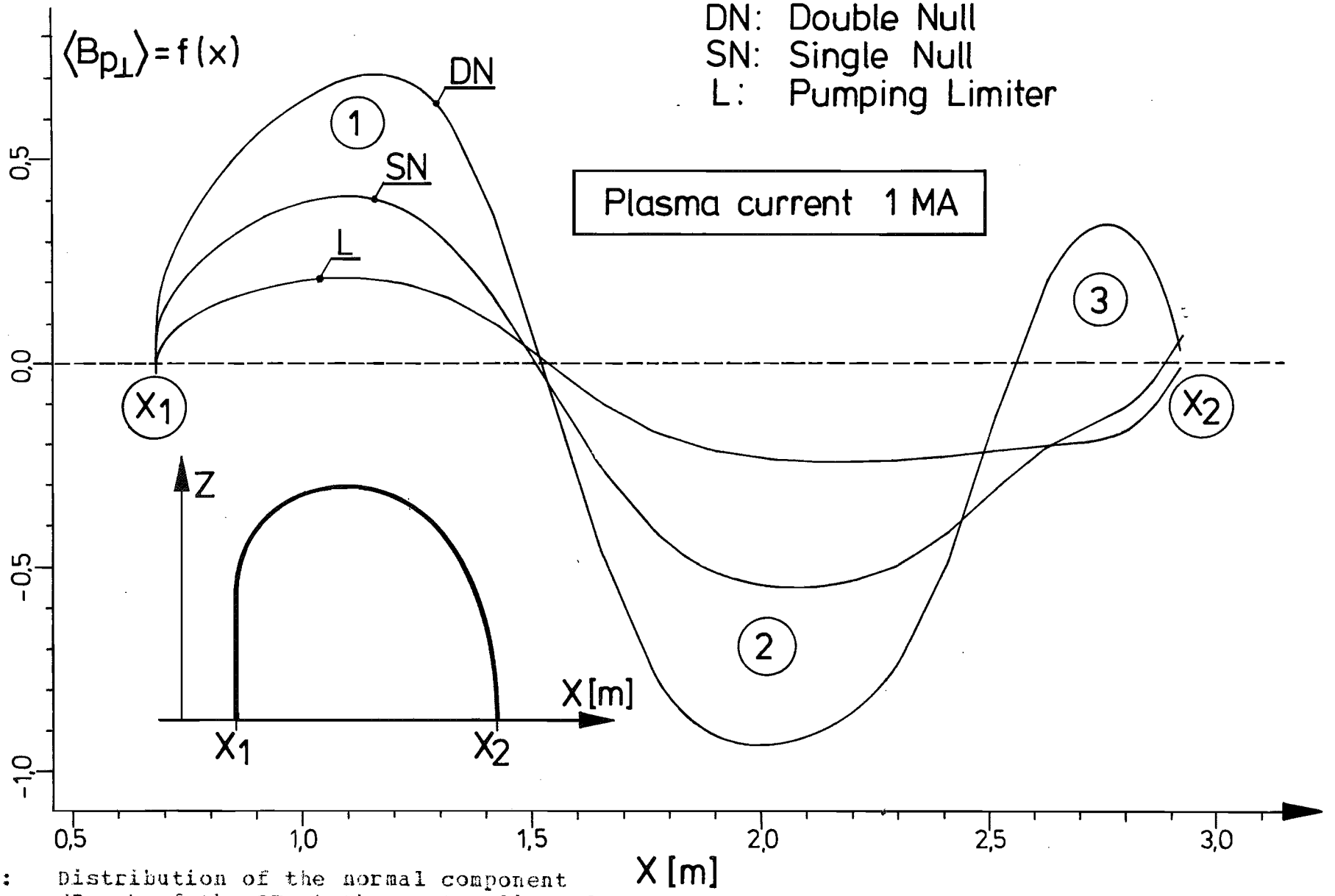

Fig. 3. 1. 10: Distribution of the normal component ($B_{p\perp}$) of the PF at the center line of the upper half of a TF coil for DN, SN and LI; for SN the stagnation point was assumed to be above the torus plane.

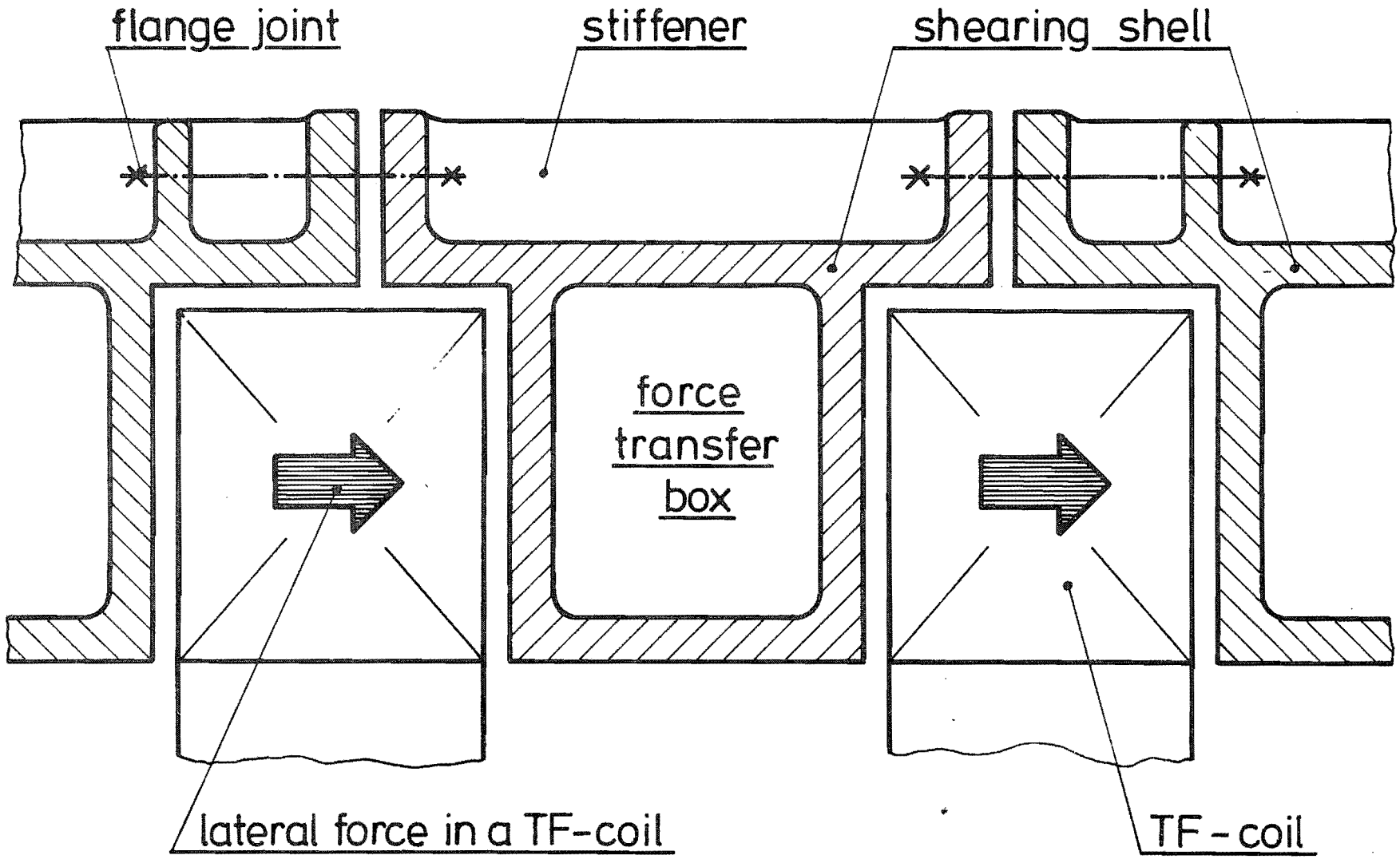

Fig. 3.1.11: Principle of lateral force transfer from the TF coils to the shearing shell of the turnover structure.

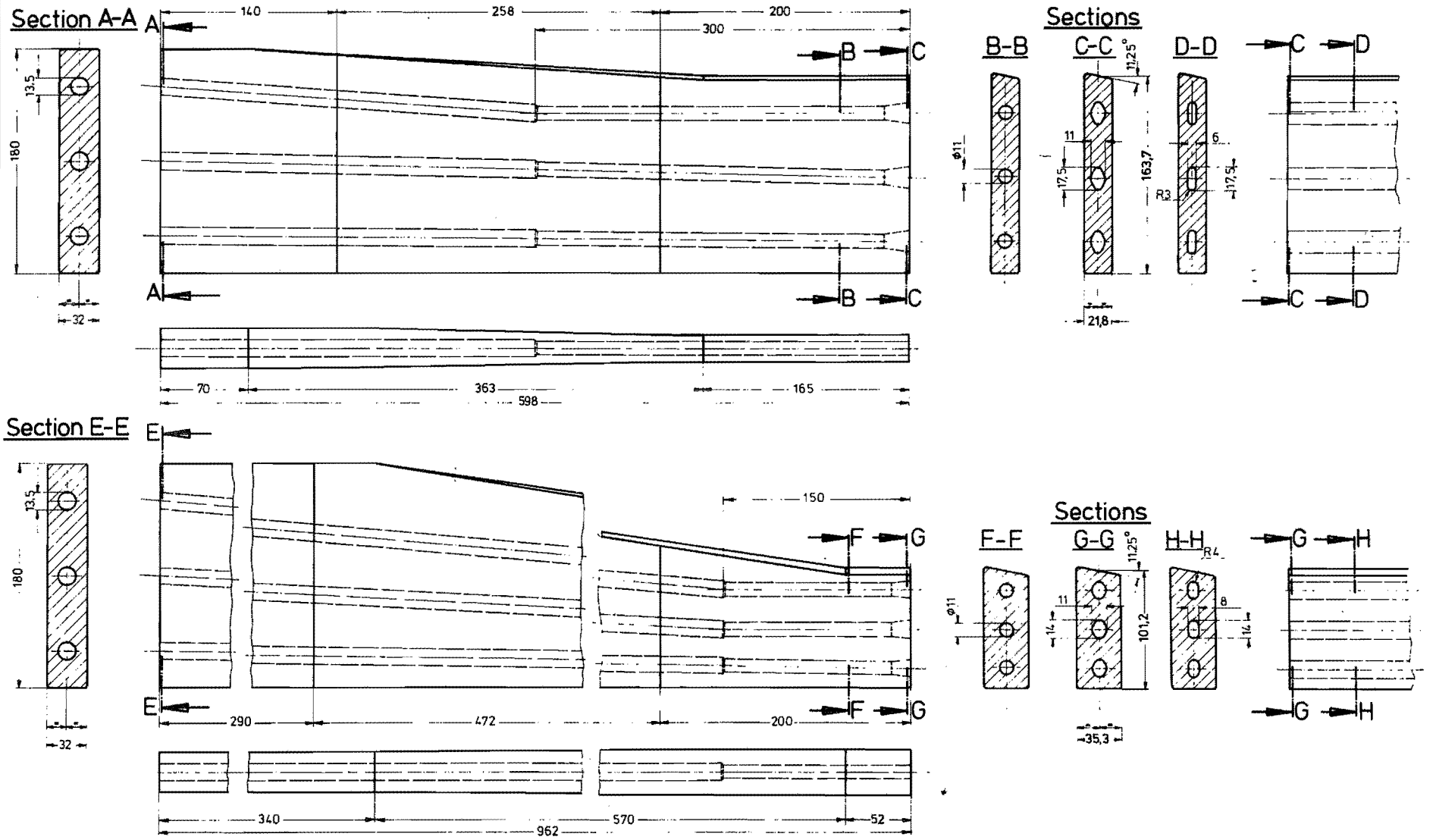

Fig. 3.1.12: Transition of conductor profiles and cooling channel cross-sections for the inner and the outermost turns.

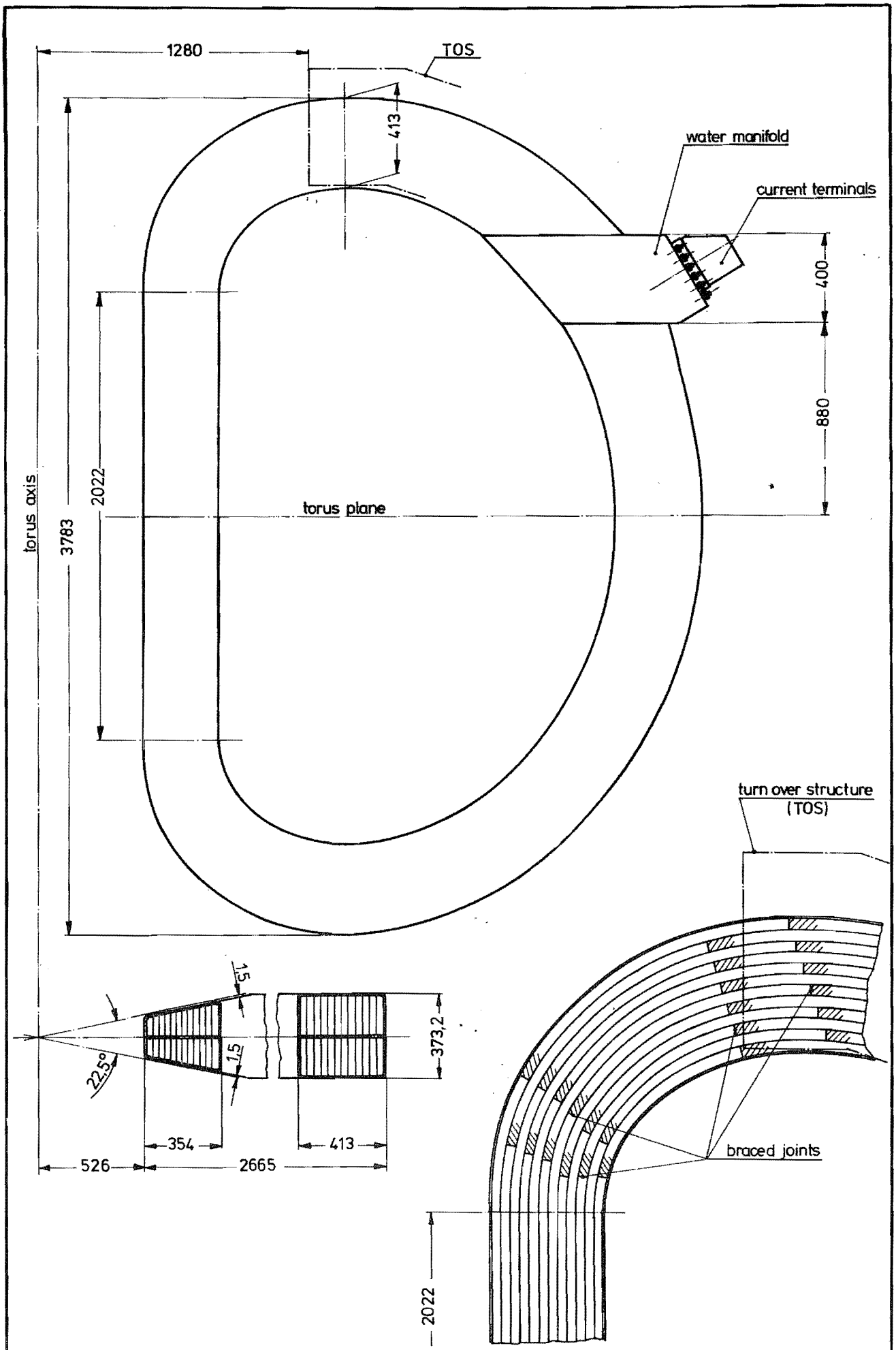

Fig. 3.1.13: Toroidal field coil dimensions and arrangement of braced joints.

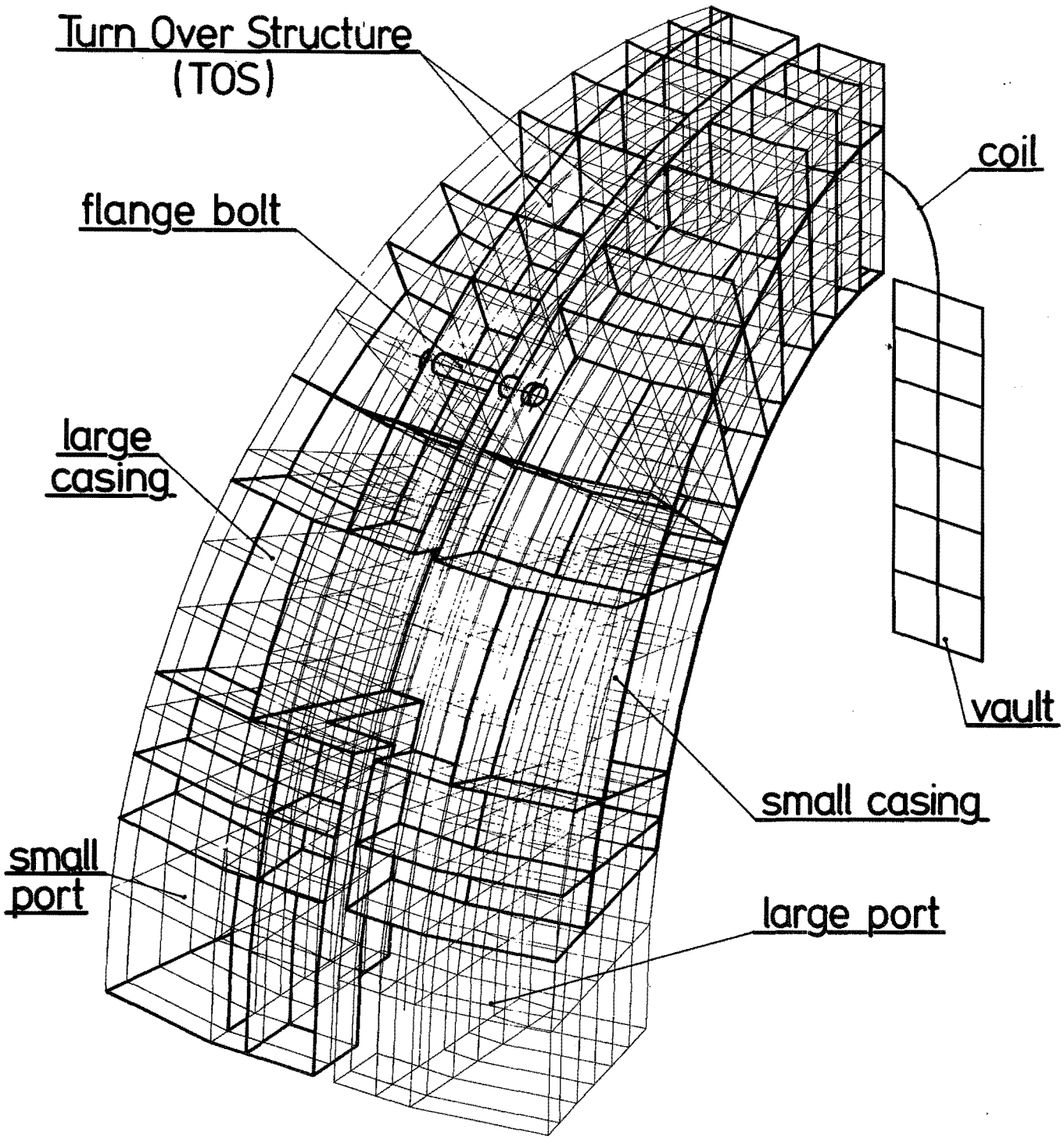

Fig. 3.1.14a: Finite-element model for the turnover loading; the coil is represented by a polygon of bars, the TOS and vault by plates.

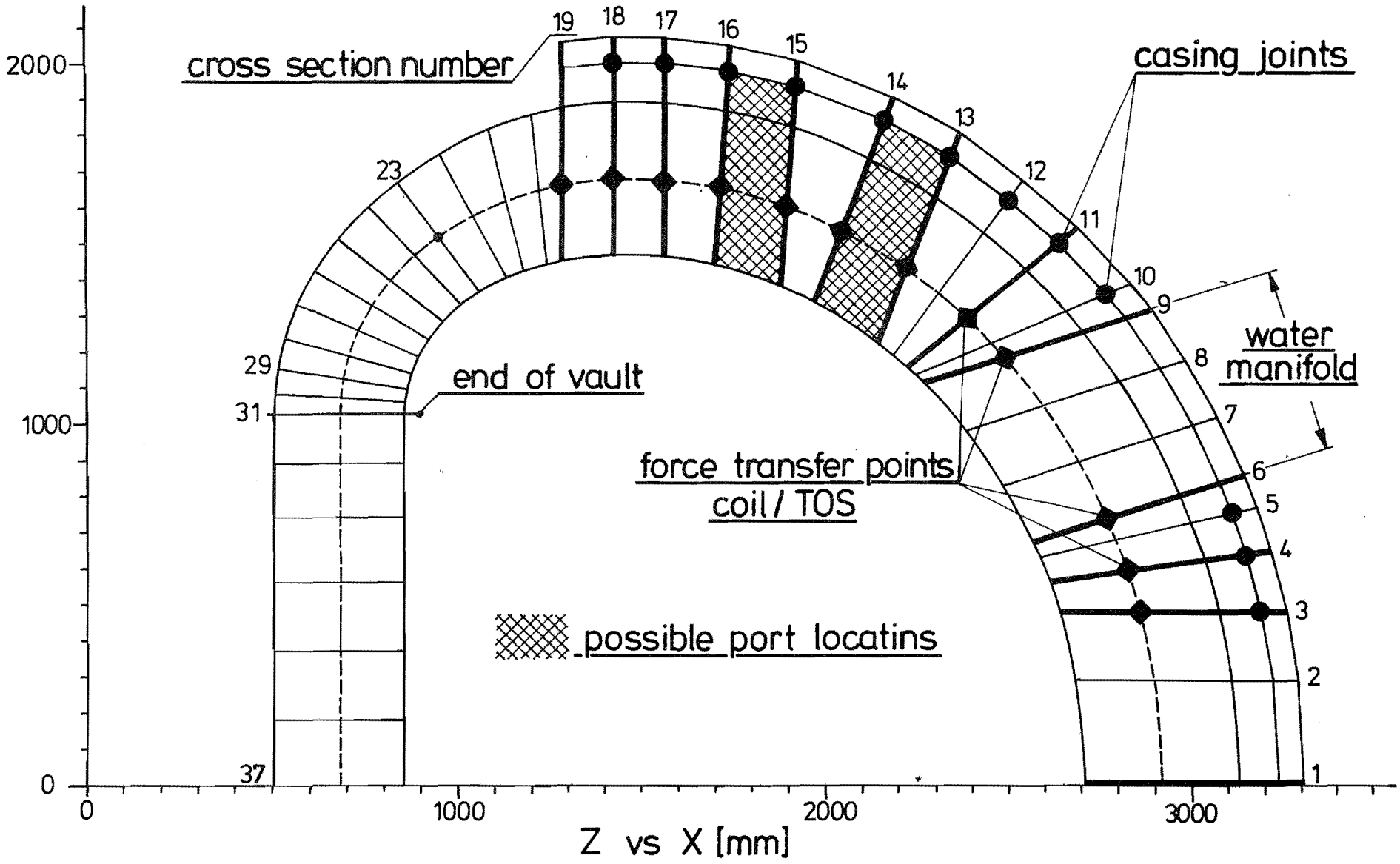

Fig. 3. 1. 14b: Circumferential subdivision of the FE model of Fig. 3. 1. 14a.

(preliminary graph)

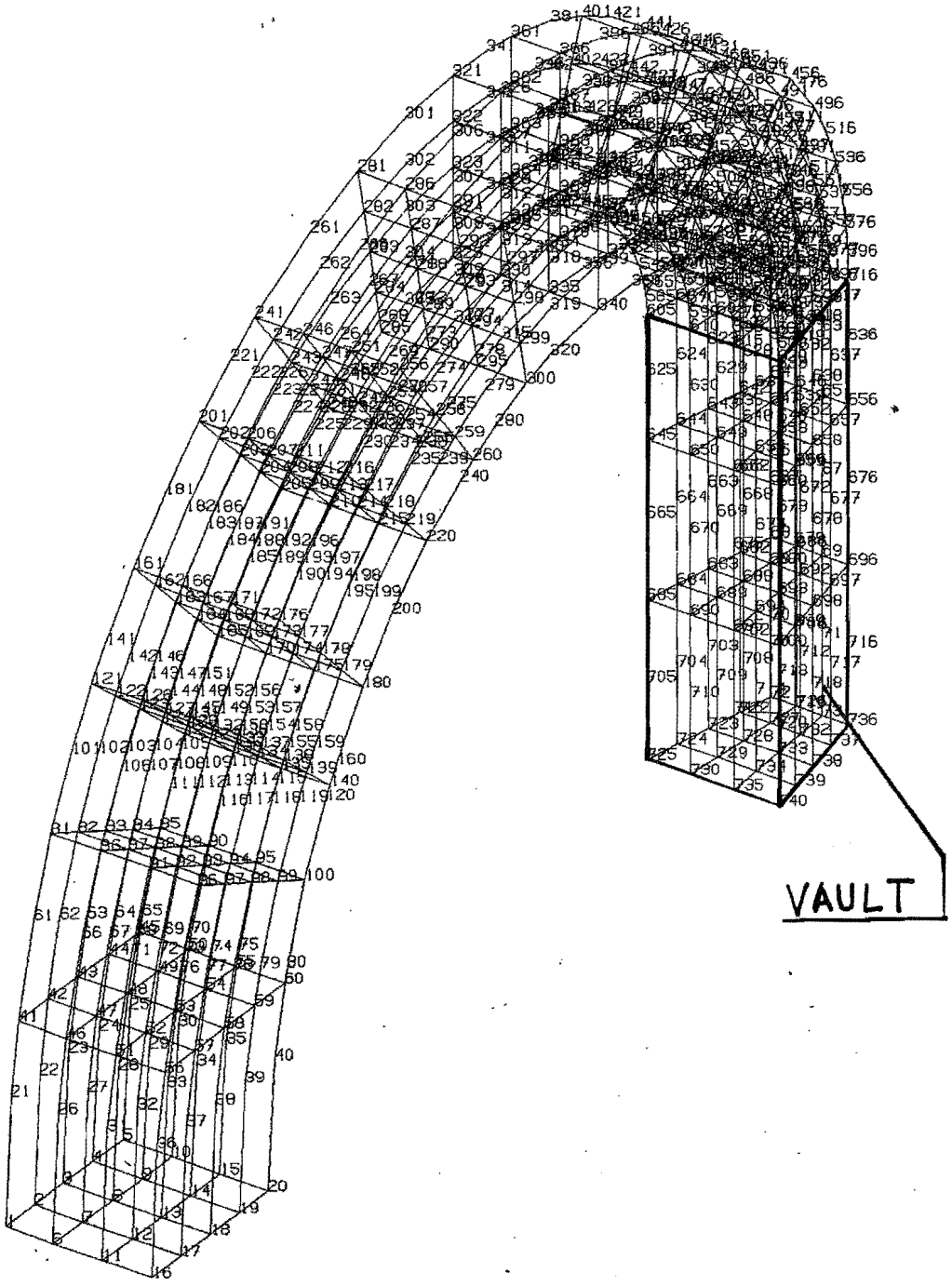

Fig. 3.1.15: Three-dimensional subdivision of a TF coil.

$$\tau = \sqrt{\tau_{zx}^2 + \tau_{zy}^2} \qquad I_p B_o = 4\,MAT$$

$$\tau_{max} = \tau_{20} = 11{,}5\ MPa$$

$$\Delta\tau = 0{,}57\ MPa$$

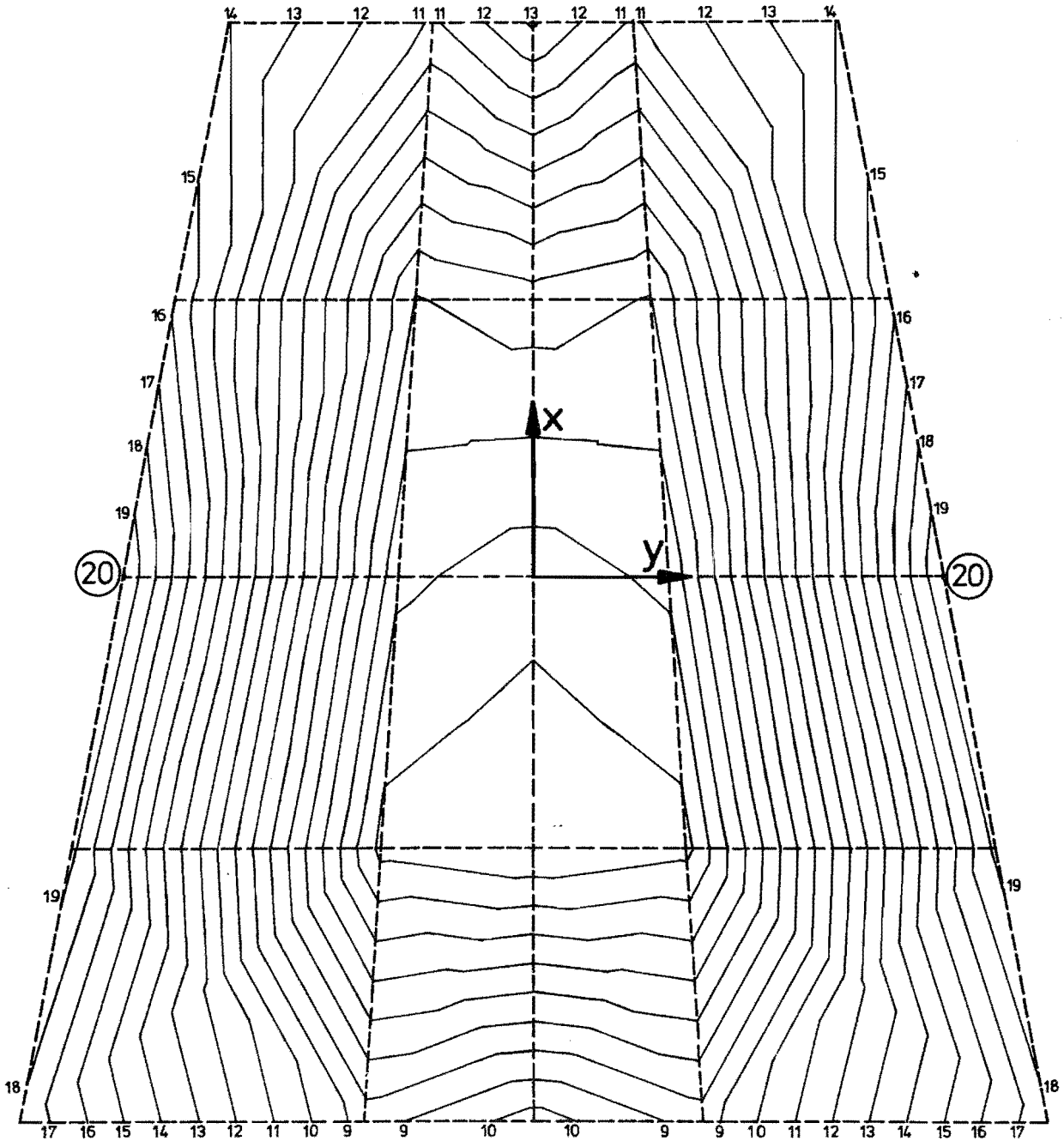

Fig. 3.1.16: Lines of constant in-plane shearing stresses for the SNA case.

Equivalent strain (ε_{eq})

$$(1-\nu^2)\,\varepsilon_{eq}^2 = (1-\nu+\nu^2)(\varepsilon_x^2+\varepsilon_y^2) + (1-\nu)^2\left(\frac{3}{4}\gamma_{xy}^2 - \varepsilon_x\cdot\varepsilon_y\right)$$

max ε_{eq} = $\varepsilon_{eq\,\underline{20}}$ = 3,6 ‰

$\Delta\varepsilon_{eq}$ = 0,18 ‰

max ε_{eq} = $\varepsilon_{eq\,\underline{20}}$ = 5,9 ‰

$\Delta\varepsilon_{eq}$ = 0,3 ‰

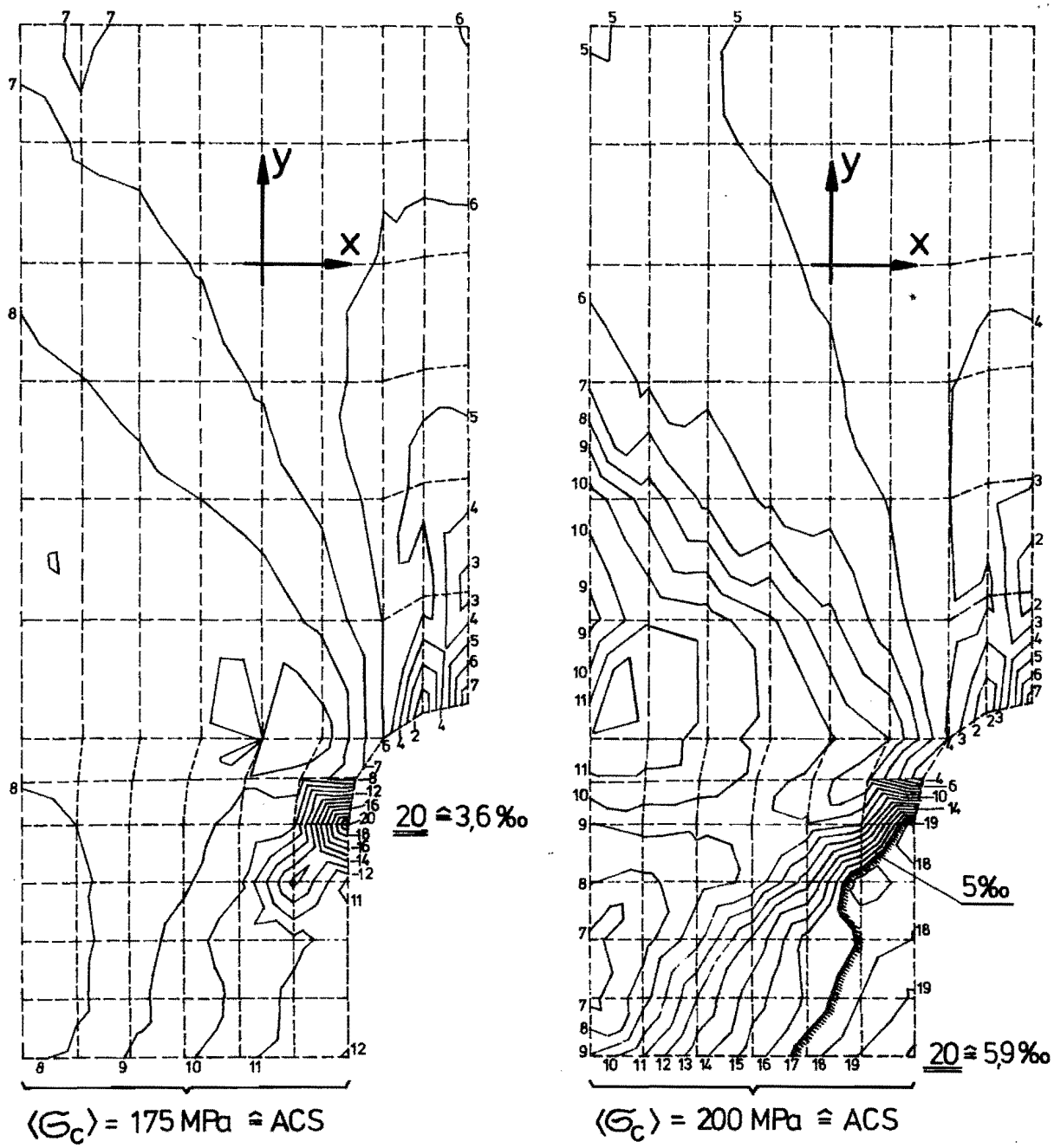

Fig. 3.1.17: Lines of constant nonlinear strain

$\sigma_{lin.}$ = 200 MPa $E_{lin.}$ = $1{,}25\times10^5$ MPa

$E_{lin.}$ / $E_{workhardening}$ = 50

3.2 The Poloidal Field (PF) System

The PF system consists of the ohmic heating (OH) system and the multipole (or vertical) V-coil system. The OH system serves for breakdown, plasma current build-up, ohmic heating and resistive current drive. The central transformer coil OH 1 provides for this purpose $\Phi_{OH} = 9.5$ Vsec. Two additional coils OH 1 and OH 2 shape the stray flux such that the field is reduced to $< 5 \cdot 10^{-3}$ T in the plasma region.

The vertical field system consisting of three coil types produces the desired SN, DN or L configurations. The coils V1 determine essentially the stagnation point, V 2 the horizontal equilibrium and V 3 essentialy the plasma shape (triangularity). The time dependences of OH and V coil excitations are different. Fig. 3.2.1 shows the position of OH and V coils. All coils are located outside the TF magnet.

3.2.1 Plasma Configurations and Currents

The poloidal field (PF) requirements of double null (DN), single null (SN) divertor and pump limiter configurations have been examined for ASDEX UG at low and high β_{pol} values using the Garching equilibrium code. The results are valid both for rather flat ($j \sim \psi - \psi^2$, ψ: poloidal flux function) and more peaked toroidal current densities ($j \sim \psi$). The comparison of these configurations has been done by looking for the largest plasma volume under the following constraints. The same coil positions outside the toroidal field coils for the divertor, shaping and equilibrium currents, are used and optimized with regard to the PF requirements (current I_M, power, energy and material). The plasma diameter in the torus midplane is not smaller than 1 m to get a sufficiently high line density $\bar{n}\cdot a$ necessary for a dense scrape-off layer. The size of the TF coils and a sufficiently large divertor chamber in the divertor cases allow a maximal height of the stagnation points of 0.85 m. The outermost flux surface of the scrape-off layer must not touch the vessel walls and installations like the passive stabilization loops. The resulting poloidal flux surfaces for a medium β_p-value of about 2.2 are shown in Figs. 3.2.2 - 4 together with the positions of the PF coils chosen and the PF currents necessary for 1 MA toroidal plasma current . The position of the scrape-off layers in the divertor chamber is the same for DN and SN cases, so that the same target plates can be used. Just one divertor coil above and one below the TF magnet is used to reduce the necessary sum of PF currents, the penalty being less flexibility in varying the radial position of the stagnation points. (Distant PF coils determine simultaneously the shape of the

interior flux surfaces and the position of the stagnation points.)

For a DN divertor plasma equilibrium with a half-axis ratio b/a ≈ 1.6 and strong triangular deformations δ = c/a ≈ 0.3 - 0.4 (see Fig. 3.2.2) result. The triangularity helps to reduce the unstable forces of the vertical displacement mode (see sect.3.2.7), but the currents in the PF coils have to produce in this case mainly a hexapole field, which, because of the large distance between plasma and the coils, dominates the PF requirements ($\Sigma |I_M| = 12 - 14 \times I_p$).

For the SN configuration the magnetic axis was moved into the upper vessel half, opposite the stagnation point. This reduces the necessary divertor current. An increase in the plasma volume of 15 % compared with the DN case and a reduction of the PF coil currents by a factor of 2 - 3 ($\Sigma |I_M| = 4.5 - 5.5 \times I_p$) was so possible. The stability of the vertical displacement mode for the SN and DN configurations, as shown in Figs. 3.2.2 and 3.2.3, is the same, as the smaller triangularity of the SN case is compensated by a smaller elongation.

Pump limiter configurations with a half-axis ratio of about 1.6 and a triangularity of $\delta = 0.1$ have nearly the same poloidal flux pattern in the plasma interior as the SN plasma and require therefore fairly similar PF currents ($\Sigma |I_M| = 3.5 \times I_p$). Both configurations differ in their plasma shape only little, and only small modifications of the PF coil currents are necessary to get the identical plasma surface in the upper half. The shift of the plasma center relative to the center of the PF coil system in the SN divertor case produces, however, a top-bottom asymmetry in the PF currents and quadratic measures of the coil currents, like the magnetic energy, change stronger than the sum of the ampere turns. These results are confirmed by our INTOR studies, where there is again only a 30 % difference in the external currents needed for producing a D-shaped pump limiter configuration and a SN configuration.

The PF coil distribution chosen allows the investigation of many other configurations with different ellipticities and triangularities. Reducing the higher PF moments dominating the dipole currents results in a circular plasma cross-section with only $\Sigma |I_M| = 1.5 \times I_p$.

Comparing the DN and SN configurations, the studies showed that an SN configuration is , indeed, by far optimal from the point of view of PF requirements. This justifies to concentrate in ASDEX UG on it and on the corresponding pump limiter configuration. The relatively minor difference in the MAT requirements between divertor and pump limiter

configurations also underlines the reactor potential of the former SN divertor configuration.

3.2.2 Basic Features of the PF Coils

The poloidal field coils are multi-windings circular coils which are inseparable units. They are wound from water-cooled copper conductors each winding layer being a cooling circuit with inlet and outlet. Care was taken to decouple different force components and forces as far as possible. Free thermal expansion wherever possible and homogeneous cooling should avoid thermal stresses. Thermal stressing of the insulation is limited by a maximum permissible temperature of T = 353 K.

High electric stresses occur by inductive voltage drop at the coil connections during excitation and de-excitation. Escessive electric load is avoided by means of protection switches. Fault conditions as well as excessive currents shall be avoided by a monitoring and safety control system. The OH coils are connected in series and also corresponding V-coils in the lower and upper half of the torus for symmetric DN and L configurations. Characteristic time-dependent OH flux and V coil currents are shown by Figs. 3.2.5 and 3.2.6. The maximum PF coil currents are indicated in Fig. 3.2.7.

3.2.3 The OH System

The OH system consists of the central transformer coils OH1, OH 2 and OH 3. The flux swing of 9.5 Vs is predominantly produced by the OH 1 coil, whereas the OH 2 and OH 3 coils serve to reduce the vacuum magnetic flux density to less than 3×10^{-3} T in the plasma region (Fig. 3.2.8) for maximum OH 1 excitation ($\Phi_{c_H} = \pm$ 4.5 Vs).

Of the several concepts for the OH 1 coil that were investigated, the simplest version comprising a 3 m long solenoid with a ratio of inner to outer radius of k_d = 0.5, was chosen. This is a good compromise between the mechanical and thermal loads and leads to negligible radial stresses. Since the mechanical stress is finally limiting a symmetric flux swing of $\Delta\Phi_{c_H} = 4.25$ Vs was chosen.

The choice of a winding current of I = 47 kA for the series-connected coils was governed by the following facts:

- The IPP generators and switching units are geared to 47 kA.
- For current switching and breaking conventional vacuum switches and thyristors can be used for this current value.

- The maximum voltage occurring in the OH 1 coil windings (at the moment of ignition) is still uncritical.

- The copper filling factor with this winding number is still sufficiently high to ensure the required mechanical stiffness of the coil.

The electrical stress of the OH system depends on the maximum dI/dt of the OH current necessary to induce a sufficiently high plasma voltage VP to cause plasma breakdown. Of special interest was the evaluation of the influence of the vacuum vessel, acting as a transformer secondary winding, on the breakdown voltage. A model circuit, including the OH coils, the V coils, the plasma, and the vacuum vessel, was investigated with the aid of the ECAP network analysis programme.

As shown in the circuit diagram of Fig. 3.2.9, the vacuum vessel was simulated with four coils, i.e. with their L and R elements connected in parallel. Geometrically, they were arranged in such a way that the D-shaped cross-section of the vessel was approximated by a rectangular one (Fig. 3.2.9). The values of the resistances RG 1 to RG 4 correspond to a vessel made of stainless steel and containing 4 bellows distributed on the toroidal circumference. The total toroidal resistance of this vessel is 0.25 mΩ. The plasma itself was simulated on the toroidal circumference by its open-ended inductance only. For the calculations this means that the circuit diagram is valid until the plasma breakdown voltage VP is reached. From experience with the ASDEX experiment, a plasmaloop voltage of 50 V is assumed to be sufficient.

Inducing a 50 V plasma voltage requires that the overall insulation of the OH coils has to withstand a voltage of about 30 kV. Figure 3.2.10 shows the dependence of the OH coil voltage and the plasma loop voltage versus discharge resistance. The vessel resistance parameter is 0.25 mΩ. The influence of the vessel resistance on the plasma loop voltage is given in Fig. 3.2.10a. The discharge resistance parameter is 0.6Ω.

The OH 1 coil is designed as a helically wound coil consisting of 10 cylindrical layers with 51 windings each. SE Cu F 25 was selected as conductor material. The single cylinders are internally connected with the exception of the high-voltage-insulated main connections at the 1st and 10th cylinder. The winding and coil insulations consist of fibre-glass-reinforced epoxy resin with cast-in polyimid foils for improved electric breakdown strength. The insulation thickness is 2.5 mm. The outer coil insulation is to be covered with a conducting graphite layer to avoid

surface breakdown.

Each winding cylinder has its own cooling circuit such that inlets and outlets are arranged on the upper and lower coil front ends. The water connections are designed to withstand the maximum voltage occurring in the coil.

The cooling channels have elliptical cross-sections. The winding conductor cross-section (2.2 x 5.5 cm^2) is deformed during bending, so that trapezoidal conductors have to be used to obtain rectangular winding cross-sections in the coil compound. The exact conductor form is being determined at present by testing. The limited length of the conductors makes it necessary to braze them. In order to restore the original strength the brazed sections will be cold-worked by stretching.

The cooling channels and water pressure (Δp = 20 bar) are determined by a cooling-down time of 10 min. In order to ensure homogenous temperatures during cooling, the water flow is reduced with baffles for the inner winding cylinders, which carry lower thermal energy. This allows equal conductors to be used throughout the coils.

The maximum thermal load of ΔT = 60 deg. is reached for $j^2 \cdot \Delta t_{\sqcap\!\sqcup}$ = 110 $(kA/cm^2)^2$ x s, where $t_{\sqcap\!\sqcup}$ is an equivalent flat-top time. The permissible value for SN discharges and Φ_{OH} = 9.5 Vs is $t_{\sqcap\!\sqcup}$ = 5.5; for DN discharges and Φ_{OH} = 8.5 Vs it is $t_{\sqcap\!\sqcup}$ = 6.5 s.

During excitation the coil expands radially and vertically. The diameter increases by 2 mm at maximum load due to mechanical and thermal stresses which act in the same direction. Mechanical and thermal stresses act vertically in opposite directions. Elastic bearings at the coil front ends take up the 5 mm vertical length variation and also allow free radial expansion.

The requirements imposed on the OH 1 coil apply essentially to the OH 2 coil as well, but to a reduced extent. Spatial constraints require this coil to be wound on radial discs. It consists of 9 pancakes of 9 windings each, each pancake having its own cooling circuit. The water inlet is positioned radially outside the coils and the outlet inside the coil. The cooling channels are therefore of equal length and are evenly distributed, so that thermal stressing of the insulation is minimized. Details are given in Tables 3.1 to 3.3.

The OH 3 coil is to be wound as one-layer disc. It is reinforced by mounting it to the V 2 multipole coil in a way which allows horizontal sliding between the two coils.

In order to feed the OH coils, magnetic fields of up to 6 T have to be crossed with conductors carrying currents of about 47 kA. As the poloidal field to be crossed has no component in the toroidal direction and the currents in the lead-ins flow in either the radial or the vertical direction, only forces in the toroidal direction are produced. The maximum line load acting on the single conductors is 0.3 MN/m length. For the lead-in as a whole, where the incoming and outgoing conductors are mechanically connected, the forces cancel one another to a large extent. Only forces due to poloidal field inhomogeneity remain.

3.2.4 The Vertical Field Coils

In dimensioning the vertical field (V) coils, symmetric and unsymmetric load conditions had to be considered, and also a larger safety margin compared with the OH coils. The latter is caused by an uncertainty of $\leq$ 10 % of the multipole current calculations. Furthermore, it is desirable that the V coils operate on the average at lower current density in order to reduce the ohmic losses since the inductive excitation energy is already appreciable.

All V coils are arranged outside the TF magnet, but as closely as possible to the torus structure. The coil concept is based on simple and standard technique. All coils are composed of radially wound pancakes connected at their outer and inner circumference.

The conductor cross-sections were dimensioned to allow a circular cooling channel bore. SE Cu F 25 was again selected as material. The insulation consists of fibre-glass-reinforced epoxy resin. Only at the connections is additional insulation required in the form of polyimid foils.

The water cooling is provided in the pancake layers with inlets and outlets at the outer and inner circumference. The lengths of the cooling channels do not allow stationary conditions during excitation. The thermal radial expansion, however, is only 2.5 mm, i.e. one-fifth of the expansion produced by the Lorentz force. The coil support has to allow movements of 40 mm in diameter in a way which again guarantees concentric positioning after cool-down. Cooling requires intervals of $\leq$ 10 min betwen discharges.

3.2.5 Loads and Stresses of Poloidal Field Coils

Thermal stresses are reduced to their minimum values by allowing free expansion wherever possible. The retarded temperature rise of the insulation compared with the

conductor produces stresses within the insulation. However, since the thermal expansion is a small fraction of the expansion and strain produced by the I x B forces, thermal stresses have been taken into account by sufficiently enlarging the safety margin.

The I x B forces acting in the radial and vertical directions are balanced radially by hoop stresses and vertically by a support structure. Sixteen supports resting on the circumference reduce bending stresses to < 10 MPa.

The different load conditions and the direction of vertical forces (up or down) depend on the configuration (SN, DN), the OH coil excitation level and sign, and the plasma beta. An analysis identified all 11 critical load cases, not including fault conditions. Tables 3.4 and 3.5 show a survey of these load cases, indicating maximum values of the integral vertical coil forces Fz and the radial coil force densities F_R . The vertical forces of the single conductors of some coils act against each other. So the maximum force Fz inside the V 1 and also V 2 coils will be nearly 65 MN stressing the isolation. The spatial force distribution is shown in Fig.3.2.11 for the critical load case for the support structure.

Figures 3.2.12 to 3.2.14 show the vertical load in time Fz(t) introduced by each coil for the DN1 and SN2 modes of operation. The maximum load occurs in all cases at the end of the flat-top phase. The KOK computer code served for the force calculations.

All stresses of the V coils were analytically calculated. This was justified by the satisfactory comparison of FE calculations with analytical calculations of the OH 1 coil stressing, this being the coil with the most critical stress distribution. The maximum conductor stresses in the center of the OH 1 coil are calculated to amount to 130 MPa. The shear stress is less than 1.5 MPa.

3.2.6 The Poloidal Field Coil Support Structure

3.2.6.1 Design Requirements

The poloidal coil system consists of two independently excited coil systems:

- the vertical field system (coils V1 to V3);
- the ohmic heating system (OH1 to OH3).

Both coil systems underlie mechanical and thermal stresses during excitation of different time sequence. The Lorentz forces for different modes of excitation are given by Table 3.4. A cylindric framework with 16 radial beam on top and bottom was conceived in order to balance these forces. The design requirements for this framework were, in particular:

- a precise spatial positioning of the PF coils;
- balance of the vertical loads without major deformations < 10 mm;
- avoidance of additional stresses, i.e. free thermal expansion and mechanical deformation in radial direction;
- simple assembly procedure;
- compatibility with modular assembly concept of the TF coil system;
- sufficiently low permeability 1.01 to 1.03;
- large toroidal resistance;
- sufficient safety margin of the cyclic loads to the fatigue limit.

3.2.6.2 Description of Support Solution

The characteristics of the support structure design which fulfills these requirements are (Fig. 3.2.15):

- selfsupporting framework composed of two wheels each, with 16 double T-beam spokes;
- both wheels are rigidly connected by 16 vertical beams

at the periphery and in the centre, torque-free, by a steel spindle;

- two nuts connect spindle and wheels free from backlash;

- for compensation of radial tolerances serve wedges (two per spoke), which also provide access to the interior of the machine in case of failure;

- the combined forces of OH and V coils can produce tension and compression in the central axis of the support frame. The spindle, provided for tension only, is therefore encompassed by slit steel cylinders which hold the OH1 and OH2 coils and balance the compression load. In order to provide backlash-free force flow, prestressed rubber elements are foreseen;

- the electric insulation is provided at the front end of the spoke beams and the radially adjustable wedges;

- the selfsupporting framework is carried by 8 vertical beams.

3.2.6.3 Stress Analysis

The maximum load occurs for single null (SN) and double null (DN) (case 4, Table 3.4). The resulting stresses and deformations calculated by a FE beam model are summarized in Table 3.6. The deformation of the framework under SN and DN load is shown in Figs. 3.2.16 to 3.2.18. The internal force distribution (normal force N, transverse force Q and bending moment Mb) is shown in Figs. 3.2.19 to 3.2.20.

3.2.6.4 Materials

The double T-beams shall be fabricated from austenitic steel 1.4311 (X 2 Cr Ni N 1810) with

- yield point = 270 MPa

- tensile strength = 550 to 750 MPa

- ductile yield = 40 %

The central column (spindle) shall be produced from austenitic steel 1.3964 (X 50 Cr Mu NiN 229)

- yield point = 540 MPa

- tensile strength = 880 - 980 MPa

- ductile yield = 40 %.

Both steels shall be used in quenched condition.

Overall dimensions of structure:

- diameter 8.5 m
- height 8.4 m
- weight 120 tons.

Table 3.6

load case 4	stress MPa beam	stress MPa spdl.	vertical displacement in mm at position V1o	V2o	V3o	V1u	V2u	V3u	strain mm spdl.
DN	140	300	4.7	2.0	0.06	-4.6	-1.9	0.07	8.0
SN	133	285	1.8	0.5	-0.1	-4.6	-1.3	-01.	7.6

max combined stress (van Mieses).

3.2.7 Plasma Stabilization and Feedback Systems

In ASDEX UG the radial and vertical position and the shape of the plasma cross-section have to be controlled by active feedback, with time constants increasing in that order. The position controls have to avoid uncontrolled wall contact at unforeseen locations, whereas the shape control is necessary to keep the plasma dimensions and the divertor configurations fixed.

The shortest control times are necessary for possible radial displacements which are due to fast variations of internal parameters (l_i or β_p). They are caused by MHD manifestations like internal sawteeth, minor disruptions, or like the new phenomena observed in discharges with high-power additional heating ("fishbones" in PDX; sawtooth-like variations in the energy content of the near-boundary region in ASDEX). Control of the resulting horizontal plasma displacement may be essential for avoiding strong plasma-wall contact triggering a subsequent major disruption. Shafranov's formula predicts in that case (for constant applied B_v and I_p) a major radius reduction of the plasma column by

$$\frac{\delta R}{R} = \frac{1}{1-n} \frac{\delta\beta_p + \frac{1}{2}\delta l_i}{\ln\frac{8R}{a} + \beta_p + \frac{l_i}{2} - 1.5}$$

where $n = -d\ln B_y / d\ln R$ is the usual decay index.

In ASDEX UG the negative decay index ($n = -0.5$) associated with the vertically elongated plasma considerably enhances the stiffness of the configuration against radial fluctuations compared with a circular plasma ($n = +0.5$). A modest change in β_p ($\delta\beta_p = 0.2$) would produce (at $\beta_p = 2$) a plasma shift of about 4 % of the major radius even without passive structures ($\delta R \leq 6$ cm). The stagnation point and the intersection points between the scrape-off layer and the target plates change much less than the plasma axis ($\sim 2 - 3$ cm). These simple estimates have been verified also by a sequence of equilibrium calculations with different β_p and shifted magnetic axes. These displacements would seem tolerable particularly in view of the relatively large distance plasma boundary - vessel wall, but have to be reduced in view of the ICRH antennae. Controlling the currents in the V 3 coils by less than 20 kA keeps the plasma column nearly fixed.

In case the plasma is not up-down symmetric, these manifestations may also lead to rapid changes of the vertical position. In fact the vertical and horizontal movements are no longer decoupled.

Vertical displacements will be caused primarily by the inherent positional instability of the elongated plasma column in ASDEX UG on the microsecond time scale. Increasing the half-axis ratio and/or reducing the triangularity increases the destabilizing force. This MHD instability can be stabilized by passive conductors at least on the time scale of these passive conductors. The resulting residual growth rate is given by

$$\gamma = \frac{1}{\tau_R} \frac{1}{\frac{F_{stab}}{F_{vert}} - 1}$$

where τ_p is the L/R time constant of the passive system, F_{stab} the stabilizing force of the currents induced in the passive conductors and F_{vert} the destabilizing force without any passive stabilization (see also sect. 3.2.8). In this model the plasma moves as a rigid conductor and no plasma currents are induced. The currents induced in the vessel walls are not sufficient to yield $F_{stab} > F_{vert}$ due

to their relatively large distance. Moreover, their decay time is short ($\approx$ 10 ms), so that the feedback power would be excessive. Separate passive loops consist of toroidal segments with low inductive up-down electrical connections which permit saddle currents to flow. An optimization of the position and the minimum number of such conductors has been made providing a sufficient stability margin ($F_{stab} > 1.5\ F_{vert}$). Three passive loops (diameter 0.1 m) located above and three below the torus midplane at the torus outside under about $\pm$ 60° from the plasma centre (see Fig. 3.2.21) having an average distance from the magnetic axis of 0.7 m are sufficient for passive stabilization of the single null, double null and the pump limiter configurations. The residual growth rates depend on the number of the up-down return conductors used and are lower than 10 s^{-1}.

This residual growth has then to be stabilized by an active feedback system. The location of the feedback conductors should be as close as possible to the plasma in order to reduce the power. On the other hand, in a fusion reactor it would be desirable to place the active coils far away from the plasma to reduce the radiation level for the necessary insulators. For ASDEX UG two positions of the active coils (consisting of one coil above and one below the torus midplane) have been considered, one within the TF coil (1 m distance from the plasma centre) and one outside the TF coil (2.2 m distance, see Fig. 3.2.21). A model including the circuit equations of passive and active coils and a rigidly moving plasma has been studied numerically. The active amplifier includes a position, velocity and excursion integrated feedback gain (PID controller). $U_{FB} = -Gz - G\dot{z} - G_{\int} \int z dt$. The condition for the adjustment of the gains has been to produce a damped response of the system whose decay time equals the residual growth times of the passively stabilized vertical motion 1/ , yielding the following gain factors: internal feedback coil $G > 200$ V/m; $25 < G_V < 100$ Vs/m; external feedback coil $G > 600$ V/m; $50 < G_V < 150$ Vs/m. Assuming an initial velocity of the plasma column with $v = 0.05 \ldots 0.5$ m/s the maximum excursions of the plasma position are below 1.5 cm. The voltages and powers necessary for 1 MA plasma current are at about 10 V and 200 kW for the inner feedback loops and 40 V and 4 MW for the external feedback loops. The requirements of the active control power depend proportionally on the squares of the initial plasma velocity and the toroidal plasma current, decrease strongly with increasing maximal plasma excursion, depend approximately inversely on the passively reduced vertical growth rate and increase strongly with the distance of the active control coils from the plasma centre, as is shown by the examples. A limited feedback response due to a capacitive term in the feedback transfer function is not critically as long as this time constant is shorter than 40 msec.

The times for shape deformations and current diffusion

are in the second range.

3.2.8 Stabilization Loops

Stabilization loops are passive single-turned poloidal field coils exclusively linked with the radial component of the poloidal field, so that a vertical plasma motion induces currents in them which are directed to counteract that motion. They are required to slow down the extremely high growth rate of the vertical position instability of an elongated plasma to values which can be controlled by an active feedback mechanism. To accomplish this function, the loops must be designed to satisfy the condition (see sect.3.2.7).

$$f = \frac{F_{Stab}}{F_{vert.}} = \frac{J_p \left(\frac{\partial M}{\partial z}\right)^2}{2\pi R_p \left(\frac{\partial B_r}{\partial z}\right) L} > 1$$

where L means the self-inductivity of the loops and $\partial M/\partial z$ the rate of change of the mutual inductivity between the plasma and the loops with the vertical plasma position.

Put in the actual values of ASDEX UG, the condition reads:

$$f = \frac{F_{Stab}}{F_{vert.}} = \frac{\left(\frac{\partial M}{\partial z} / \frac{\mu H}{m}\right)^2}{L/\mu H} > 1$$

The resulting growth rate becomes

$$\gamma = \frac{1}{\tau_R (f-1)} \quad \text{with} \quad \tau_R = \frac{L}{R}$$

which calls for a resistance R of the stabilization loops as small as possible and for a clear satisfaction of the condition by an appropriate choice of the position of the coil. $\Lambda f>1$

For ASDEX UG the proposed arrangement (see Fig. 2.4) has proved to be the only one by which this condition can be fulfilled without intercepting the plasma scrape-off layer by the loops. It yields :

$$f = \frac{F_{Stab}}{F_{vert}} \approx 1,6$$

and depending on some details of the final design, a resulting growth rate of

$$\gamma \approx 5 \ldots 10 \ sec^{-1}$$

These values are not greatly affected by combining the 3 separate conductors each loop was assumed to consist of (Fig. 3.2.21), to a single constructive unit. This was necessary for a realizable constructive concept which meets the additional requirements on strength and diagnostic access.

For safety reasons the mechanical design of the loops must be based on the relatively high force load which will appear if the active feedback circuit fails to operate properly. Assuming a possible free plasma motion without contact to any limiting material of 0.15 m a current of at least 70 kA (for I_p = 2 MA) will then be induced in the loops leading to forces which are shown in Fig. 3.2.22. These forces are too large to be absorbed or even to be led into the outer structure of the experiment by the relatively fragile vacuum vessel. Therefore the forces, as far as their radial components are concerned, must be taken up by the stabilization loops themselves and, as far as the net vertical forces are concerned, a separate support structure must be provided to lead them through four of the eight large vessel ports in the outer structure of the experiment. Thus a total mechanical and thermal decoupling of the stabilization loops from the vacuum vessel can be achieved. Figure 3.2.23 shows the schematic setup of the total passive stabilization system. Its present design is largely determined by efforts to avoid any limitation of the diagnostic access to the plasma. It consists of four single loops of different size mechanically combined by four bridges which provide the electrical connections between the upper and lower parts of the loops and accommodate at the same time the necessary electrical insulation between the loops. The arrangement corresponds to the electrical partition of the vessel and allows to dispense with any insulation between the loops and the vessel.

To meet the requirements on conductivity and strength, the conductor must probably be made of copper. Its use yields presently some margins, as a first stress analysis has shown. This might be very helpful in the further course of the design when coping with some problems in more detail like current bridges, cooling measures or soluble connections required by assembly needs. Anyway, the conductors must be shielded against the energy flux from the plasma to limit the sputtering effects. This will be achieved by covering the coils with a graphite layer. To avoid too large temperature excursions, active cooling might be necessary.

Poloidal - Field - Coils

Set up Disposition

Tab. 3.1

PF COIL	Ra cm	Ri cm	L_{ges} cm	B_{ges} cm	D cm	$S_{Lt;Is}$ Leiter cm	S_{spIs} Spule cm	L_{Lt} cm	B_{Lt} cm	A_{Lt} Cu cm	f_{ges} -	Wght cu Mp				
OH 1 o	51	25,5	150	25,5	+ 75	0,125	0,5	5,5	2,2	10,2	0,68	11,14				
OH 1 u					- 75											
OH 2 o	79	53,5	63,5	25,5	+ 196	0,15	0,5	6,64	2,15	13,71	0,677	4,1				
OH 2 u	"	"	"	"	- 196	"	"	"	"	"	"	"				
OH 3 o	329,5	280,5	4	49	+ 188,5	0,15	0,5	2,7	7,7	18,43	0,47	1,6				
OH 3 u	"	"	"	"	- 188,5	"	"	"	"	"	"	"				
V1 o	196,2	123,9	34	72,3	+ 234	0,15	0,5	5,2	3,0	13,95	0,681	15,0				
V1 u	"	"	"	"	- 234	"	"	"	"	"	"	"				
V2 o	329,5	280,5	41	49	+ 166	0,15	0,5	4,7	4,5	17,35	0,622	21,3				
V2 u	"	"	"	"	- 166	"	"	"	"	"	"	"				
V3 o	369,5	340,5	21	29	+ 60	0,15	0,5	3,7	3,7	11,15	0,549	6,65				
V3 u	"	"	"	"	- 60	"	"	"	"	"	"	"				
Plasma																

Poloidal - Field - Coils

Tab. 3.2

Characteristic Data

						SN 2				DN 1						
PF COIL	cyld. -	pan cake -	N_{cyld} -	N_{Pc} -	N_{coil} -	$\Delta\hat{\phi}_{OH}$ Vs	$N_{coil} \times \hat{I}_{Lt}$ KA	$\hat{I}_{Lt}$ KA	$\hat{j}_{cu}$ KA cm^{-2}	$\Delta\hat{\phi}_{OH}$ Vs	$N_{coil} \times \hat{I}_{Lt}$ KA	$\hat{I}_{Lt}$ KA	$\hat{j}_{cu}$ KA cm^{-2}	R_{293} mΩ	L mH	
OH 1 o	10	-	51	-	510	9,5	11997	47	4,6	8,5	10734	42	4,12	20,3	60,9	
OH 1 u																
OH 2 o	10	-	8	-	80		3764	47	3,43		3368	42	3,07	4,1		
OH 2 u	10	-	8	-	80		3764	47	3,43		3368	42	3,07	4,1		
OH 3 o	-	1	-	5	5		235	47	2,55		210	42	2,28	0,88		
OH 3 u	-	"	-	5	5		235	47	2,55		210	42	2,28	0,88		
V1 o	-	6	-	20	120	-	1870	15,6	1,12	-	4752	39,6	2,84	14,7	62,9	
V1 u	-	"	-	"	120	-	5773	48,1	3,45	-	4752	39,6	2,84	14,7	62,9	
V2 o	-	8	-	9	72	-	-880	12,2	0,7	-	-3643	50,6	2,92	13,5	58,7	
V2 u	-	"	-	"	72	-	-3766	52,3	3,02	-	-3643	50,6	2,92	13,5	58,7	
V3 o	-	5	-	6	30	-	-990	33,0	2,96	-	1210	40,3	3,62	10,2	15,5	
V3 u	-	"	-	"	30	-	-770	25,7	2,3	-	1210	40,3	3,62	10,2	15,5	
Plasma							2000				1200					

Poloidal - Field - Coils

Tab. 3.3

	Heating SN2				Heating DN1				Cooling							
PF COIL	t_{BrDr} s	$t_{\sqcap}$ ($\hat{I}_{Lr}$) s	ϑ_A K	$\Delta\vartheta$ adb. grd	t_{BrDr} s	$t_{\sqcap}$ ($\hat{I}_{Lr}$) s	ϑ_A K	$\Delta\vartheta$ adb. grd	N_{cool} -	Δt_{cool}	$\Delta\vartheta_{FIN}$ grd	v_{cool} cm s^{-1}	Δp_{cool} atm	d_H cm	d_{cool} cm	
OH 1 o	4	5	293	57	8	6,4	293	58	10	10	< 1	264 ÷ 450	4,7 ÷ 20	1,5	Ellipse 2,2/1	
OH 1 u																
OH 2 o				30				32	10			322 450	6,7 17	0,85	2x0,6	
OH 2 u				30				32	10					0,85	2x0,6	
OH 3 o				16				17	1			440	20	1.73	3x1,0	
OH 3 u	4	5	293	16	8	6,	293	17	1	10	< 1	440	20	1.73	3x1,0	
V1 o	4	7	293	4	8	9,6	293	41	12	10	< 1	550	20	1,45	1,45	
V1 u		5,3		33		9,6		41	12			550		1,45	1,45	
V2 o		3,8		1		9,9		45	8			550		2,2	2,2	
V2 u		2,8		12		9,9		45	8			550		2,2	2,2	
V3 o		5,0		23		4,6		31	5			550		1,8	1,8	
V3 u	4	5,2	293	14	8	4,6	293	31	5	10	< 1	550	20	1,8	1,8	
Plasma																

Poloidal-Field-Coils ; Critical vertical Loads

Tab. 3.4

	Load case 1		Load case 2				Load case 3				Load case 4					
PF	OH		V-Test DN		V-Test SN		V-Test DN		V-Test SN		Test DN		Test SN			
COIL	I(t2)		β=0.6 I(t3)	$F_{z\,coil}$ Mp	β=0.6 I(t3)	$F_{z\,coil}$ Mp	β=2,2 I(t4)	$F_{z\,coil}$ Mp	β=2.2 I(t4)	$F_{z\,coil}$ Mp	β=2.2 I(t12)	$F_{z\,coil}$ Mp	β=2.2 I(t8)	$F_{z\,coil}$ Mp		
OH 1 o	I_{max}	-773									$-I_{max}$	-1039	$-I_{max}$	-887		
OH 1 u		+773										1039		1146		
OH 2 o		-725										-1267		-975		
OH 2 u		+725										1267		1378		
OH 3 o		-18										-1167		-337		
OH 3 u	I_{max}	+18									$-I_{max}$	1167	$-I_{max}$	886		
V1 o			0,87 I_{max}	+625	0,75 I_m	+143	I_{max}	+854	I_{max}	+205	I_{max}	1903	I_{max}	618		
V1 u			0,87 I_m	-625	I_{max}	-1366	I_{max}	-854	0,95 I_m	-1046	I_{max}	-1903	0,95 I_m	-2260		
V2 o			I_{max}	+419	I_{max}	-303	I_{max}	-300	0,77 I_m	-368	I_{max}	581	0,77 I_m	985		
V2 u			I_{max}	-419	I_{max}	+1857	I_{max}	+300	0.63 I_m	+1560	I_{max}	-581	0,63 I_m	-208		
V3 o			I_{max}	-1119	0,22 I_m	-71	0,65 I_m	-619	I_{max}	-284	0,65 I_m	-631	I_{max}	-270		
V3 u			I_{max}	+1119	0,5 I_m	-260	0,65 I_m	+619	I_{max}	-66	0,65 I_m	631	I_{max}	-78		
Plasma																

	Load case 5				Load case 6											
PF	DN		SN		DN		SN									
COIL	β=2,2 I(t12)	$F_{z\,coil}$ Mp	β=2,2 I(t8)	$F_{z\,coil}$ Mp	β=0,6 I(t3)	$F_{z\,coil}$ Mp	β=0,6 I(t3)	$F_{z\,coil}$ Mp								
OH 1 o	$-I_{max}$	-951	$-I_{max}$	-740	-0,05 I_m	-125	-0,53 I_m	-197								
OH 1 u		951		999		125		332								
OH 2 o		-1223		-902		-180		-268								
OH 2 u		1223		1304		180		519								
OH 3 o		-1156		-317		-172		-175								
OH 3 u	$-I_{max}$	1156	$-I_{max}$	866	-0,05 I_m	172	-0,53 I_m	656								
V1 o	I_{max}	1748	I_{max}	516	0,87 I_m	513	0,75 I_m	243								
V1 u		-1748	0,95 I_m	-1962	0,87 I_m	-513	I_{max}	-1778								
V2 o		782	0,77 I_m	-140	I_{max}	584		-128								
V2 u	I_{max}	-782	0,63 I_m	768		-584	I_{max}	1108								
V3 o	0,65 I_m	-653	I_{max}	-223		-1148	0,22 I_m	-58								
V3 u	0,65 I_m	653	I_{max}	-114	I_{max}	1148	0,5 I_m	-277								
Plasma	1200		2000		1000		1600									

Poloidal-Field-Coils; Critical radial Loads; for currents see Tab.

Tab. 3.5

	Load case 2				Load case 3				Load case 4				Load case 5			
PF	D N		S N		D N		S N		D N		S N		D N		S N	
COIL	$F^{*}_{R\,int}$	$F^{*}_{R\,ext.}$	$F^{*}_{R\,int}$	$F^{*}_{R\,ext}$	$F^{*}_{R\,int}$	$F^{*}_{R\,ext}$	$F^{*}_{R\,int}$	$F^{*}_{R\,ext.}$ kp	$F^{*}_{R\,int.}$ cm^{-3}	$F^{*}_{R\,ext}$	$F^{*}_{R\,int}$	$F^{*}_{R\,ext}$	$F^{*}_{R\,int}$	$F^{*}_{R\,ext}$	$F^{*}_{R\,int}$	$F^{*}_{R\,ext}$
OH 1 o									31,6	2,0	32,1	2,4	30,4	0,7	30,2	0,2
OH 1 u									"	"	32,1	2,4	"	"	30,2	0,2
OH 2 o									13,3	-7,4	15,8	-4,8	13,1	-7,7	15,4	-5,2
OH 2 u									"	"	12,6	-8,3	"	"	12,1	-8,7
OH 3 o									4,1	-2,0	1,6	-0,3	4,1	-20	1,6	-0,3
OH 3 u									"	"	3,4	-1	"	"	3,4	-1
V1 o	6,4	-4,9	0,62	-0,64	8,1	-6,5	1,2	-1,1	8,2	-6,7	1,2	-1,1	8,3	-6,6	1,3	-1,1
V1 u	"	"	11,8	-9,7	"	"	11,2	-8,3	"	"	11,3	-8,4	"	"	11,5	-8,3
V2 o	6,5	-4,5	0,5	-0,18	6,9	-4,4	0,4	-0,1	7,1	-4,5	0,4	-0,1	7,0	-4,5	0,4	-0,1
V2 u	"	"	7,8	-4,3	"	"	3,4	-1,5	"	"	3,5	-1,6	"	"	3,5	-1,6
V3 o	4,3	-3,4	0,3	-0,15	1,8	-1,5	3,1	-2,2	1,8	-1,4	3,1	-2,2	1,8	-1,5	3,2	-2,1
V3 u	"	"	5,1	-3,5	"	"	1,9	-1,3	"	"	1,9	-1,4	"	"	2,0	-1,3
Plasma																

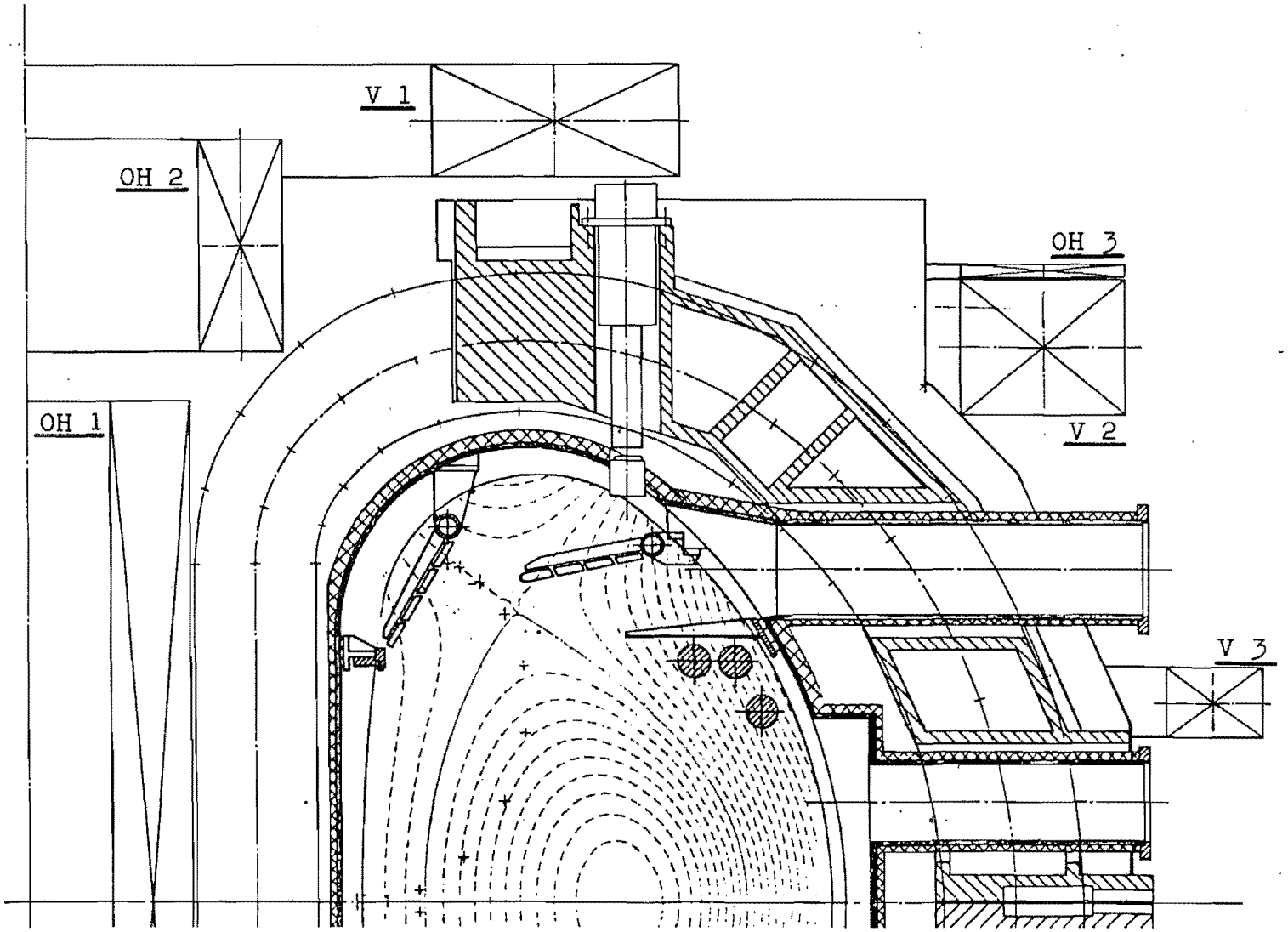

Set up Disposition of the Poloidal Field Coils

Fig. 3.2.1

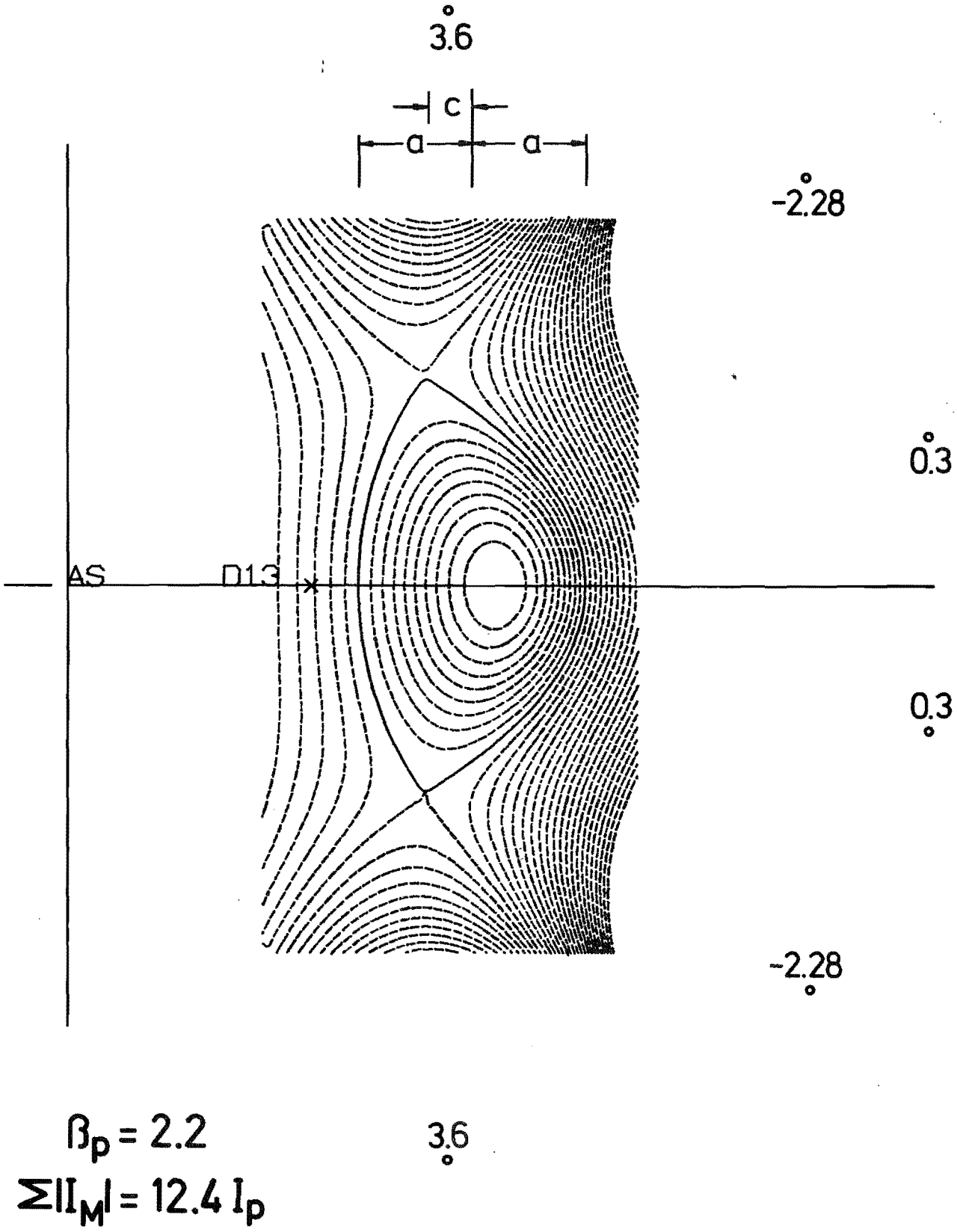

Fig. 3.2.2 Double Null Configuration for ASDEX Upgrade. The multipol currents given correspond to I_p = 1 MA.

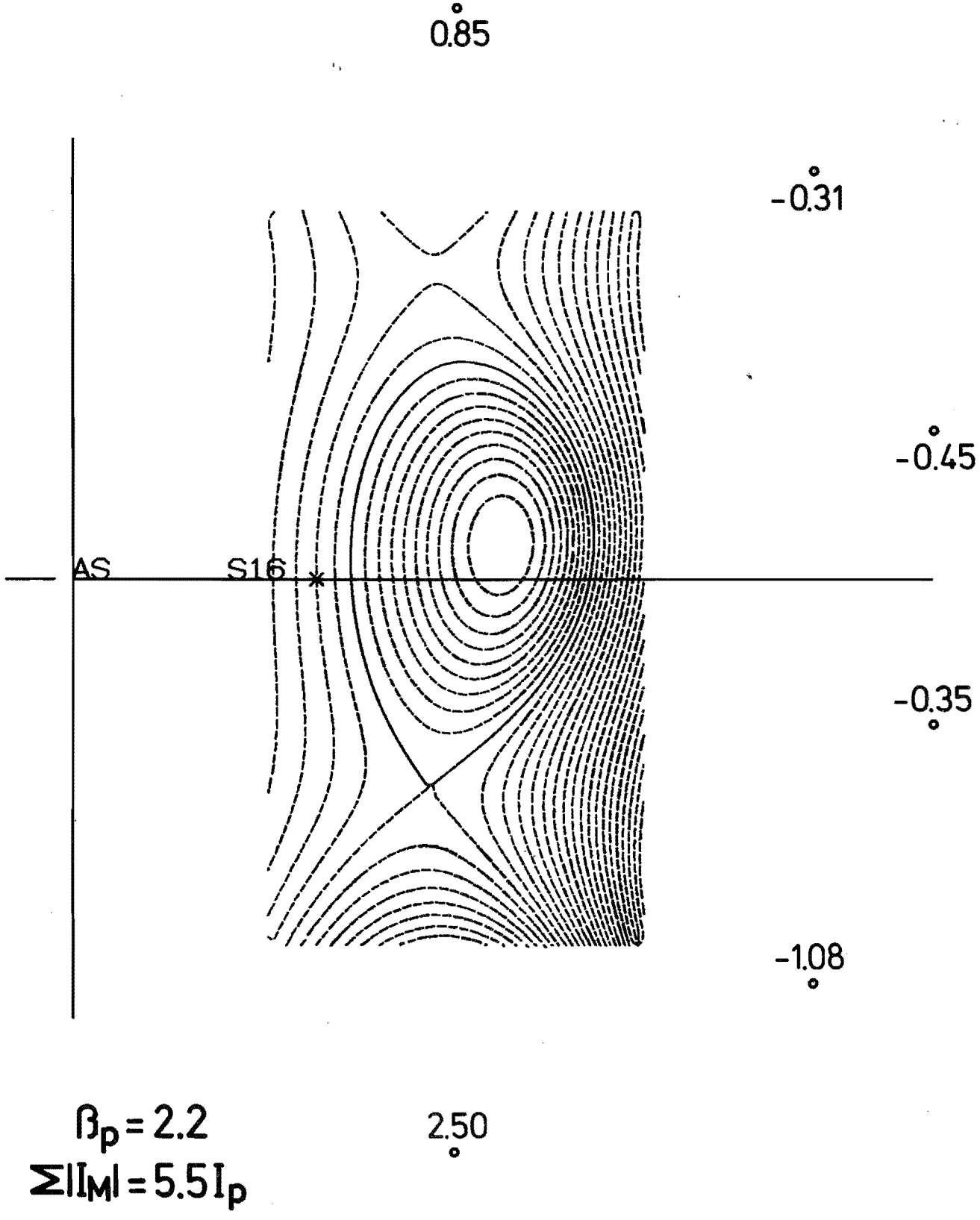

Fig. 3.2.3 Single Null Configuration for ASDEX Upgrade. The multipol currents given correspond to I_p = 1 MA.

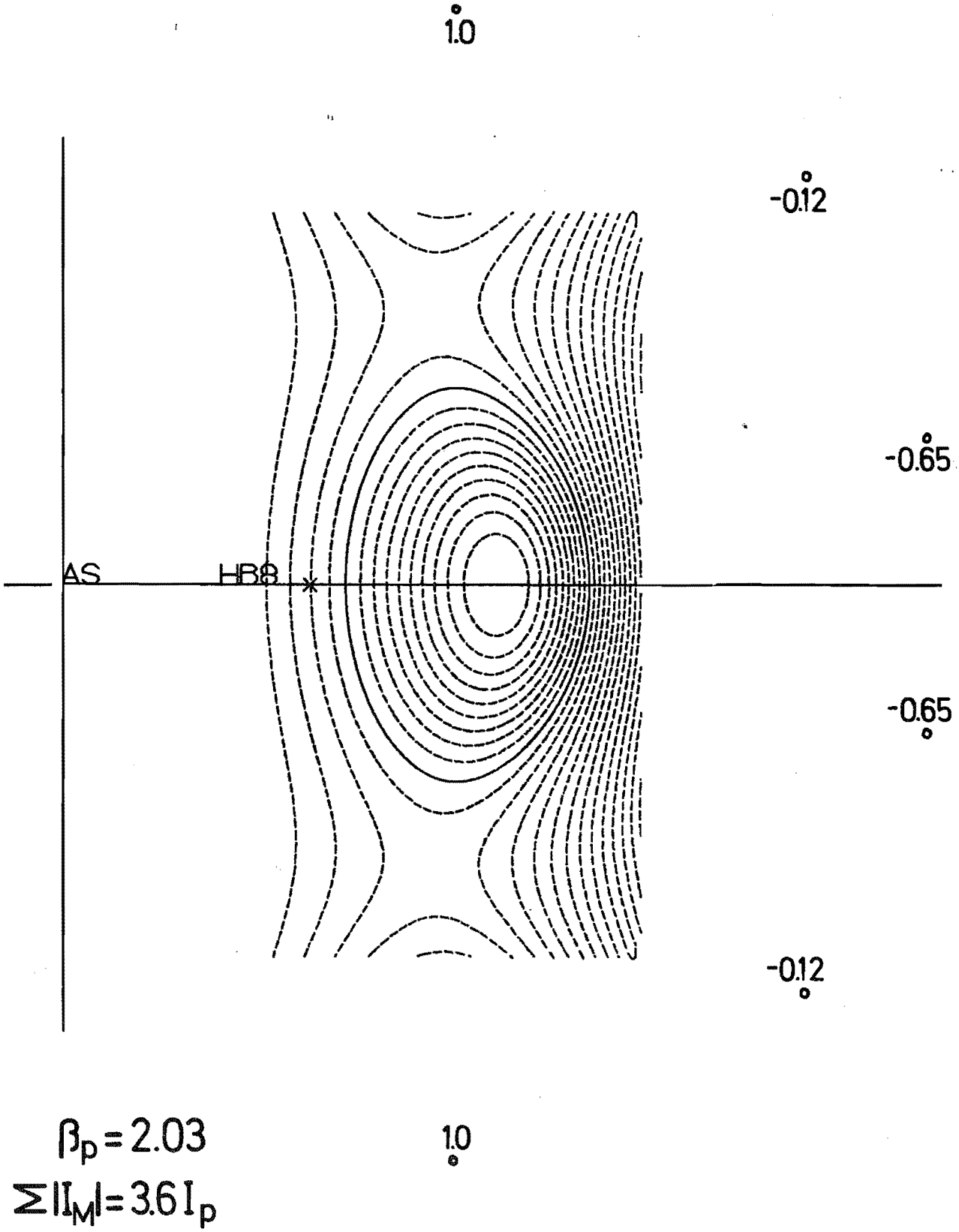

Fig. 3.2.4 Limiter Configuration for ASDEX Upgrade. The multipol currents given correspond to I_p = 1 MA.

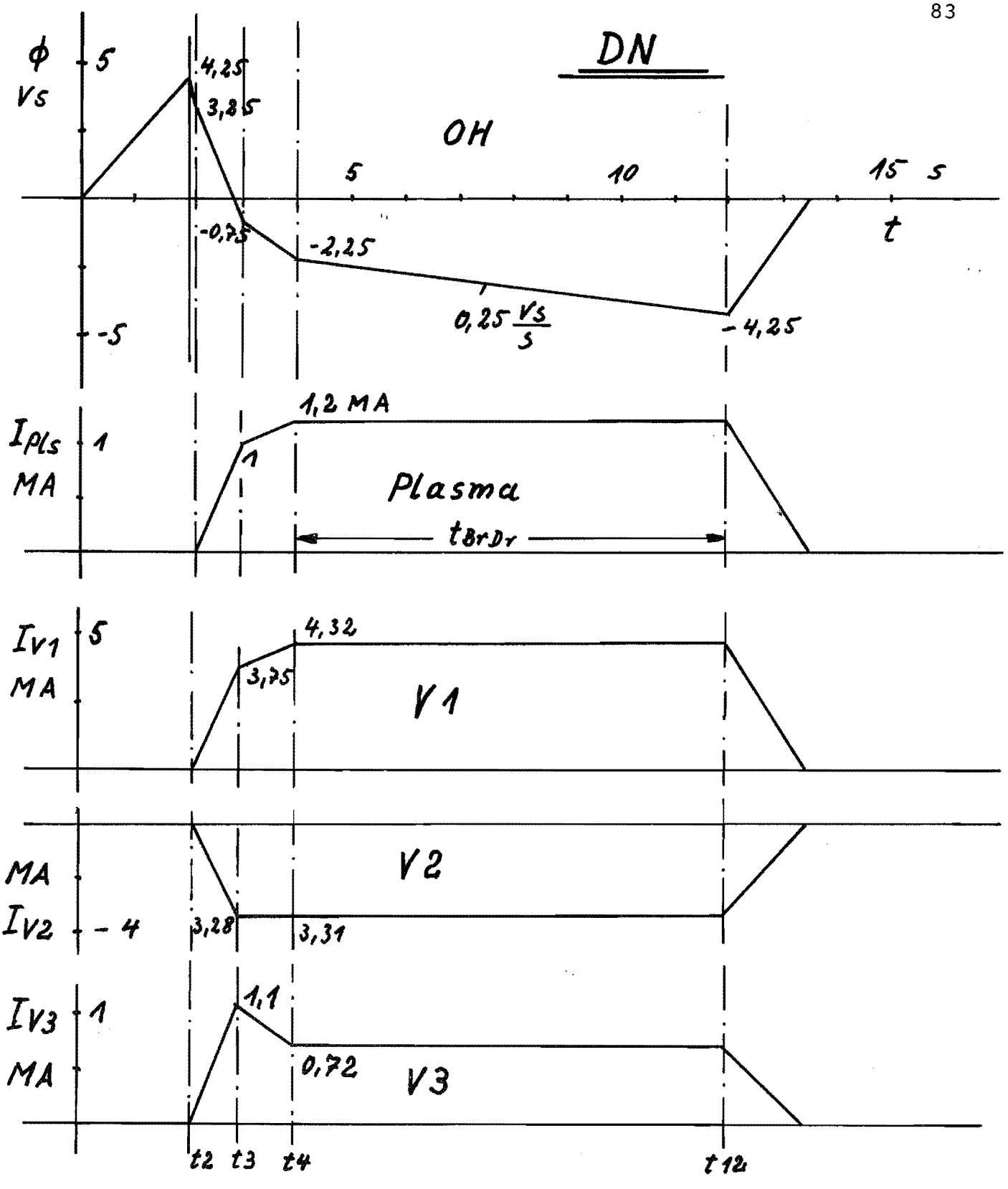

Magnetic Flux and Current Characteristics

- symmetric operation of the coils (DN) -

-V Coil Currents

disregarding TF-magnet supply requirements

Fig. 3.2.5

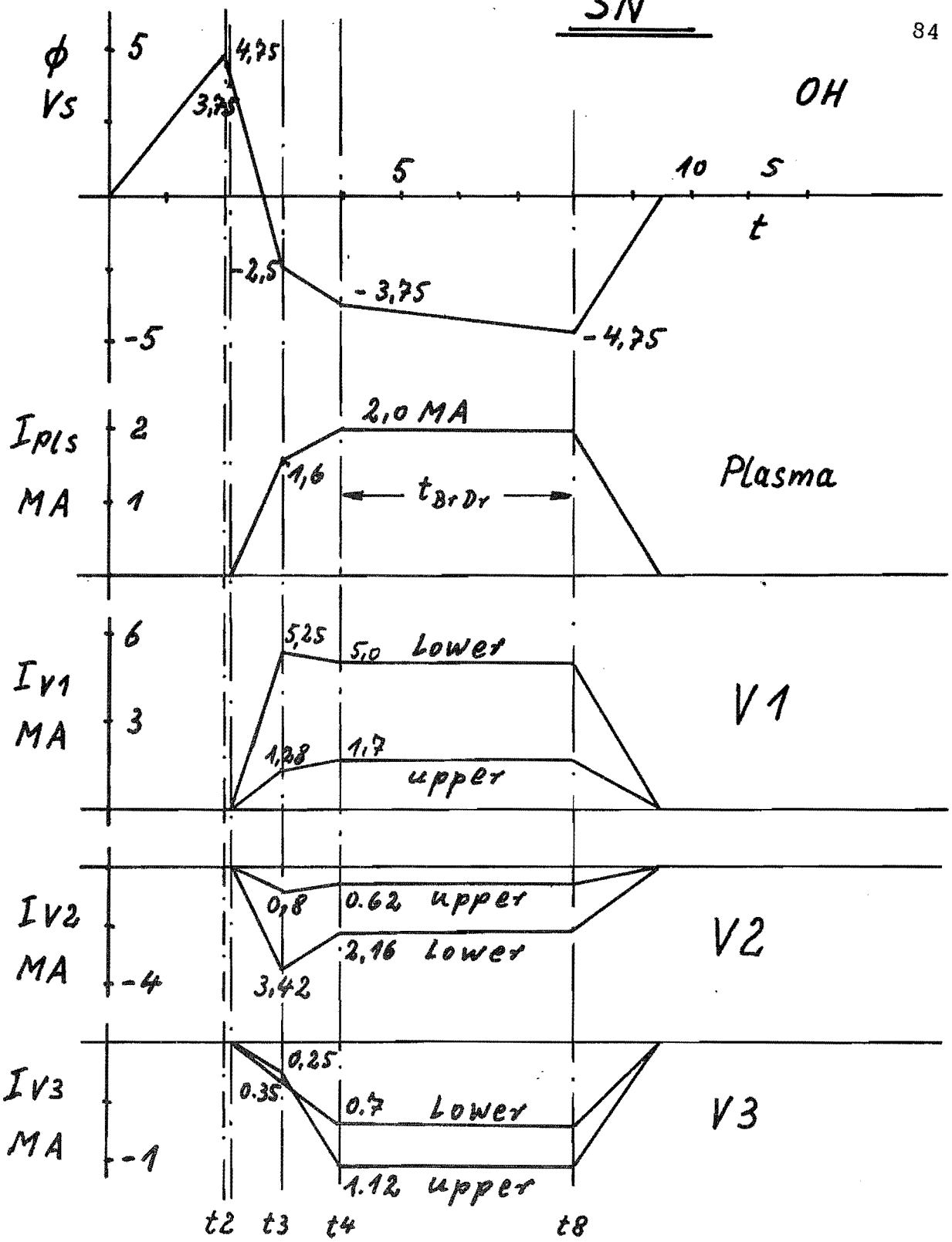

Magnetic Flux and Current Characteristics

- unsymmetric operation of the coils (SN)-
- V Coil Currents

2 MA were chosen in order to provide for 1.8 MA with 10% safety margin. I_p = 1.8 MA is conceivable for $q \geqslant 2$ operation and $I_p \cdot B_o \leqslant 4.5$ MA.

Fig. 3.2.6

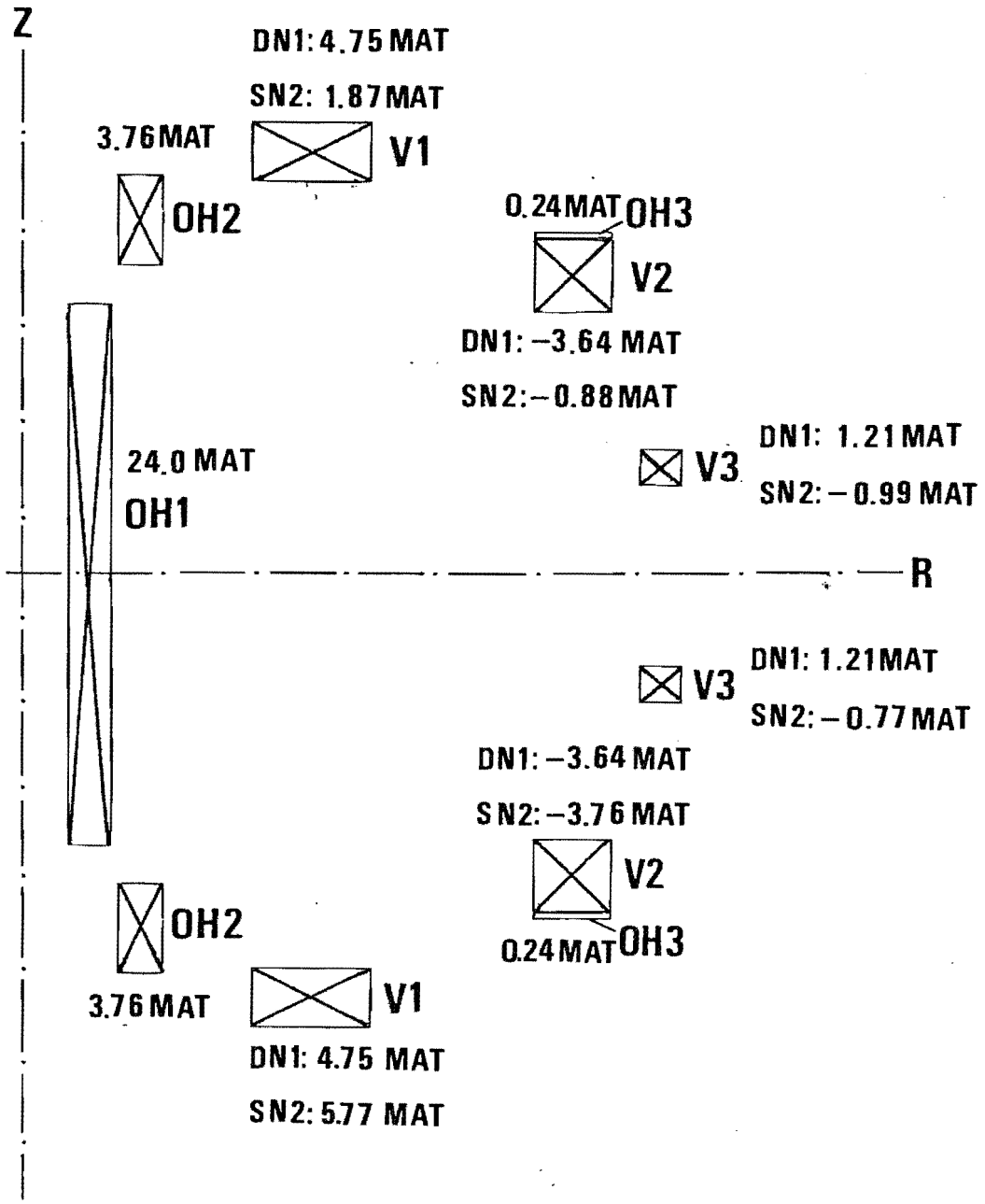

Maximum Currents in the Poloidal Field Coils

symmetric operation DN
unsymmetric operation SN

Fig. 3.2.7

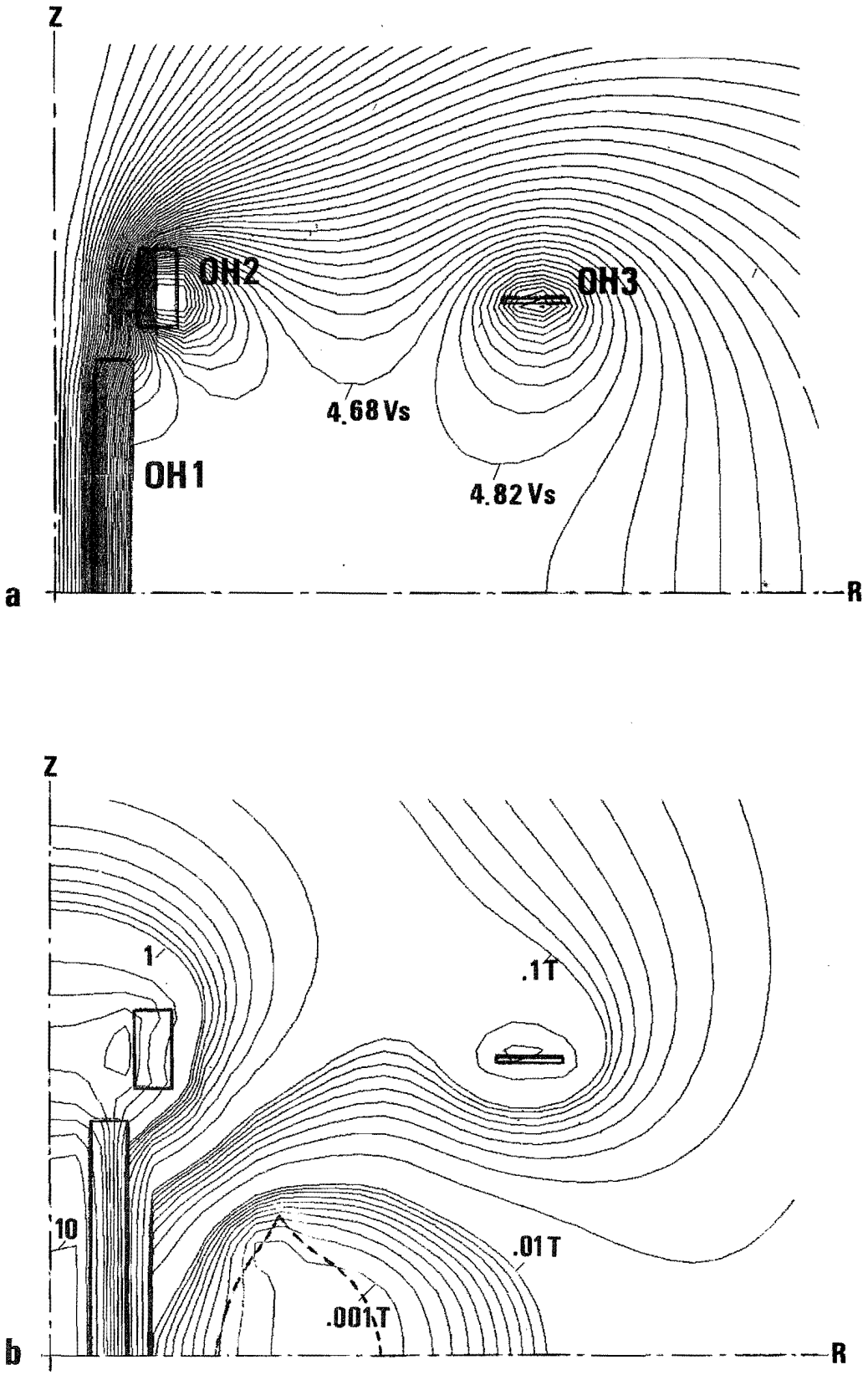

Fig. 3.2.8 OH Field Distribution

a) Contour Lines of constant Magnetic Flux

b) Contour Lines of constant Flux Density

```
: OH CIRCUIT
LOH,10-11=6C.9E-3
RLOH,11-10=C.6C
INIT,ILOH=47K
: PLASMA
LPL,20-21=1.50E-6
MOPL,LOH-LPL=6.77E-5
: VACUUM VESSEL
RG1,30-31=0.49E-3
RG2,30-32=1.20E-3
RG3,30-33=1.76E-3
RG4,30-34=1.76E-3
RGO,30-35=0.
LG1,31-35=9.02E-7
LG2,32-35=4.04E-6
LG3,33-35=3.65E-6
LG4,34-35=3.65E-6
MG12,LG1-LG2=5.77E-7
MG13,LG1-LG3=5.21E-7
MG14,LG1-LG4=5.21E-7
MG23,LG2-LG3=1.50E-6
MG24,LG2-LG4=1.50E-6
MG34,LG3-LG4=2.36E-7
: VF CIRCUIT (OPEN)
LV1,41-40=6.14E-2
LV2,43-42=6.14E-2
LV3,45-44=5.77E-2
LV4,47-46=5.77E-2
LV5,49-48=1.48E-2
LV6,51-50=1.48E-2
RV1,40-61=14.7E-3
RV2,42-63=14.7E-3
RV3,44-65=13.5E-3
RV4,46-67=13.5E-3
RV5,48-69=10.2E-3
RV6,50-71=10.2E-3
MV12,LV1-LV2=1.32E-3
MV13,LV1-LV3=1.48E-2
MV14,LV1-LV4=2.88E-3
MV15,LV1-LV5=3.74E-3
MV16,LV1-LV6=2.22E-3
MV23,LV2-LV3=2.88E-3
MV24,LV2-LV4=1.48E-2
MV25,LV2-LV5=2.22E-3
MV26,LV2-LV6=3.74E-3
MV34,LV3-LV4=6.81E-3
MV35,LV3-LV5=1.06E-2
MV36,LV3-LV6=5.54E-3
MV45,LV4-LV5=5.54E-3
MV46,LV4-LV6=1.06E-2
MV56,LV5-LV6=4.92E-3
: MUTAL INDUCTANCES
: PLASMA-> VESSEL
MPG1,LG1-LPL=5.07E-7
MPG2,LG2-LPL=1.68E-6
MPG3,LG3-LPL=6.95E-7
MPG4,LG4-LPL=6.95E-7
```

```
: MUTAL INDUCTANCES
: VESSEL -> OH
MOG1,LG1-LOH=1.00E-4
MOG2,LG2-LOH=1.00E-4
MOG3,LG3-LOH=1.01E-4
MOG4,LG4-LOH=1.01E-4
: MUTAL INDUCTANCES
: OH CIRCUIT -> VF
MOV1,LOH-LV1=9.32E-3
MOV2,LOH-LV2=9.32E-3
MOV3,LOH-LV3=8.49E-3
MOV4,LOH-LV4=8.49E-3
MOV5,LOH-LV5=2.93E-3
MOV6,LOH-LV6=2.93E-3
: VF CIRCUIT -> PLASMA
MPV1,LPL-LV1=3.69E-5
MPV2,LPL-LV2=3.69E-5
MPV3,LPL-LV3=6.09E-5
MPV4,LPL-LV4=6.09E-5
MPV5,LPL-LV5=3.40E-5
MPV6,LPL-LV6=3.40E-5
: MUTAL INDUCTANCES
: VF CIRCUIT -> VESSEL
MVG11,LV1-LG1=2.44E-5
MVG12,LV1-LG2=8.71E-5
MVG13,LV1-LG3=1.53E-4
MVG14,LV1-LG4=1.84E-5
MVG21,LV2-LG1=2.44E-5
MVG22,LV2-LG2=8.71E-5
MVG23,LV2-LG3=1.84E-5
MVG24,LV2-LG4=1.53E-4
MVG31,LV3-LG1=2.57E-5
MVG32,LV3-LG2=1.54E-4
MVG33,LV3-LG3=1.35E-4
MVG34,LV3-LG4=3.83E-5
MVG41,LV4-LG1=2.57E-5
MVG42,LV4-LG2=1.55E-4
MVG43,LV4-LG3=3.82E-5
MVG44,LV4-LG4=1.35E-4
MVG51,LV5-LG1=1.25E-5
MVG52,LV5-LG2=8.17E-5
MVG53,LV5-LG3=4.30E-5
MVG54,LV5-LG4=2.80E-5
MVG61,LV6-LG1=1.25E-5
MVG62,LV6-LG2=8.17E-5
MVG63,LV6-LG3=2.80E-5
MVG64,LV6-LG4=4.30E-4
```

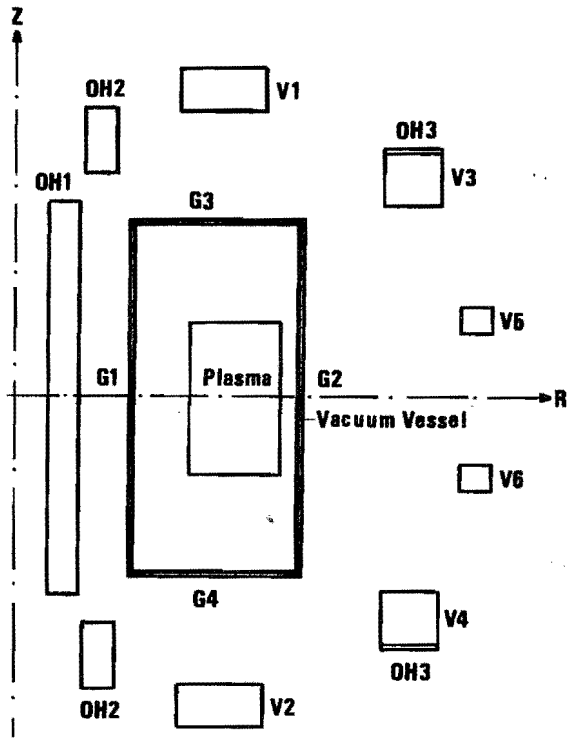

Fig. 3.2.9

Poloidal Field Network Simulation

ECAP Input List
Coil Arrangement
Network

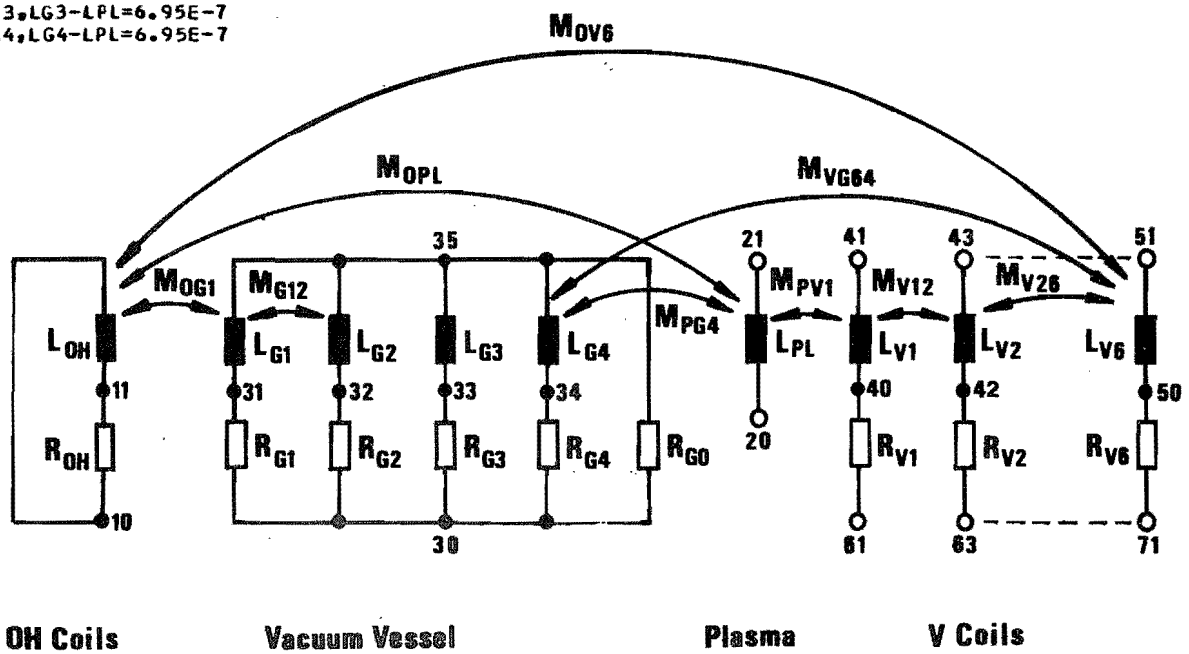

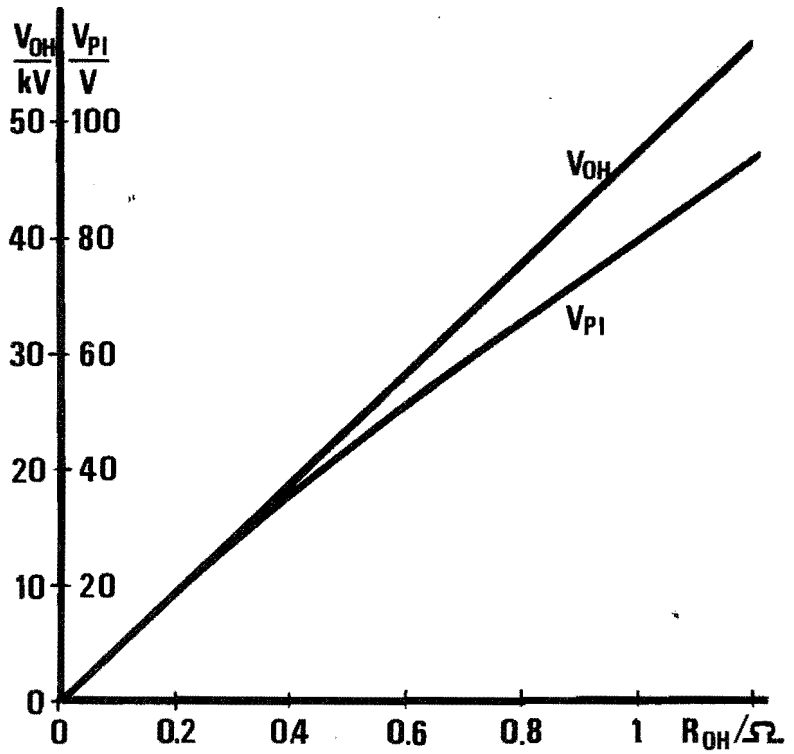

Fig. 3.2.10 OH Coil Voltage V_{QH} and Induced Plasma Loop Voltage V_{Pl} vs. Discharge Resistance

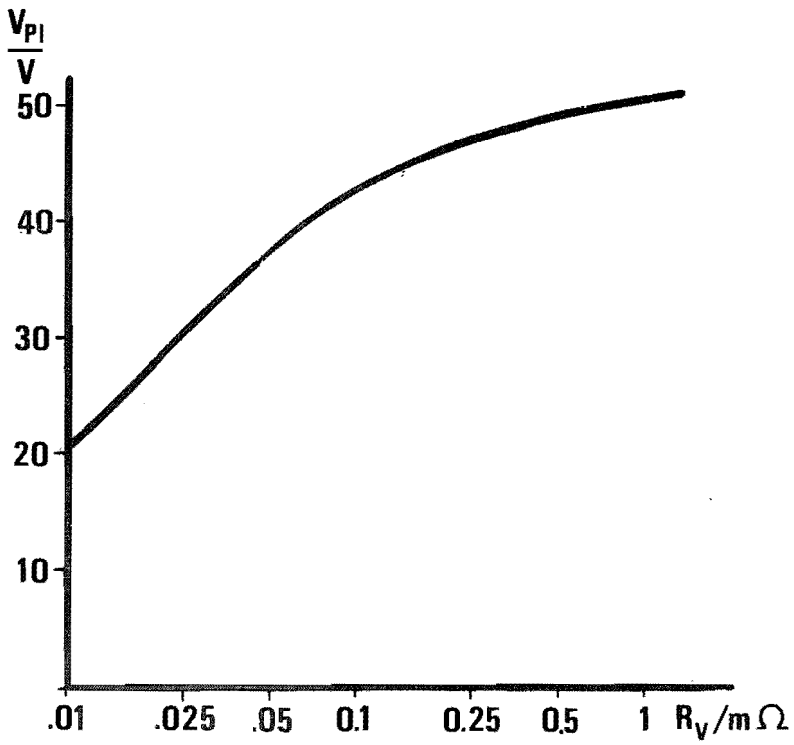

Fig. 3.2.10 a Induced Plasma Loop Voltage V_{Pl} vs. Resistance of the Vacuum vessel R_V

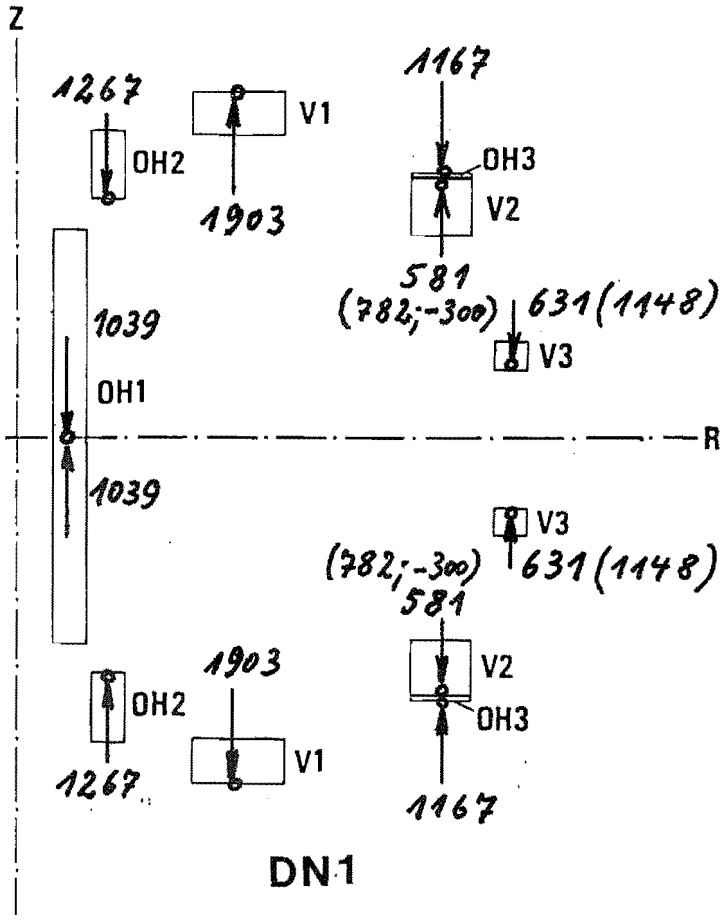

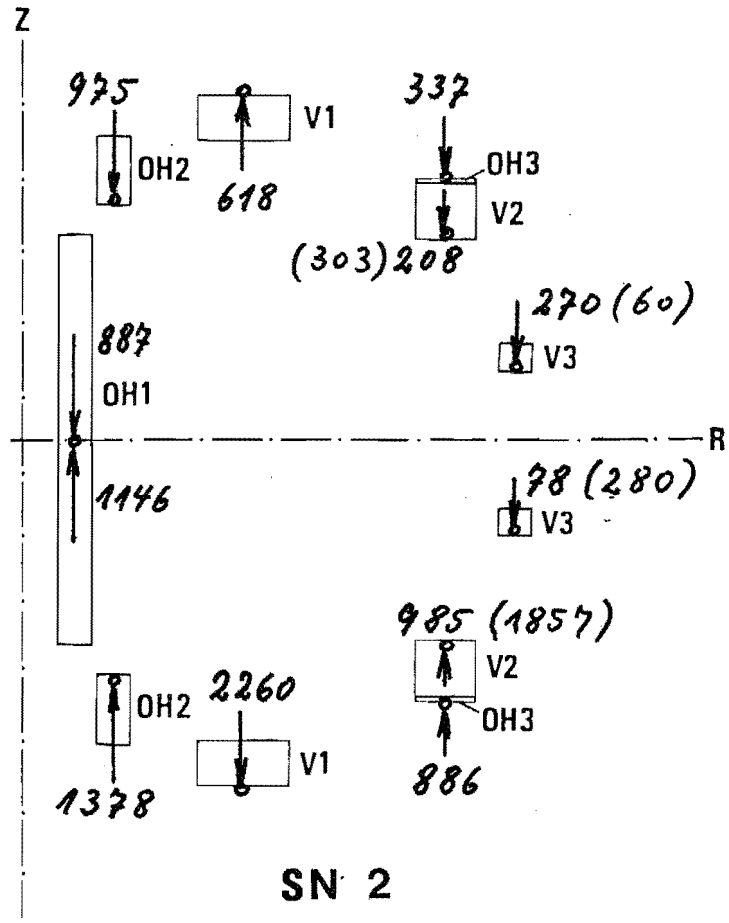

Integral vertical I x B Forces of the PF Coils

Maximum load of the support structure (load case 4)

(in brakes) maximum values of the coils induced at different loads

Fig. 3.2.11

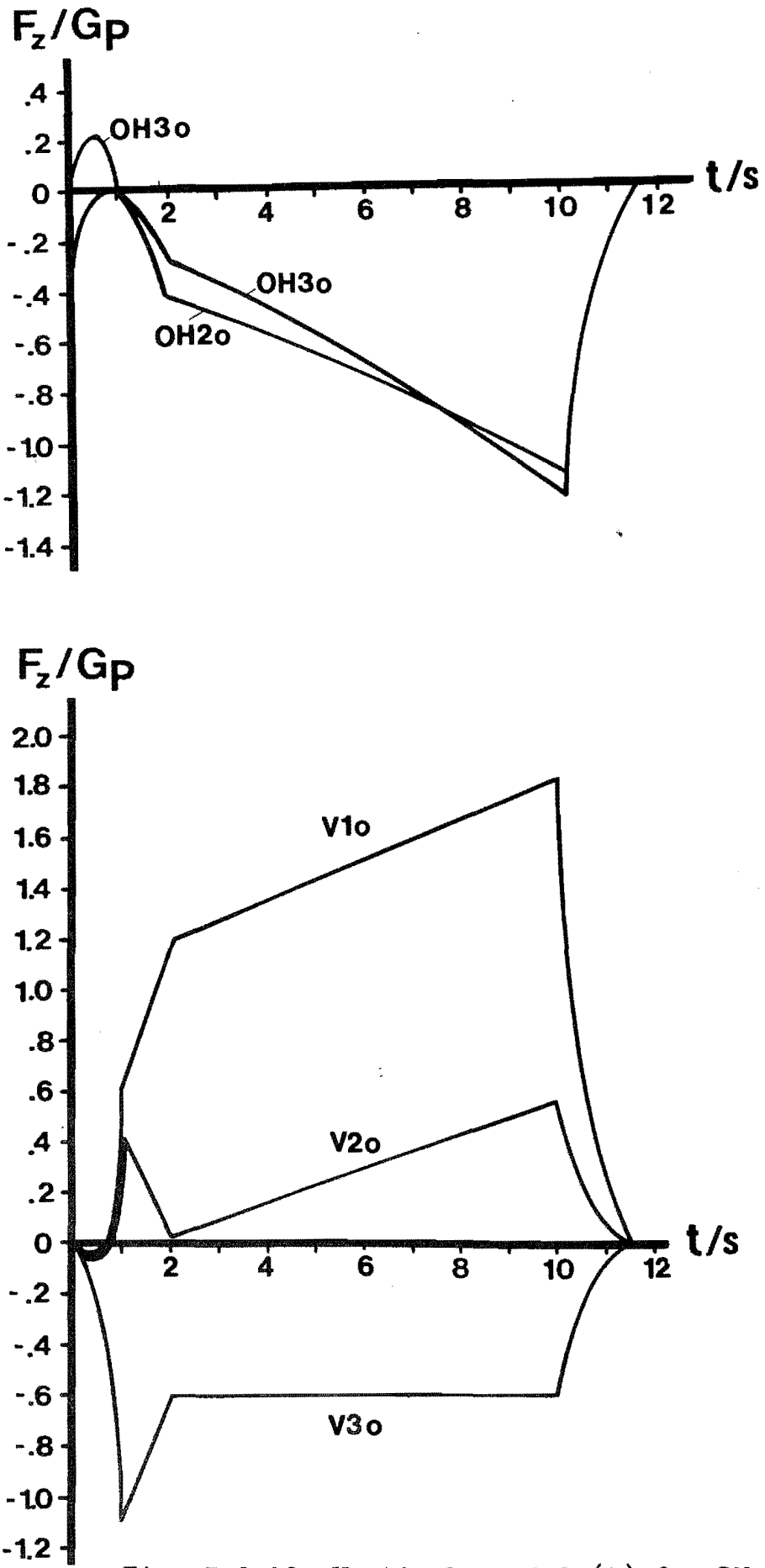

Fig. 3.2.12 Vertical Load $F_z(t)$ for DN Operation without Plasma

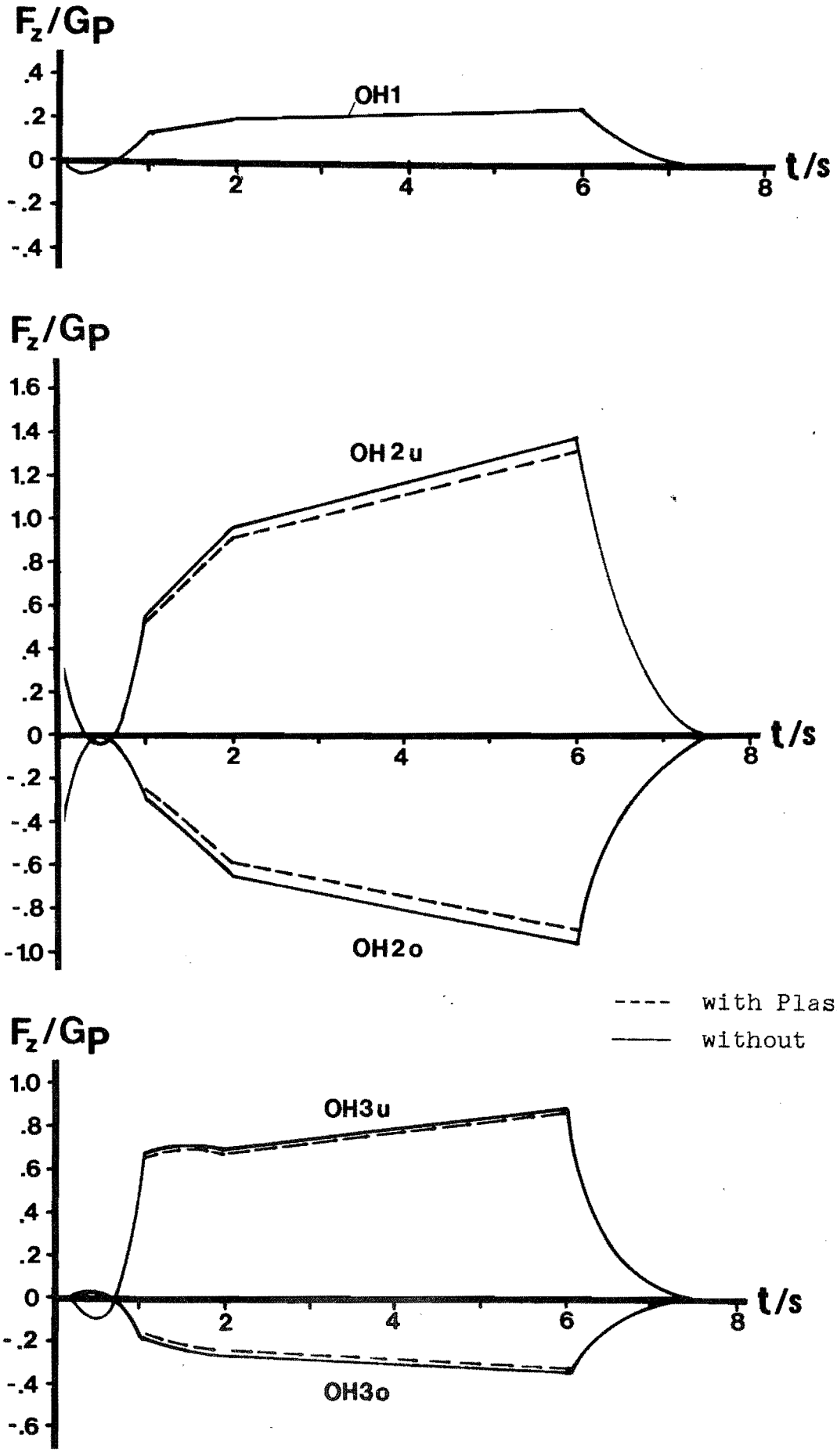

Fig 3.2.13 Vertical Load $F_z(t)$ for SN Operation
OH Field Coils

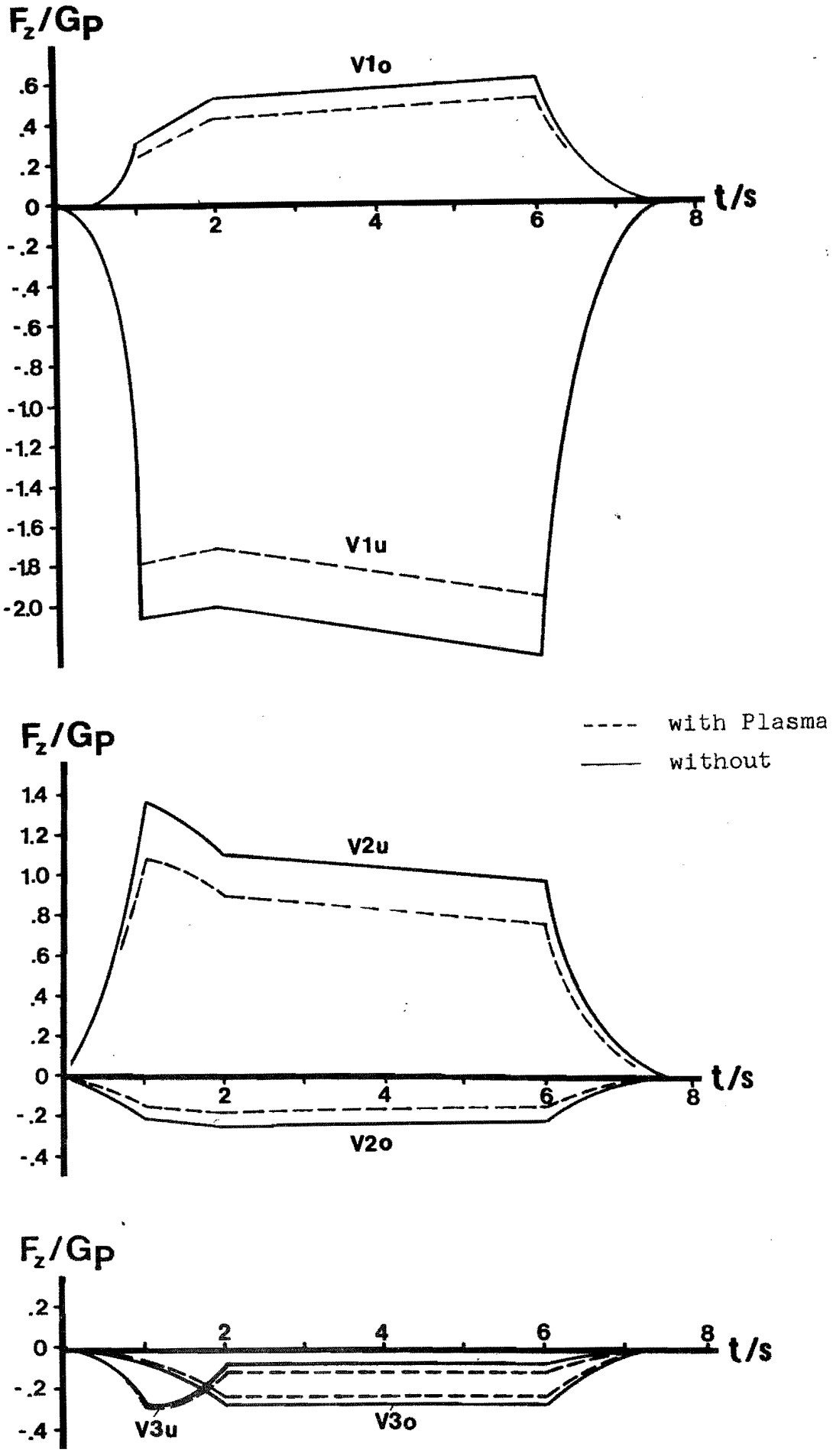

Fig. 3.2.14 Vertical Load $F_z(t)$ for SN Operation
Vertical Field Coils

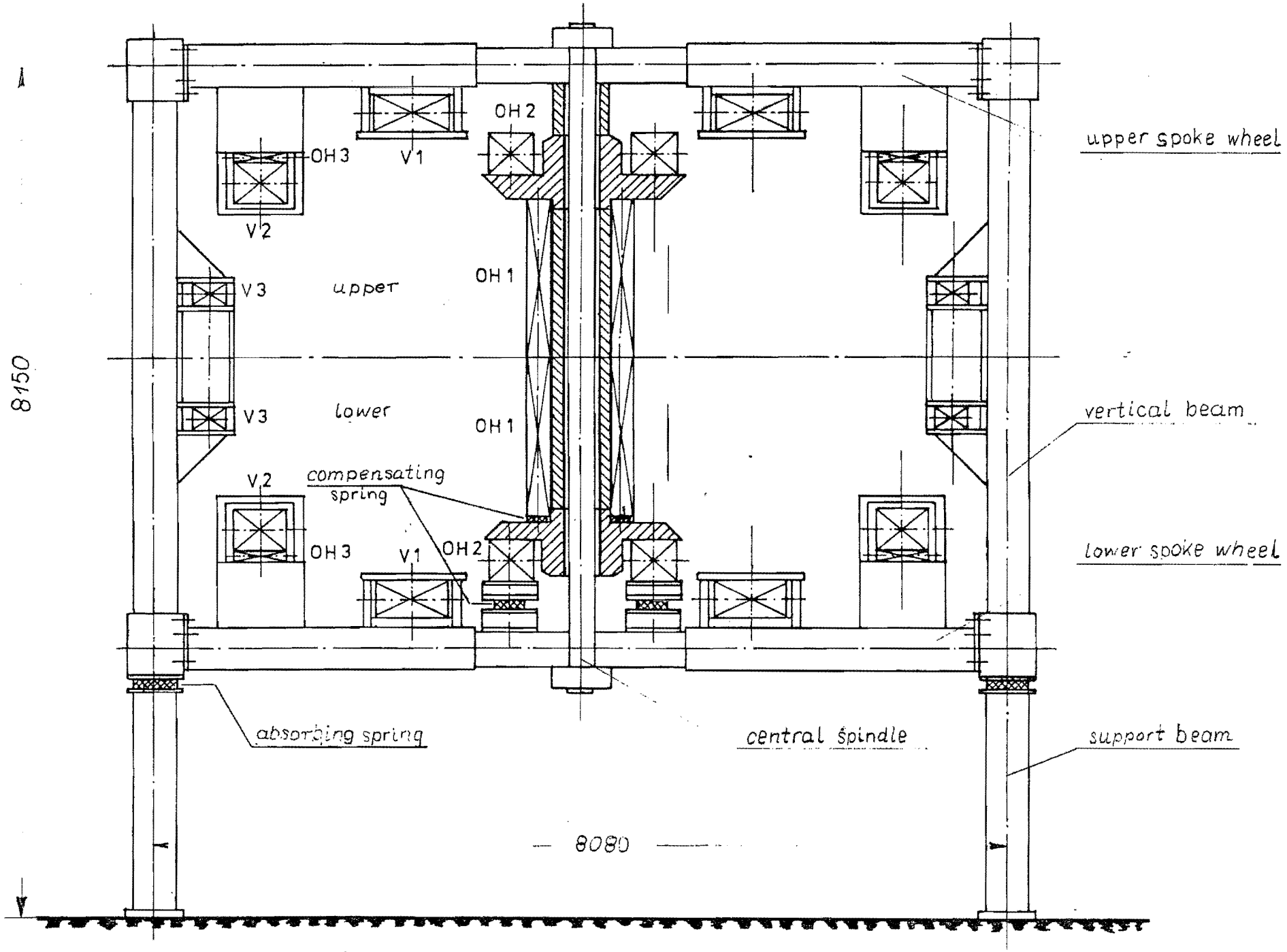

Fig. 3.2.15: Poloidal Field Support Structure

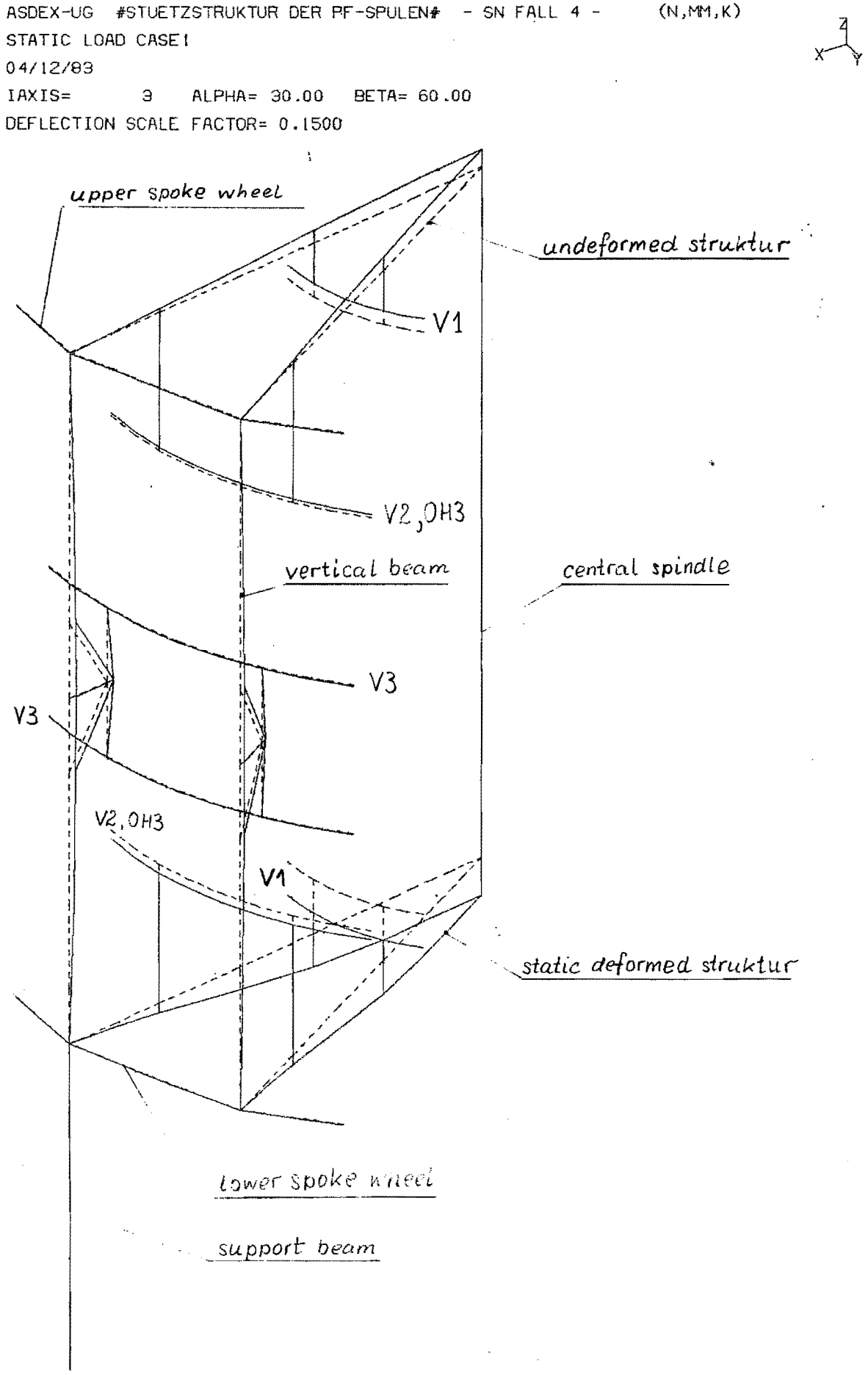

Fig. 3.2.16 Finite Element Modell

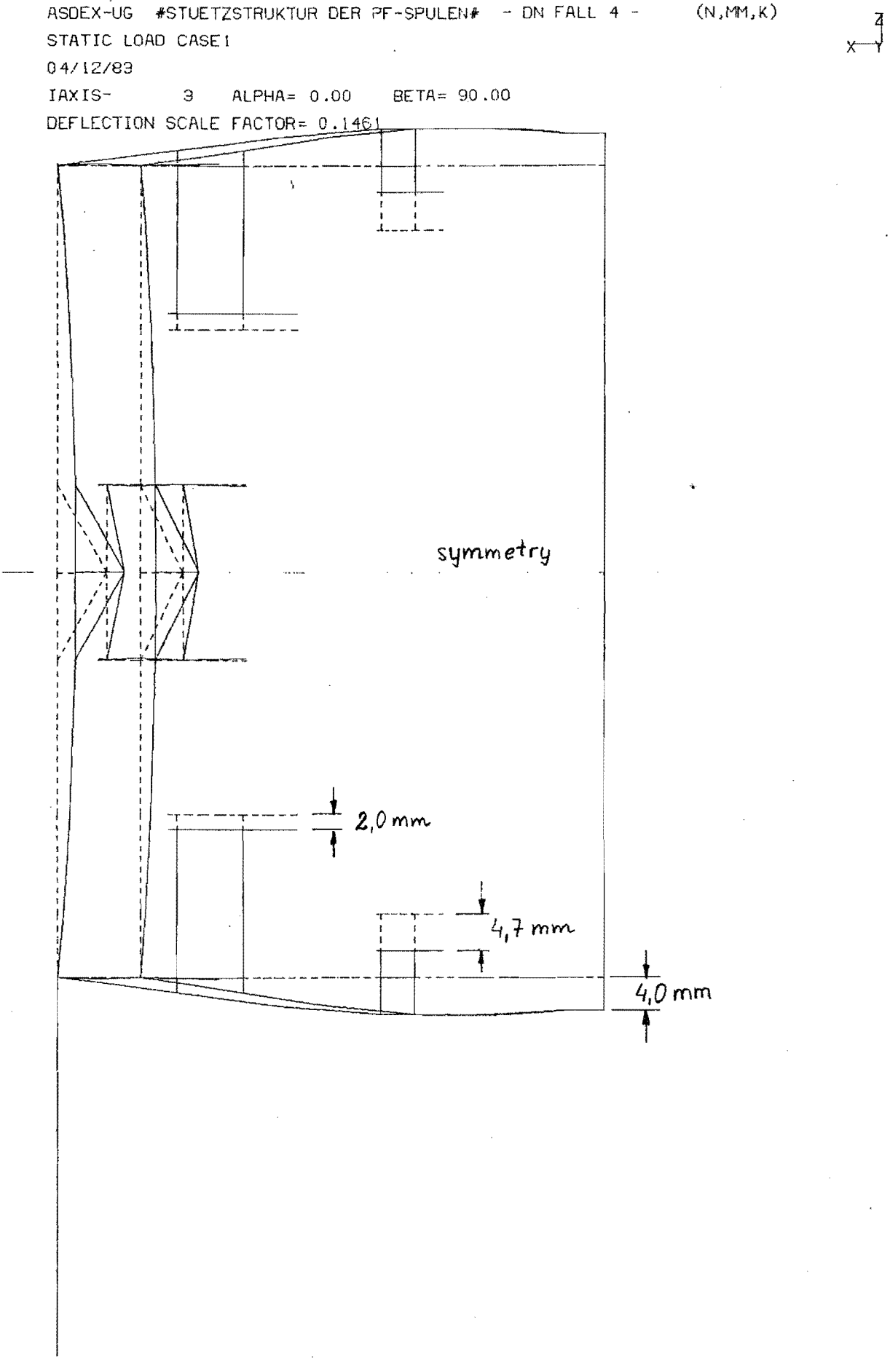

Fig. 3.2.17: Deformation of the framework under DN load

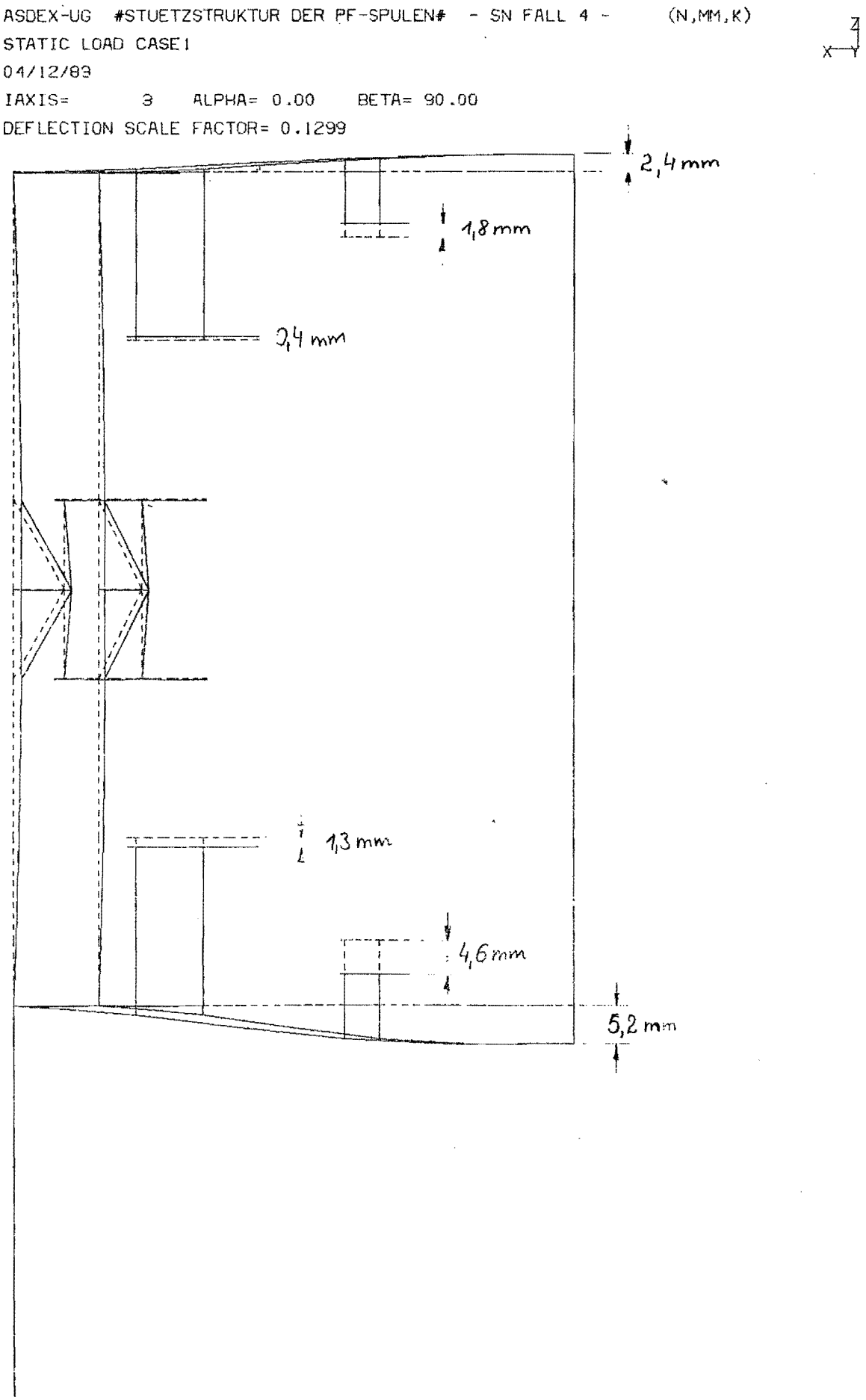

Fig. 3.2.18: Deformation of the framework under SN load

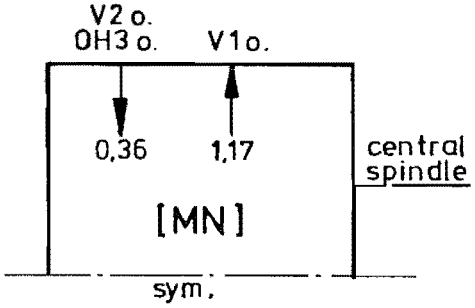

a) vertical component of the Lorentzforces

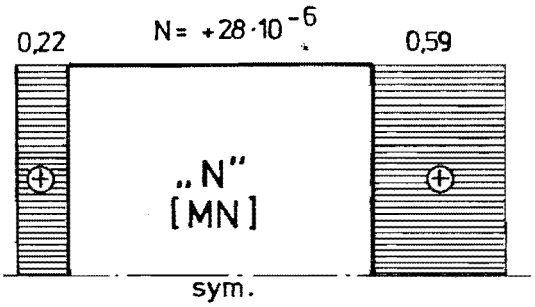

b) normal force distribution

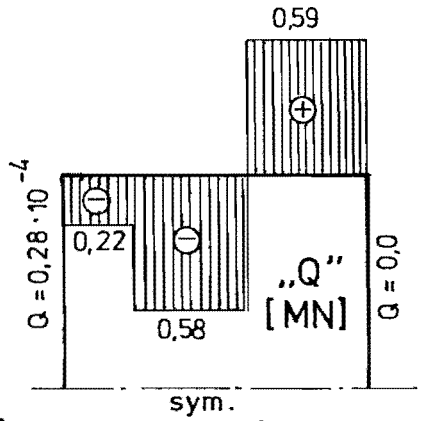

c) transverse force distribution

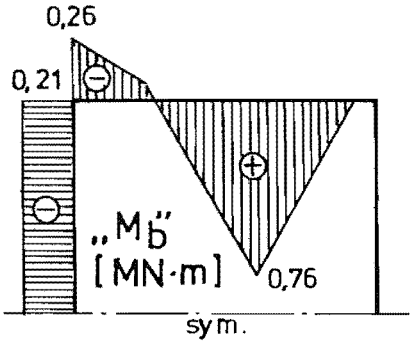

d) bending moment distribution

Fig. 3.2.19: Internal forces distribution under DN load

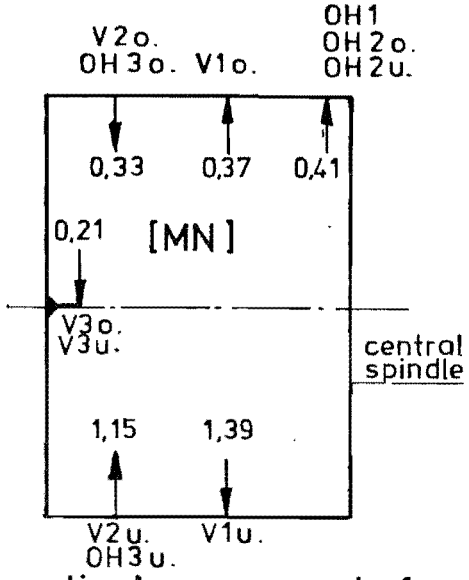

a) vertical component of the Lorentzforces

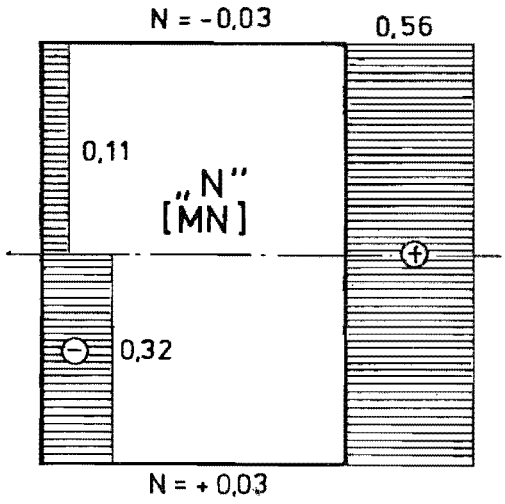

b) normal force distribution

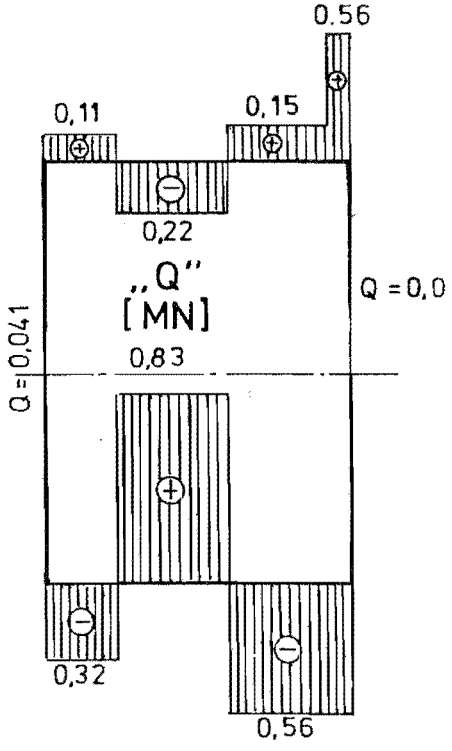

c) tranverse force distribution

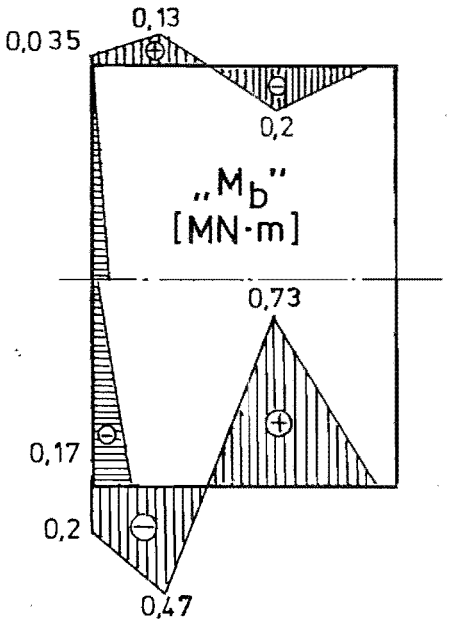

d) bending moment distribution

Fig. 3.2.20: Internal forces distribution under SN load

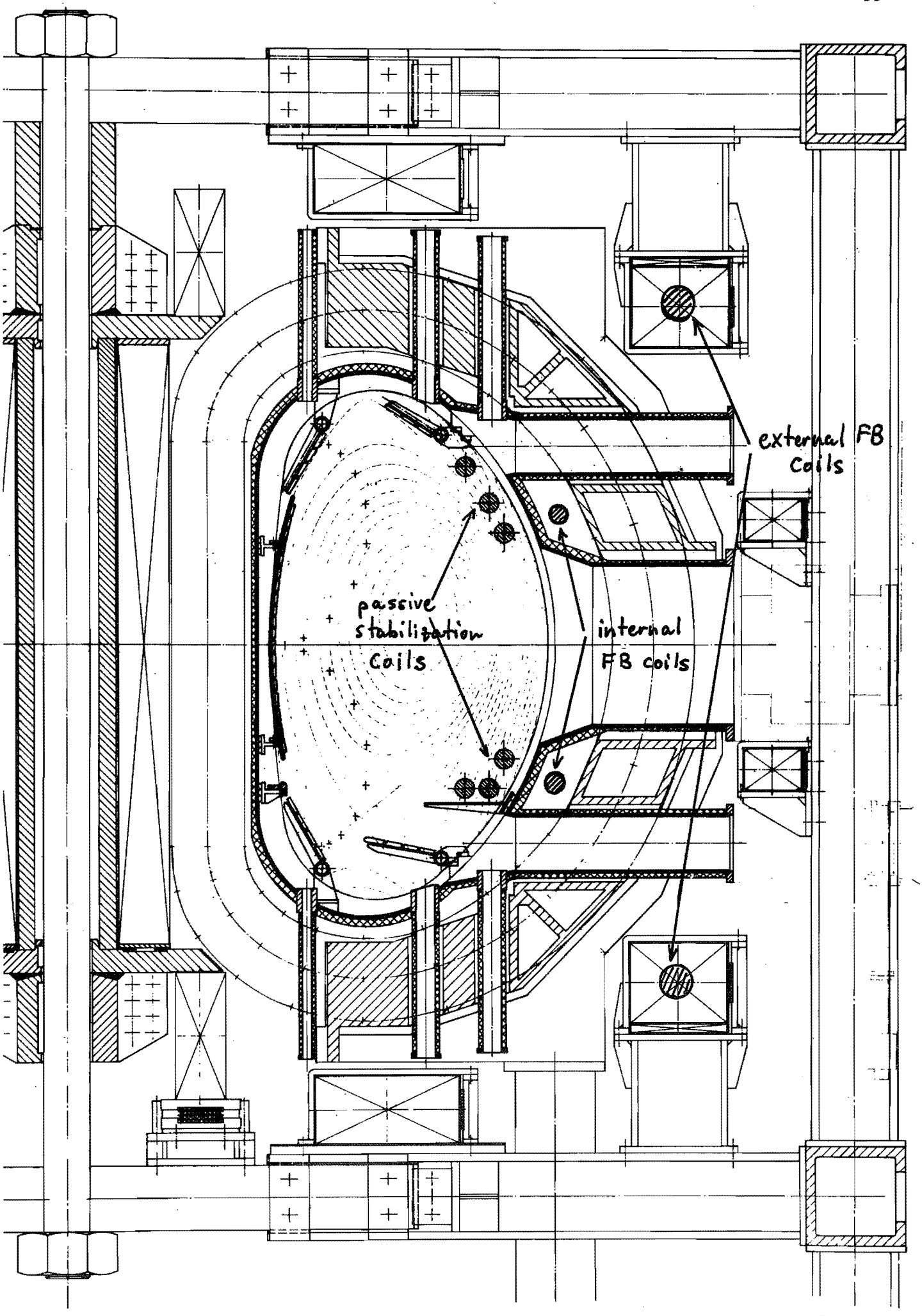

Fig. 3.2.21: Position of the passive stabilization coils and of the internal and external feedback coils.

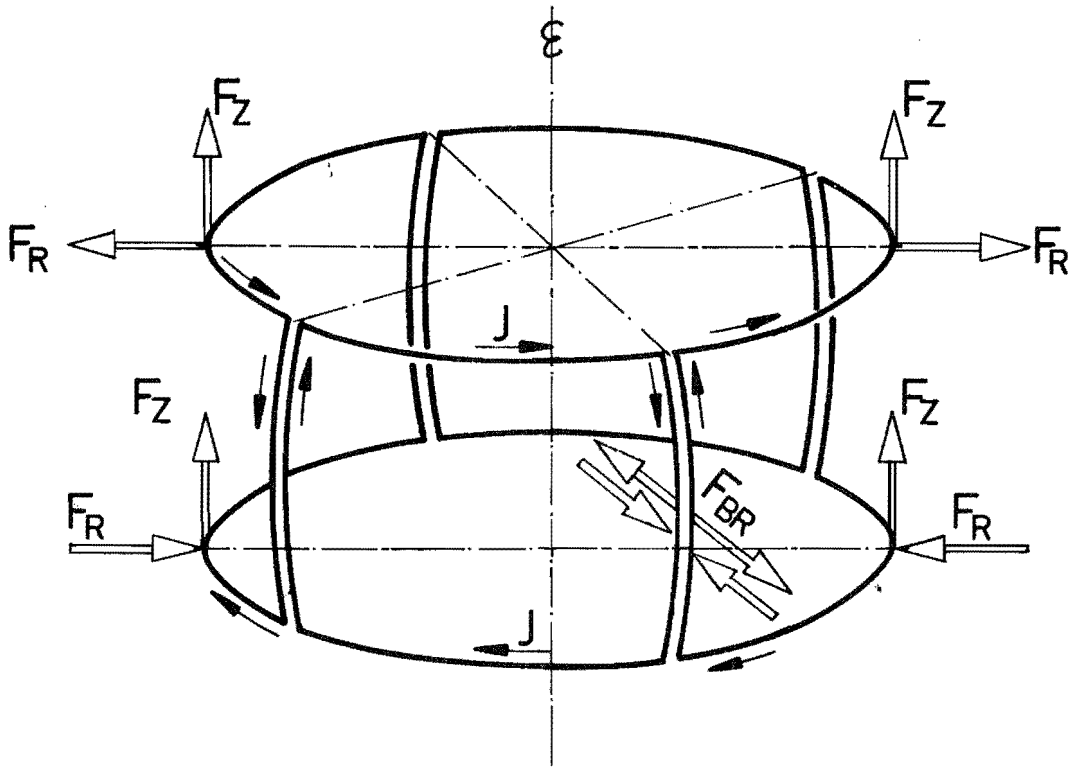

for $J_p = 2\,MA$ $\quad F_Z \approx 2{,}5 \frac{t}{m}$ $\quad F_{Z\,tot} \approx 60\,t$

$F_R \approx 4 \frac{t}{m}$ $\quad (F_R$ and F_Z proportional to $J_p^2)$

for $J_p \cdot B_T = 6{,}5\,MAT$

$F_{BR} \approx 23 \frac{t}{m}$ $\quad$ (proportional to $J_p \cdot B_T$)

FIG 3.2.22

FORCE LOAD ON THE STABILIZATION LOOPS

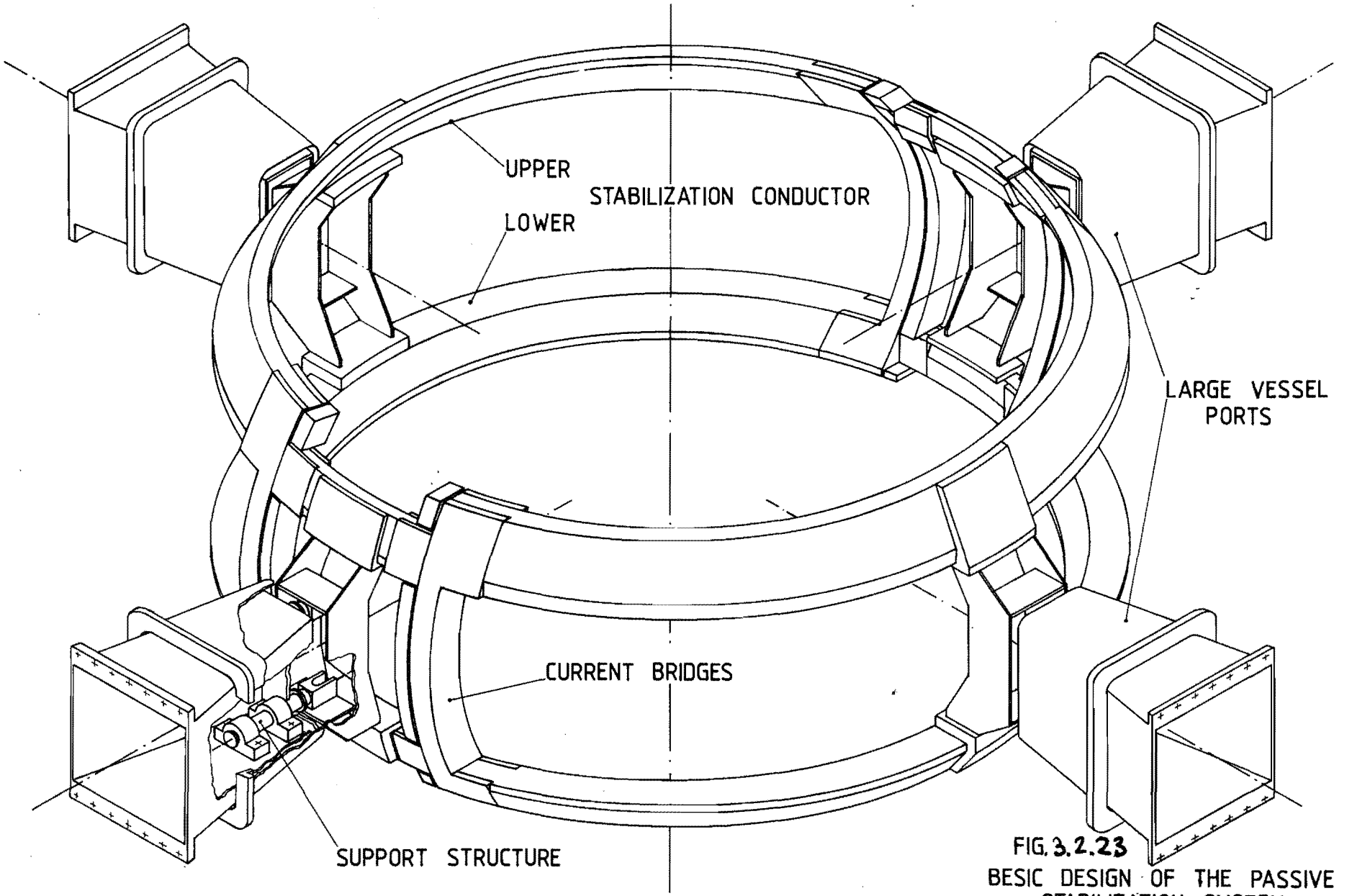

FIG. 3.2.23
BESIC DESIGN OF THE PASSIVE STABILIZATION SYSTEM

3.3 The Vacuum Vessel System

3.3.1 The Vessel Concept

The vacuum vessel concept of ASDEX UG is a further development of that successfully used in ASDEX. Maintaining the good access to the plasma, little space required for the wall structure and good attachment possibilities for divertor plates and diagnostic elements the vessel is adapted to higher thermal and electromagnetic loads and the modular assembly of the ASDEX UG. The specific features of the vessel are:

- self-supporting toroidal shell composed of 16 wedge-shaped segments of a D-shaped cross-section and 15 mm wall thickness (Fig. 3.3.1);

- the corners of the 16 polygon are placed in the symmetry planes of the TF coils and are reinforced by ribs and flanges along the poloidal circumference of the vessel (Fig. 3.3.2);

- four segments form a 90^{o} vessel module;

- the vessel modules, pre-assembled with the corresponding TF coils and magnet structure have to be bolted together from inside the vessel to form the torus;

- the vacuum tightness at these joints is given by a copper-coated Helicoflex-O-ring backed by a Viton-O-ring. In the space between these O-rings a separate vacuum of approximately 0.1 mbar can be established for testing purposes during assembly and for reduction of possible leaks during operation;

- each of the four vessel modules incorporates an electrical break. In order to satisfy the vacuum requirements these breaks are covered by metallic bellows which reduce the toroidal electrical resistance of the vessel to 0.25 m Ω (Fig. 3.3.3);

- the vessel is supported by the magnet via eight tension bars which enable free, concentric expansion during baking up to 150 C;

- expansion elements between the tension bars and the magnet provide a constant height of the vessel midplane, indepedent of the vessel temperature;

- the vessel wall, divertor plates, heat shield and diagnostic elements can be actively cooled by water;

- attachment of elements inside the vessel will be done using a stud welding technique developed especially for vacuum application.

The access to the interior of the vessel is given by following ports:

- 8 horizontal ports of a rectangular cross-section, 40 cm wide and 80 cm high for assembly purposes, diagnostics, pumping and stabilization loops;

- 30 horizontal ports of 28 cm diameter for divertor pumping;

- 2 inclined ports of 20 cm diamter for neutral beam diagnostic;

- 16 horizontal ports of 23 cm diamter for ICR heating;

- 28 vertical ports of 10 cm diamter for laser diagnostics and observation of the ICRH antennas;

- 8 vertical ports of 5 cm diamter for laser diagnostics.

3.3.2 Parameters of the Vessel

Outer diameter in horizontal direction:	5.2 m
inner diameter in horizontal direction:	1.85 m
diameter in vertical direction:	2.85 m
maximum wall thickness on R :	8 cm
total weight:	24 t
volume:	32 m^3
internal wall area of the equivalent torus with smooth surface:	72 m^2
internal wall area taking into account the convolutions of the bellows:	84 m^2
internal wall area including the heat shield, divertor plates and ports:	270 m^2
electrical resistance in toroidal direction:	0.25 $m\Omega$
electrical resistance in poloidal direction:	0.025 $m\Omega$
maximum baking temperature:	150 C
vessel and bellows material:	SS 304 LN
thermal insulation of the vessel	20-40 mm silicon rubber

3.3.3 Stress Calculations

The largest mechanical stress on the vessel occurs in the separation plans, in particular in the assembly joints, electrical breaks and bellows. The stress calculations have therefore been concentrated on these parts of the vessel, primarily to ensure the tightness of the torus and to minimize the elastic deformations at the ports.

Atmospheric pressure load: The atmospheric pressure of 1 bar acting on the vessel surface generates in the wall hoop forces which vary along the poloidal circumference from 108 N/mm tension to 180 N/mm compression with a mean value of 48 N/mm compression. Responsible for this variation are the aspect ratio of the torus, the low wall thickness and the straight inner part of the vessel, acting as a cylinder under internal pressure (Fig. 3.3.4). The compression has to be transmitted by the large contact area of the flanges, the tension by threaded bolts of 20 mm diamter spaced equidistant along the poloidal circumference of the vessel. At the assembly joint a constant compression of 200 N/mm is required to ensure the vacuum tightness of the Helicoflex- and Viton-O-rings. Together these forces result in a tension at the bolts of 25 kN which have to be compensated by an adequate pre-tension. By use of a cold worked stainless steel with a yield strength of 270 MPa a pre-tension of 50 kN can be achieved - 50 % more than the actual tension at the assembly joint.

The bolts at the electrical breaks are exposed only to tension caused by atmospheric pressure and provide therefore a larger safety margin.

The dimensioning of the bellows is also determined by the atmospheric pressure. As shown in Fig. 3.3.5, the maximum stress and deflection of the bellows depend very much on their major curvature and reach maximum values for a plane corrugated sheet (infinite curvature radius).

In ASDEX UG the bellows at the cylindrical part of the vessel could be curved maximally with a radius of 7000 mm. This allowed to reduce the bellow stress by 55 % to 150 MPa compared with a straight bellow link, a value which reaches 60 % of bellow material yield strength (Fig. 3.3.6).

The 40 MPa stresses in the vessel wall caused by the atmospheric pressure are negligibly low.

Gravity load: Also the weight of the vessel of approximately 24 t generates very low stresses in the shell. Low, but not negligible are the tension forces which, similar to those produced by the atmospheric pressure, reduce the pre-tension of the bolts (Fig. 3.3.4).

The position of the vessel supports at the large radius of 1800 mm is a compromise between the distortion of the vessel shell and ports and the access for assembly and maintenance purposes.

Thermal load: All parts of the vessel are shielded from direct plasma contact by various in-vessel components (heat shield, divertor plates, antennas etc.). The heat load on the vessel is therefore solely due to radiation from the plasma, which, on average, amounts to 0.1 MW/m^2 in the standard case and to 0.2 MW/m^2 in case of 100 % radiation from the main plasma. This requires active cooling during pulse interval for the vessel and other exposed components. The vessel will be cooled from the outside by the heating and cooling system also used for bake-out.

In the worst case (100 % radiation during a 10 s pulse with 10 MW of heating power) the temperature of the inner surface of the vessel rises by 95 K. The resulting thermal stress (tension) of $\leq$ 130 MPa, is not critical. After temperature equilibration the vessel will be 35 K above coolant temperature, which again is uncritical.

Thin in-vessel components exposed to the radiation heat up excessively and are therefore not permitted. For this reason also the bellows have to be shielded from the radiation.

Electromagnetic loads during plasma disruption: The discontinuities in the vessel resistance at the electrical breaks lead to large shear forces along the electrical breaks during a hard plasma disruption (Fig. 3.3.7).

The eddy current calculations were performed with the aid of an extended version of FEDIFF, a computer programme based on the Finite Element Network method. Extended by a post-processor and input of external magnetic fields the resulting force distribution has been used directly as input for the mechanical stress analysis with the SAP finite element code.

The force locking design of the electrical breaks of the vessel resulted from the above analysis. The toroidal distribution of the electromagnetic forces, up to 42 times the atmospheric pressure, causes bending stresses in the 15 mm thick vessel wall and twisting of the electrical break flanges (Fig. 3.3.8). By introduction of reinforcements inside the vessel the stresses in the shell have been reduced to 150 MPa and deformations to values below 1 mm.

The mechanical design of the divertor plates, separation plates and heat shield is still based on estimates of loads expected during a plasma disruption. Detailed calculations

will be done together with the final optimization of the vessel.

3.3.4 Divertor plates (DP) and Heat Shield

General description of the divertor region (Fig. 3.3.1): The plasma flowing along the field lines outside the separatrix impinges on the DP. The plates have to withstand the heat load.

Hydrogen atoms neutralized at the target plates are either reionized within the divertor plasma or escape to the outer divertor region, depending on their line of flight. On the outside this region is separated from the main plasma chamber by the separation plates, which prevents the direct recycling of the neutrals from the divertor region to the main plasma. On the inner DP no such separation is possible.

In single-null operation only the lower divertor plates are used. The upper DP's facilitate double-null operation without changing the in-vessel structure. In this case, however, there is no separate divertor chamber in the upper divertor region. All necessary connections will be provided such that symmetrical divertor structure for double-null operation can be installed with a minimum of construction time.

Thermal load, material selection: Two considerations determine material selection: Thermal load and the desire to have low -Z material.

Of the low-Z materials graphite (or TiC-coated graphite) has been successfully used in several tokamaks. It has also been chosen for ASDEX UG. It offers the additional advantage that it can afford high power bursts, as may occur due to run-away electrons or during disruption, without permanent damage. Whether the coating is really necessary, is not yet clear at the moment. More information on this particular point will be available by the time the final decision has to be taken.

The expected distribution of thermal load on the outer DP is shown in Fig. 3.3.9 (power to the inner DP is similar). The assumptions used, namely a total power of 2.5 MW to the outer DP and an e-folding length λ_e = 1 cm at the equator are conservative. The former corresponds to a power deposition of 50 % of the total power to the DP, which is more than is usually observed in ASDEX.

The maximum load of 3.5 MW/m^2 can be taken by inertially cooled graphite plates for pulse durations of up to 10 s. Steady-state cooling of graphite exposed to this load is not possible with presently available technology. We therefore

use inertial cooling. For 10 s pulse duration this requires a thickness of d = 2 cm. Cooling in between pulses is necessary for the planned repetition rate of 5 to 10 min. An effective heat transfer coefficient of 0.1 W/cm^2K is sufficient. This could be marginally obtained with mechanical clamping to a cooled metal plate. The design described below promises better values. The surface temperature on the hottest spot will reach 1000 C in a 10 s pulse, the graphite will be cooled to below 100 C between pulses.

Design of the DP: The design which is studied at present is shown in Fig. ?.3.10. The graphite plate (10 x 10 cm^2) is clamped to a water-cooled stainless steel plate. In order to improve the heat transfer between the graphite and the steel, a Mo/Cu sandwich is braised to the graphite.

The most severe mechanical load occurs during disruption. Due to the subdivision into individual tiles, the stresses are reduced below critical values.

Inner heat shield: As mentioned above, the bellows have to be protected from the plasma radiation. On the inside of the torus this is accomplished by an actively cooled stainless steel toroidal shield. Direct plasma contact of this shield may occur. The shield is therefore armoured with graphite mushrooms similar to those of the ZEPHYR design. Thus the shield may also be used as large area toroidal limiter. For full power operation with 50 % power deposition at the limiter it can be used for approximately 3 s.

3.3.5 The Vacuum Pumping System

The vacuum pumping system is similar to the one of ASDEX It consists of turbo-molecular pumps, backed by roots blowers and forepumps. The turbo pumps are connected to the ducts thatlead to the divertor region. The upper and the lower ducts each have one common fore vacuum line. The pumps can also be used for pumping the divertor region during the discharge. At first 14 pumps will be used in the lower divertor region. Additional pumps can be installed in the upper divertor region for double-null operation lateron. The requirement that the turbo pumps have to be at sufficiently low magnetic field results in fairly long pumping ducts plus magnetic shielding of the pumps. The conductance L and effective pumping speed S_{eff} per pump, as calculated from the design, is shown in the following table:

	Conductance L (l/s)			Effective pumping speed S_{eff} (l/s)		
	air	H	He	air	H	He
upper duct	830	2200	3100	670	1300	1525
lower duct	975	2580	3650	760	1470	1650

For estimating S_{eff} , a 3500 l/s turbo pump was assumed.

In addition a cryo pump will be connected to one of the large openings to double the pumping speed for water vapour during discharge cleaning.

With this system, we expect pumping times of 1h of fore pumping and about 10h to reach 10^{-7} mbar. The base vacuum will be in the 10^{-8} mbar range ($6 \cdot 10^{-8}$ mbar with a degassing rate of $2 \cdot 10^{-10}$ mbar l/s cm and a surface area of 300 m^2). The leaks are specified (as in ASDEX) to below $2 \cdot 10^{-8}$ mbar l/s. The leaks therefore have no influence on the base pressure or the recontamination of discharge-cleaned surfaces.

During the discharge one expects a neutral density equivalent to 10^{-3} to $5 \cdot 10^{-3}$ mbar in the divertor chamber. Thus of the order of (1 to 5)x 10^{21} H atoms l/s are pumped by the external pumps.

3.3.6 Manufacture and Assembly

The standards, quality control and assembly techniques applied to the vacuum vessel for ASDEX are identical with those required for ASDEX UG. Therefore the experience obtained in manufacture and assembly on site can directly be used for ASDEX UG. After delivery of the four vessel segments the following assembly procedure is foreseen:

- assembly of vessel segments together with 3 TF coils and respective magnet structure to modules;
- assembly of the modules, adjustment and vacuum-tight connection of the vessel segments;
- vacuum test of the vessel at room and baking temperature;
- welding of the horizontal ports, access from outside the vessel;
- welding of the vertical ports, access from inside;
- cleaning of the inner vessel wall;

- assembly of the diagnostic elements, divertor plates, separation plates, stabilization loops, ICRH antennas, heat shield, etc. inside the vessel;

- connection of cooling pipes and control elements outside the vessel;

- attachment of the vertical and radial vessel supports;

- closing the ports and assembly of the external diagnostics, vacuum system, etc;

- final leak test.

3.3.7 Collaboration with Industry

The high thermal and electromagnetic loads on the vessel on one hand and the flexibility in operation of ASDEX UG (single, double null or limiter configuration) on the other, required the development of new techniques for the vacuum vessel.

Development activities at IPP:

- application of stud welding in vacuum and nuclear engineering (German patent No. 3131055) - all elements inside the vessel will be attached by this method;

- non-destructive in situ testing device for all welded studs (German patent No. 3210825) - increase of safety margin and better use of the material;

- heat shield based on the large area limiter as developed for ZEPHYR (German patent No. 3125970) - heat shield of the inner wall of the vessel;

- expansion elements for passive compensation of thermal movements of the vessel during baking and operation - integrated in the vertical supports;

- double sealed metallic coupling for the cooling inside the vessel - divertor plates, heat shield, etc.;

- electrical breaks of the vessel - capable of transmitting shear forces of up to 700 N/mm.

Acitivities with industry:

- development of divertor plate elements for contact cooling and coaxial elements for direct cooling at the Metallwerk Plansee/Austria;

- development and testing of remote-controlled devices for welding the ports during assembly at Linde AG/ FRG;

- optimization of the vessel design concerning the distortion of the structure during welding and heat treatment - collaboration with Linde AG, FRG;

- development and testing of the double seal for the assembly joints of the vessel - collaboration with Helicoflex/FRG and France.

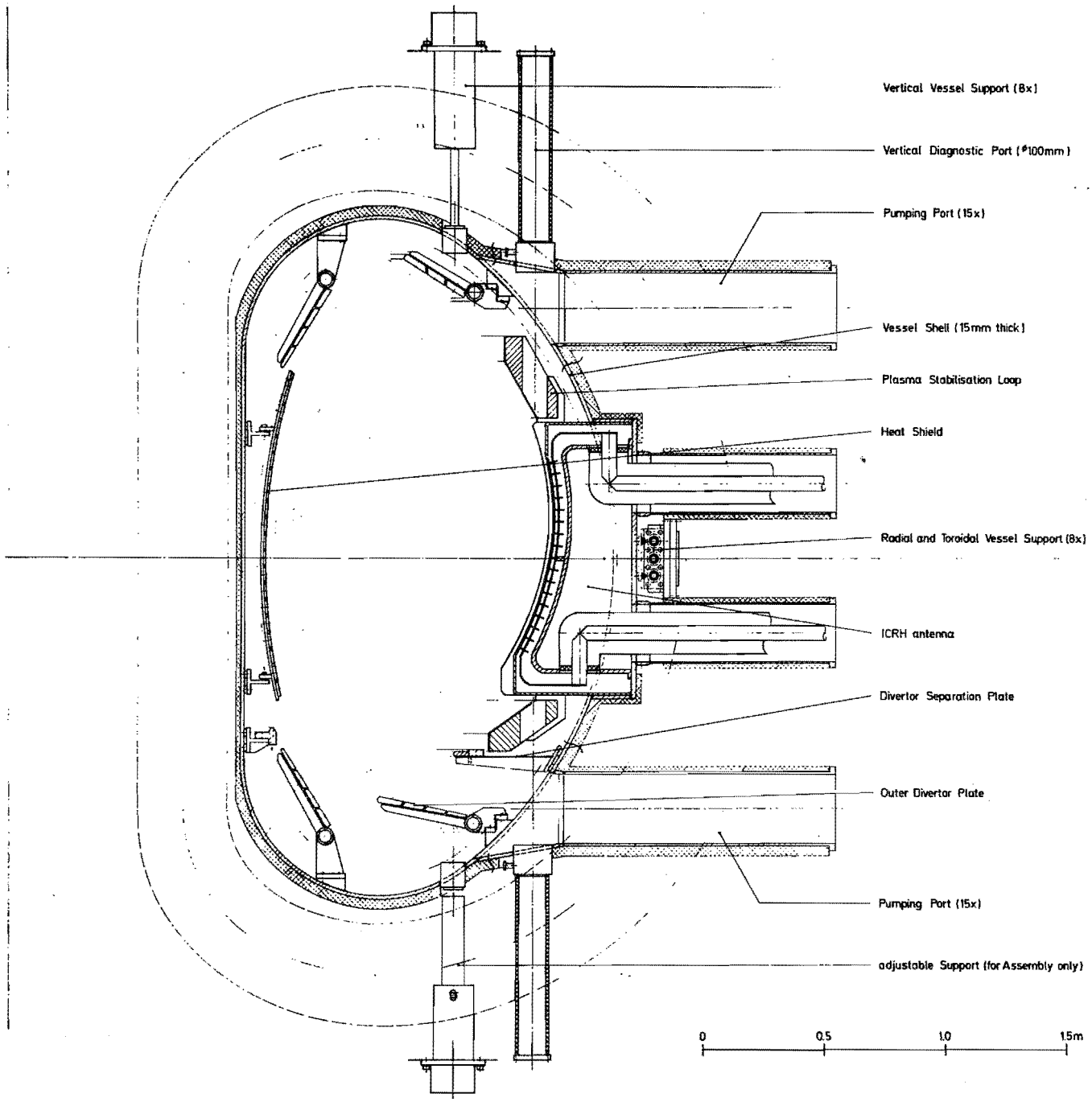

Fig. 3.3.1 Vertical Cross-Section of the Vessel

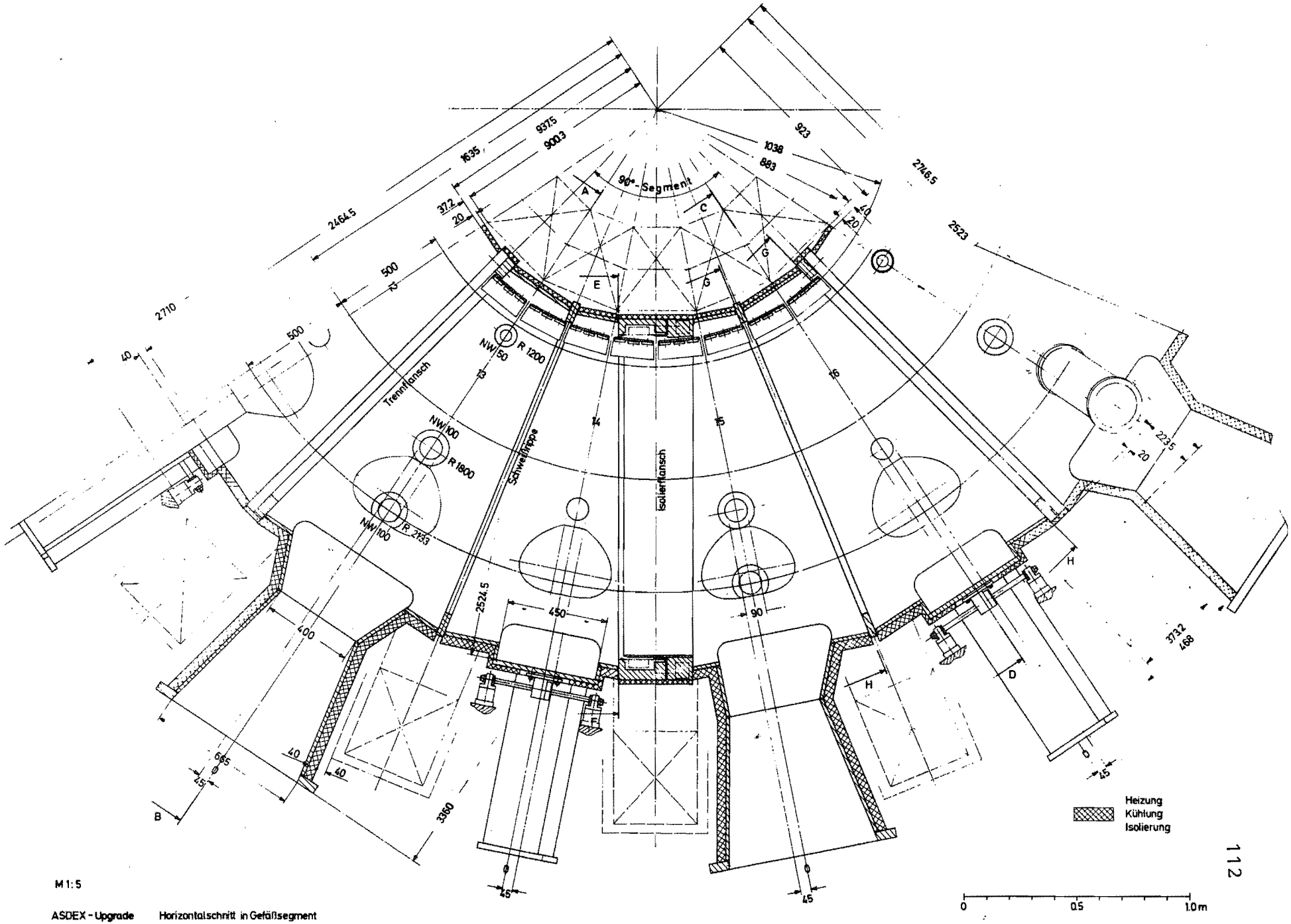

Fig. 3.3.2 Horizontal Section of a Vessel Module

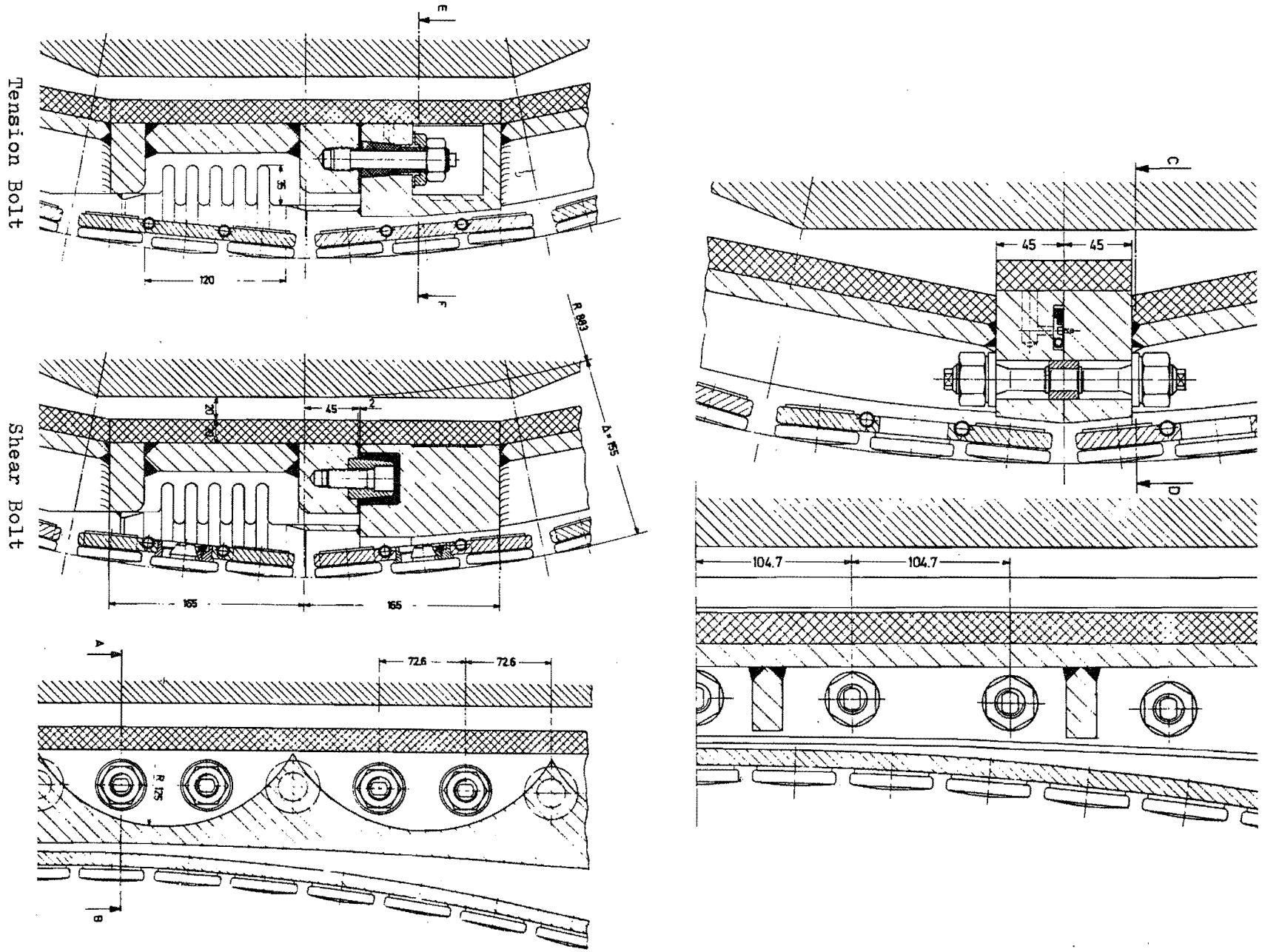

Electrical Break

Assembly Joint

Fig. 3.3.3 Design of the Assembly Joints and Electrical Breaks of the Vessel

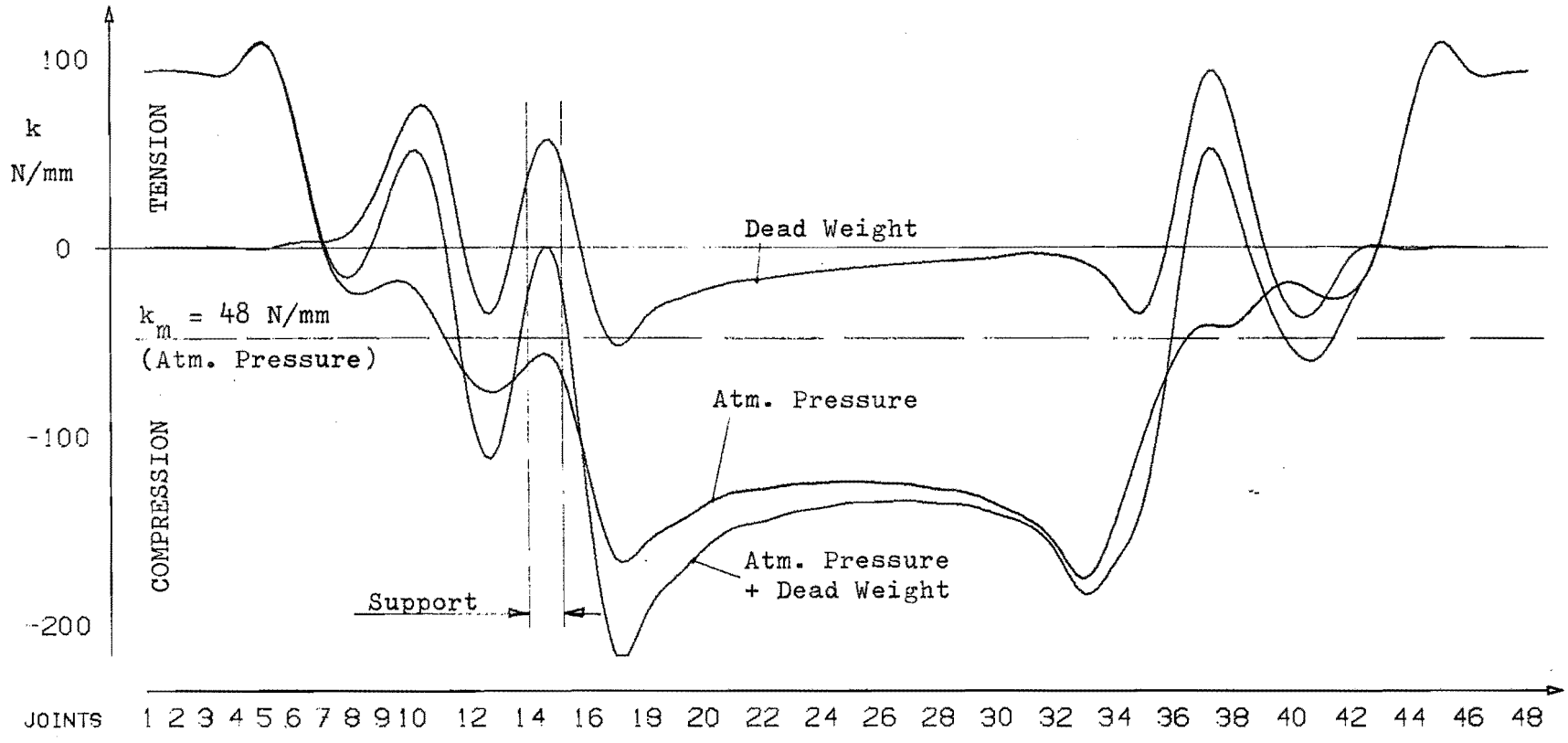

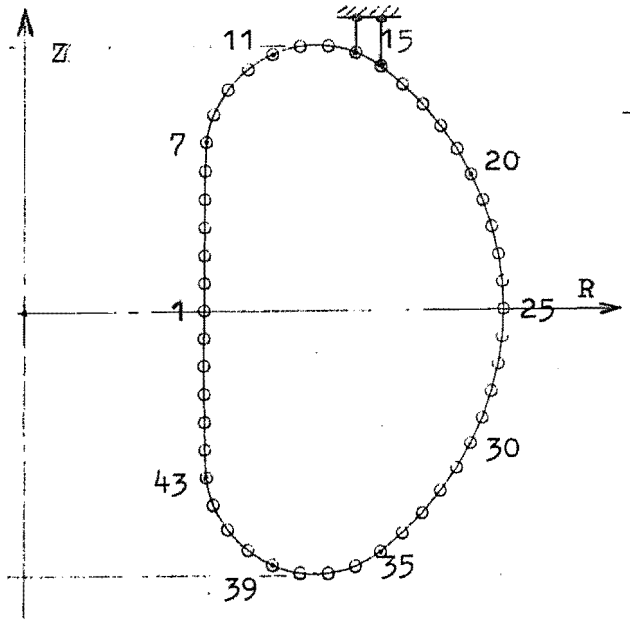

Maximum Values of	Unit	Atm. Pressure 1 bar	Dead Weight 24 t	Atm. Pressure + Dead Weight
Hoop force (tension)	N/mm	108	89	109
" (compression)	"	175	52	216
Deformation ΔR at Ri	mm	0.04	0.00	0.04
" ΔR at Ra	"	0.08	0.01	0.09
" ΔR	"	0.10	0.04	0.13
" ΔZ	"	0.17	0.69	0.83
Stress (von Mises)	MPa	12	15	19

Fig. 3.3.4 Hoop Forces Deformation and Stress in the Vessel Shell

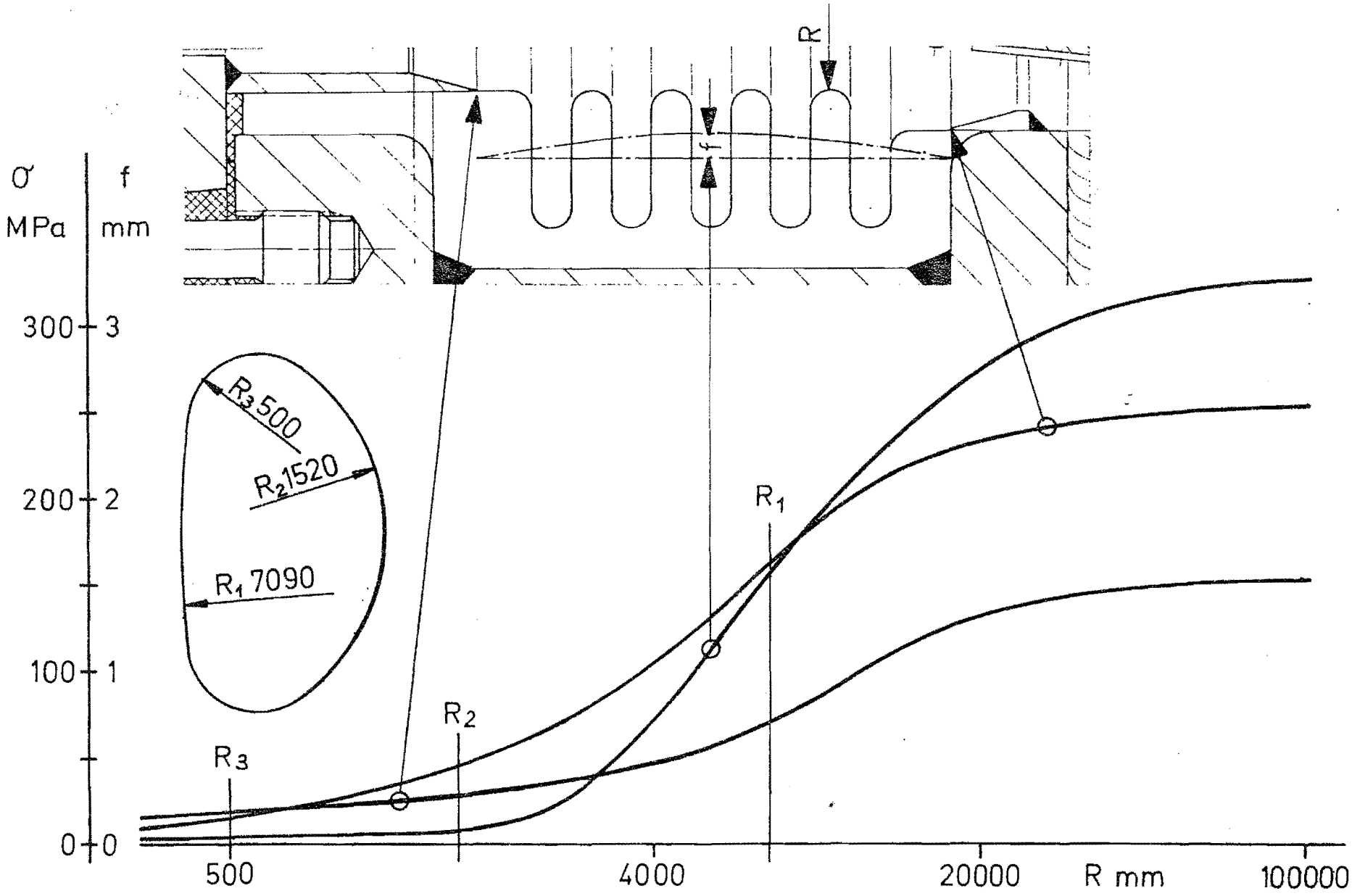

Fig. 3.3.5 Stresses and Deformation of the Bellows as Function of the Curvature
(Loading: atm. pressure)

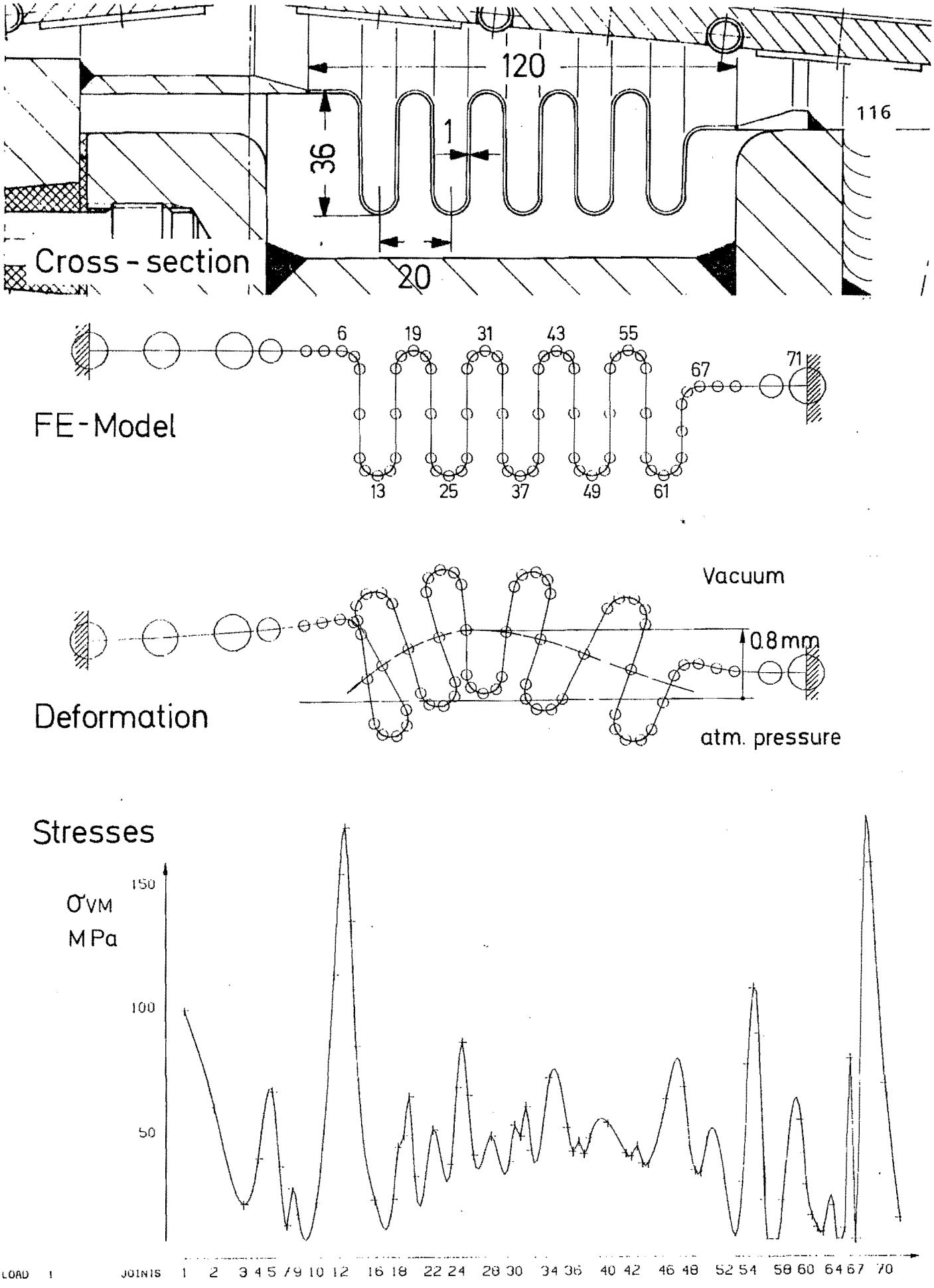

Fig. 3.3.6 Results of FE-Calculation for the flat part of the bellows (loading: atm. pressure)

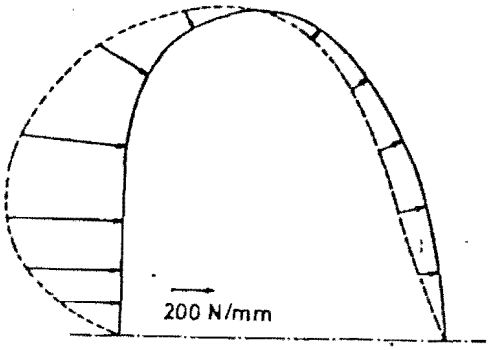

Fig. 3.3.7a Force density distribution at the electrical gap

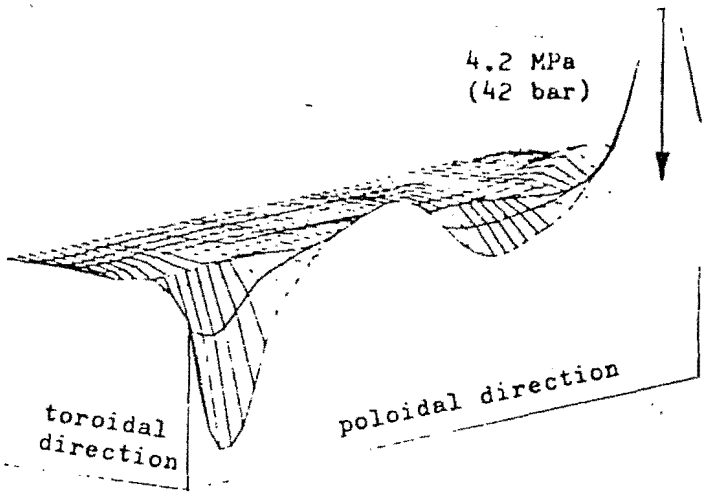

Fig. 3.3.7b
Normal pressure distribution on the vessel wall

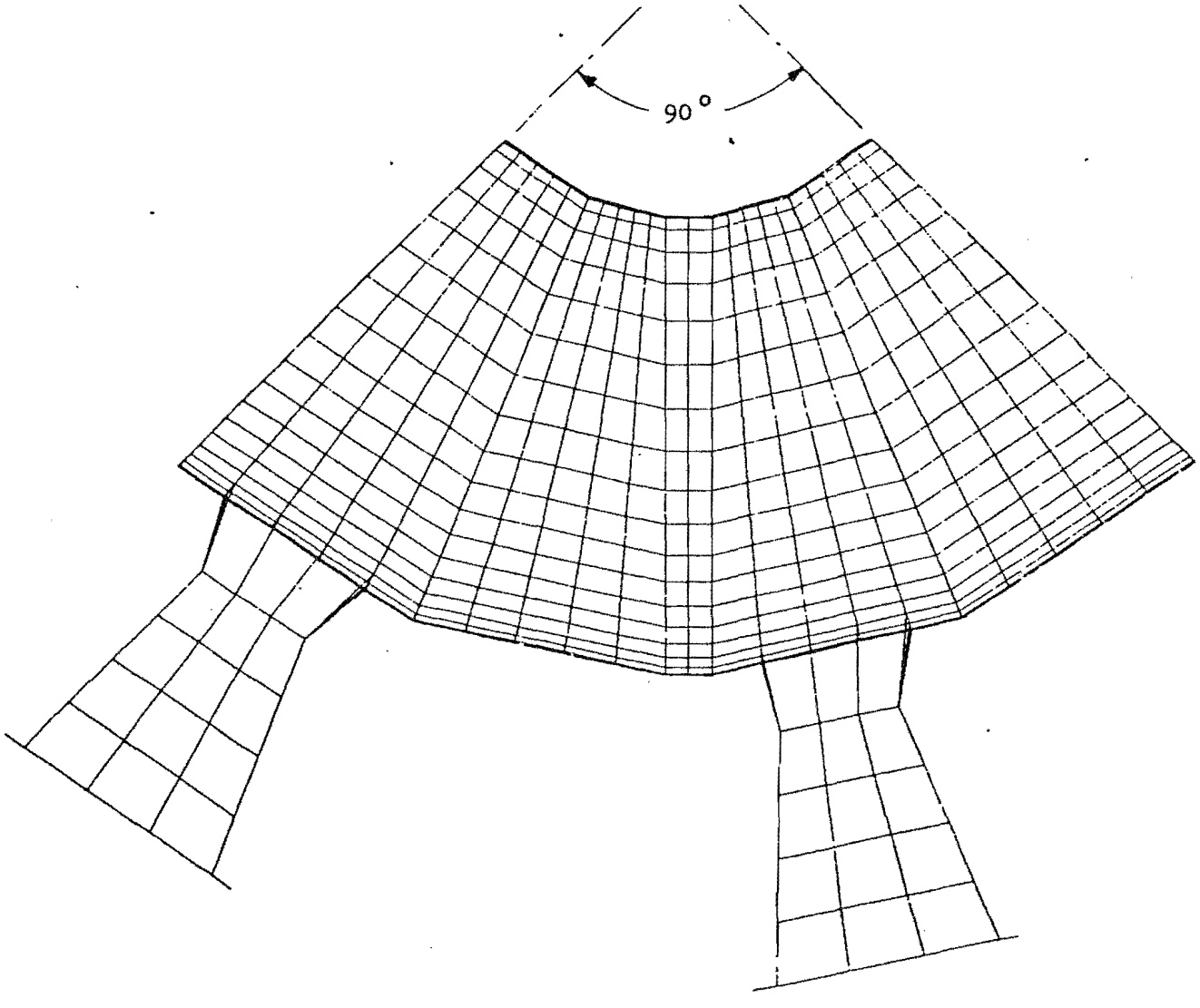

Fig. 3.3.8 Finite element mesh of one quarter of the vessel

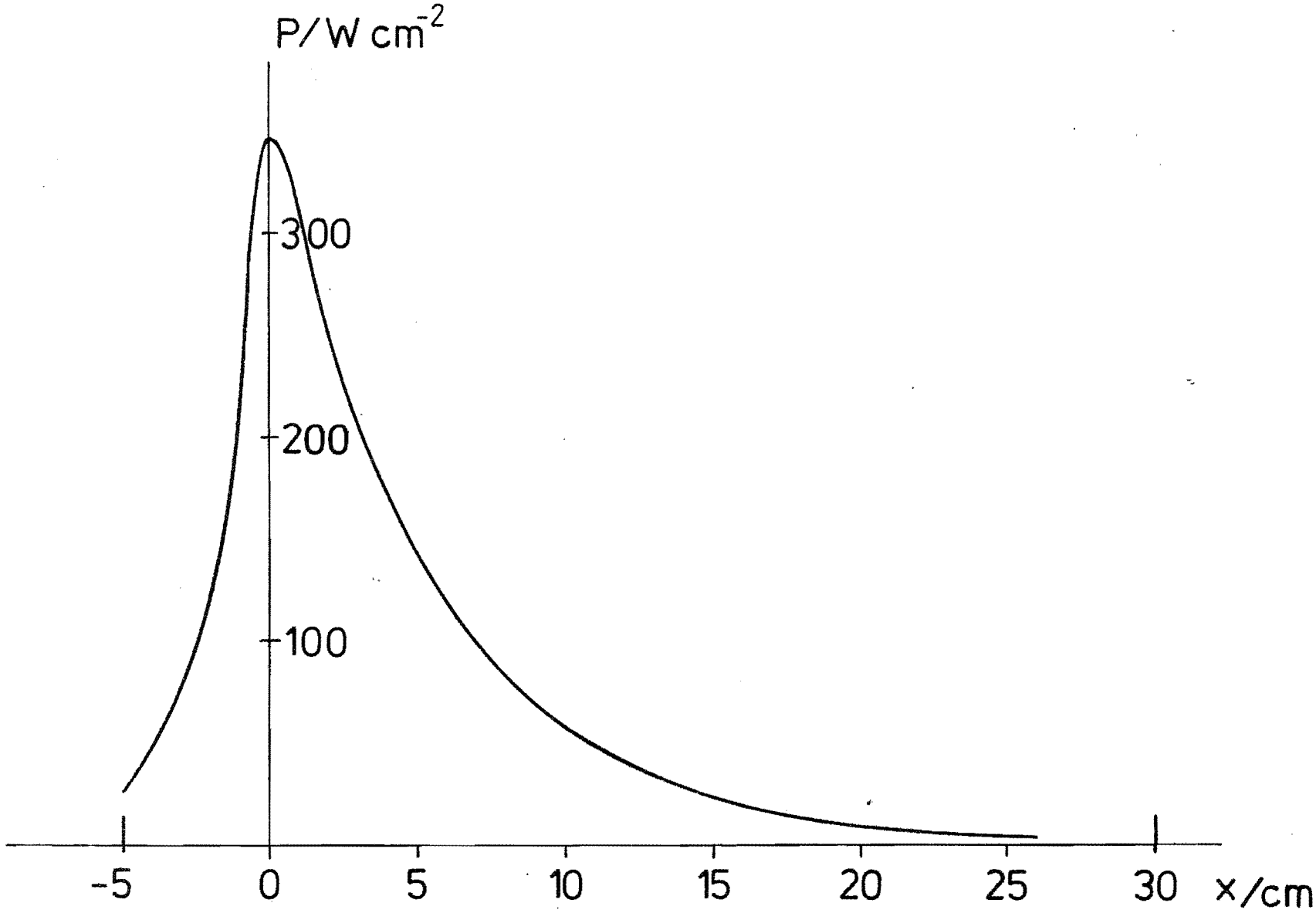

Fig. 3.3.9 Power deposition on the outer divertor plate.
(x = 0 is the intersection of the separatrix).
Assumptions: Total power to the plate = 2.5, λ_E (at equator) = 1 cm

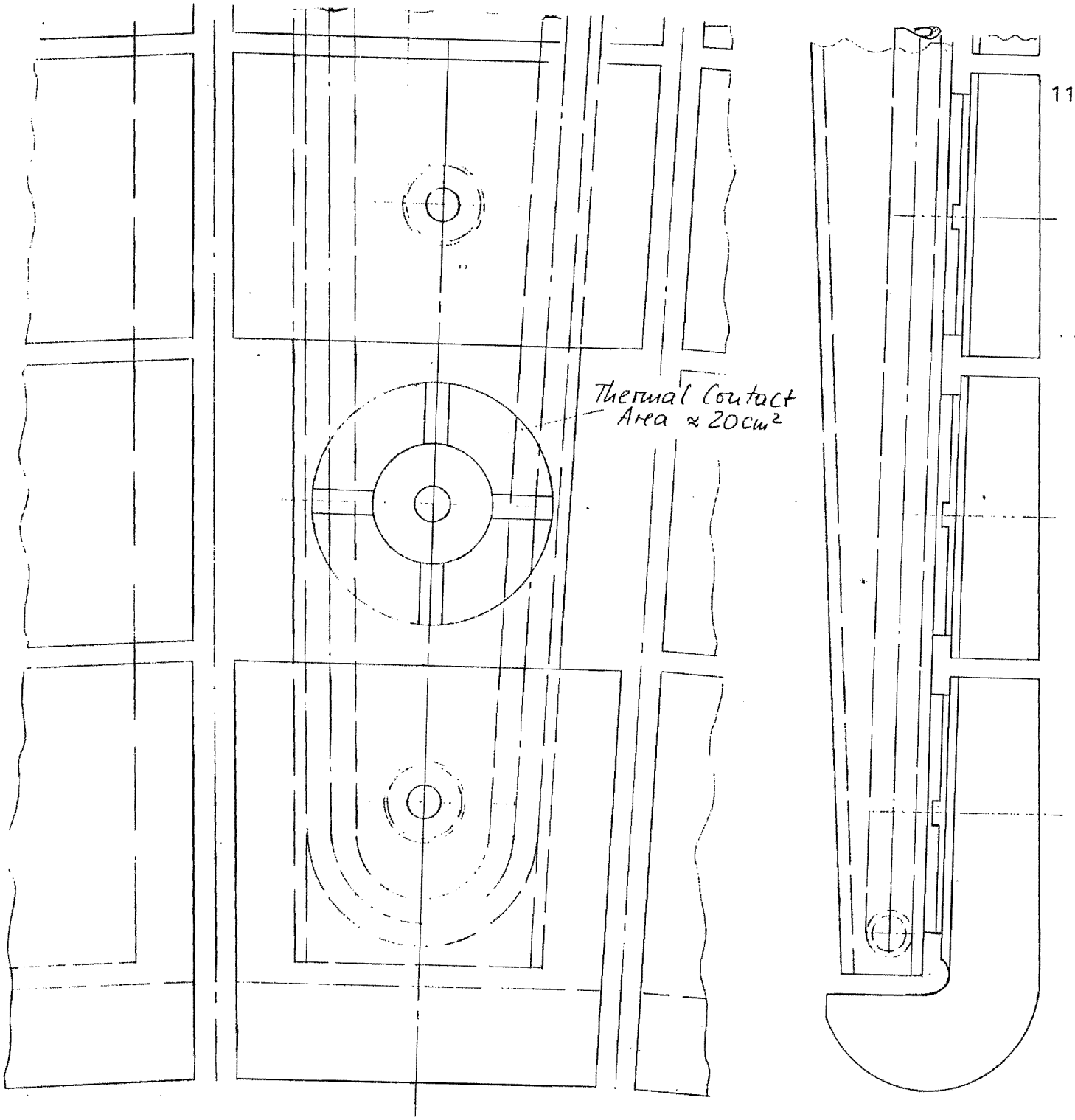

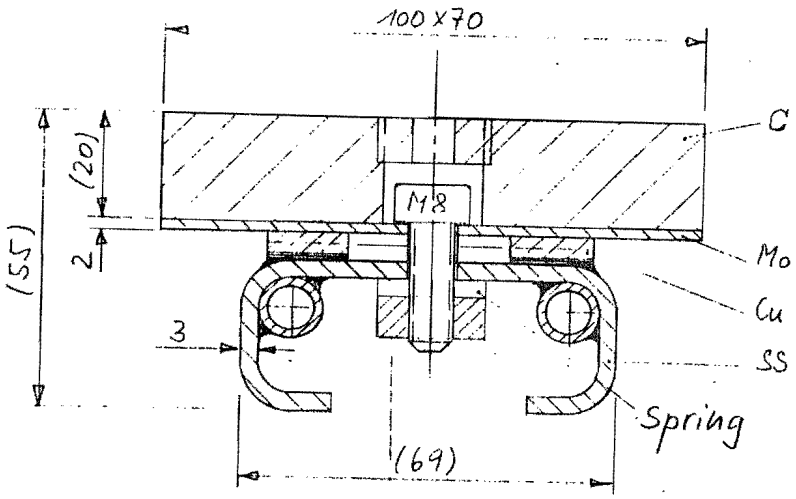

Fig. 3.3.10
Layout of the Divertor plates for contact cooling

3.4 Assembly of the Tokamak System

3.4.1 General

The modular design of the ASDEX UG tokamak system and its topologically de-coupled coil systems allow simple and time saving assembly.

The toroidal system is subdivided into four 90 degree sectors. Two of them will be assembled in their final positions. Two others will be assembled on moveable platforms which will then be shifted toward the fixed ones and connected with them. The poloidal field coils have got a support structure of their own which can be set up after the four toroidal sectors have been mounted.

The choice of the assembly concept has been guided by the idea to use only standard assembly techniques. Remote assembly, disassembly and maintenance are not envisaged because the activations of the structure will be kept low enough in any case.

The assembly facilities, e.g. cranes, hydraulic jacks etc., will be made of ferromagnetic steel and removed from the experimental area after completion of assembly. As a result the access to the plasma is not hampered by stationary assembly equipment.

3.4.2 Prerequisites for Assembly

- preparation of the building is finished;
- the foundations have been integrated into the basic plate
- the radiation shielding wall is finished;
- the radiation shielding ceiling not yet mounted;
- test assembly of vacuum vessel, TF and PF structure have been successfully terminated.

3.4.3 Assembly Sequence

a. Mount the 8 vertical TF support bearers.
b. Deposit multipole coils V1u and V2u on floor concentric to the center of experiment.
c. Set up the assembly platforms for the four toroidal sectors.
d. Assemble sectors II and IV in their final position and sectors I and III on the moveable platforms, as follows:
   d.1 set up 90 degree sector of vacuum vessel on assembly platform;
   d.2 thread on 3 TF coils on vacuum vessel;
   d.3 assemble lower TF structure elements;
   d.4 set 90 degree vacuum vessel on lower TF structure;
   d.5 assemble upper TF structure elements;
   d.6 pre-assemble the elements inside the vacuum vessel.
e. Deposit CH coil 1 on floor of experiment hall concentric to center of experiment.
f. Shift moveable sectors II and IV in their final position and connect TF structure to a torus.
g. Connect vacuum vessel segments to torus.
h. Weld in the missing two horizontal ports.
i. Weld in all vertical ports;
j. Disassemble assembly platforms.
k. Cast the tolerance balancing elements at TF vault and TF structure.
l. Adjust and fix vacuum vessel within TF structure.
m. Place CH coil 1 and central column in their final position and preassemble the other PF coils close to their final position.
n. Set up PF structure and assemble of PF coils.
o. Disassemble all assembly facilities.
p. Install bus bars, cooling tubes, pumping ducts, etc.

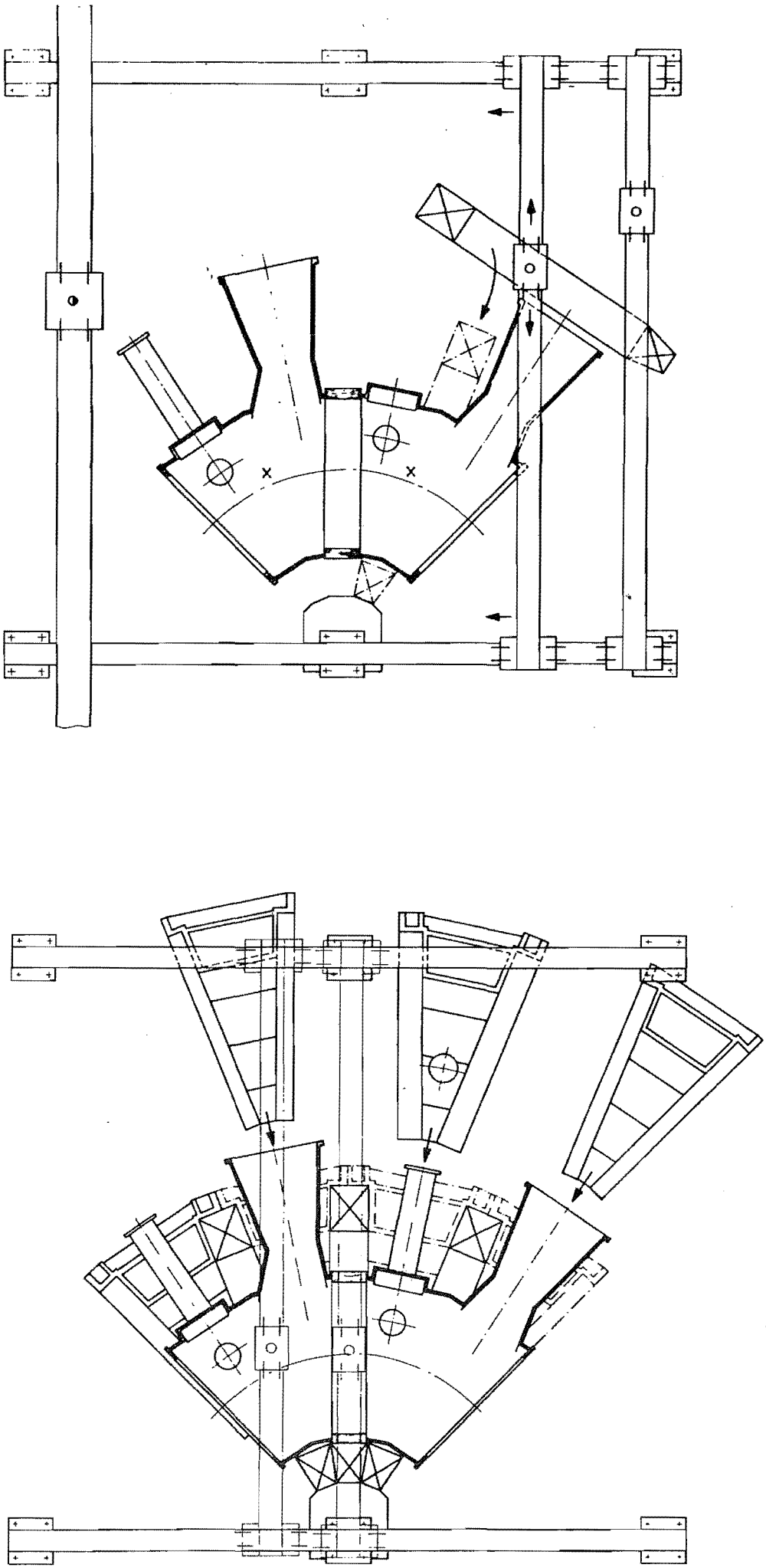

Fig. 3.4.3.1 Assembly of 90 Degree Modul

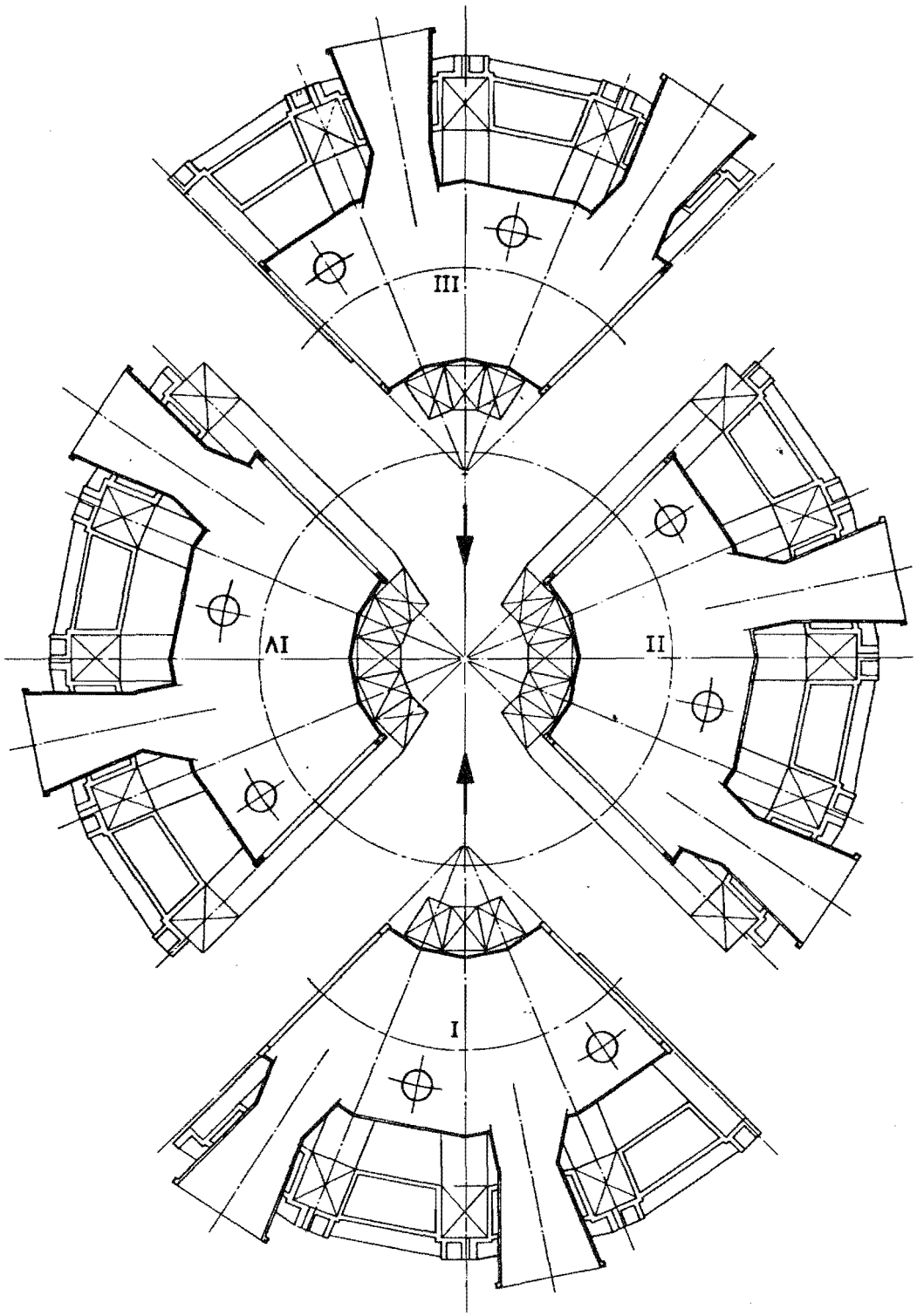

Fig. 3.4.3.2 Assembly Principle

4. Power Supply

4.1 Load Components

Steady-state and emergency power consumption of ASDEX UG is very similar to that of the existing experimental devices at IPP. Therefore both requirements can be covered by supply facilities already available.

Pulse power is needed for:

- toroidal field coils;
- OH transformer;
- multipol coils;
- auxiliary plasma heating and
- plasma stabilization loops.

Pulse power can be provided by IPP's fly wheel generators up to parameter ranges envisaged at present. Adaption of rectifiers to load data is necessary. The maximum parameters which the tokamak system is designed for, can be attained for each individual component. For simultaneous operations of all components the choice of parameters has to be adjusted to the power and energy limitations.

4.2 IPP's Pulse Power Facilities

Data of fly wheel generators GEZ 2 and GEZ 3

	GEZ 2	GEZ 3
Energy (MJ)	1450	500
Power (MVA)	167	144
Voltage (kV)	2x2.75	10.5
Current (kA)	2x17.5	8
Frequency (Hz)	85-110	85-110
Pulse length (s)	10	4
Pulse break (s)	360	180
Data of rectifiers:	REZ 2	REZ 3
Number of modules	2	12*)
Type	diode	thyristor
Power (MW)	2x75	12x22,5

Voltage (kV)	3.3	1
Current (kA)	22.5	22.5
Mode of operation	series parallel	series parallel

*) Two rectifiers can be operated in current reverse mode.

4.3 Maximum Requirements for Individual Components

4.3.1 Toroidal Field Magnet

Fig. 4.3.1.1 shows voltage, current, power and energy of the toroidal magnet versus time for its maximum field of 4 T. The current rise time of 8 s is determined by the maximum voltage of the rectifiers of REZ 3.

Fig. 4.3.1.2 shows a circuit diagram of the toroidal field power supply. The two fly wheel generators are operated in parallel. As the frequencies of the generators can be different, chokes are necessary to avoid loop currents.

The TF magnet is symmetrically grounded by a fuse. In case of an accidental earth leakage, the fuse interrupts the earth loop and major energy deposition at the earth leakage area can be avoided.

4.3.2 OH Transformer

Fig. 4.3.2.1 shows the electrical data of the OH circuit versus time for a maximum plasma current of 2 MA in the case of single null operation. Total magnetic flux swing: 9.5 Vs.

Fig. 4.3.2.2 shows the circuit diagram of the OH circuit. It is based upon that of W VII which has been successfully in operation for several years.

Excitation Phase: The breakers Q1a and Q1b are open. Q2 is closed. The rectifiers REZ 3a and REZ 3b charge the OH coils at a constant voltage to its maximum current of 47.5 kA.

Break-down Phase: Toward the end of the excitation phase the vacuum breakers Q1a and Q1b close and Q2 opens. The valves V1 and V2 ignite and the precharged capacitor C forces the current of the breakers to zero. So Q1a and Q1b can be opened and the OH current is commutated into R2. As a result the current drops at a time constant of L/R and

this induces the ignition voltage in the plasma (approx. 50 V). The saturable inductance LS decreases the dJ/dt when the current is close to zero and facilitates circuit breaking.

Low-β_p-Phase: Already during the break-down phase the voltage of the rectifiers is reversed. At a constant level of 2.4 kV the plasma current can be increased up to 90 % of its maximum value within 1.5 s. This rise time was chosen in order to keep the power necessary for the multipol coils within the limits of the pulse power capacity.

Heat-up and High-β_p-Phase: During these phases simple rectifier control provides the current changes necessary for the plasma voltage required (0.25 V during plasma current flat-top).

4.3.3 Multipol Coil System

Fig. 4.3.3.1 shows the currents in the individual multipol coils and the total power and energy required for single null operation at a plasma current of 2 MA. For simplicity the voltages have not been shown but are quoted in Fig. 4.3.3.2. This single null mode denoted as SN 1, is characterized by relatively low power and energy requirements. Single null mode SN 2, which is quoted in other parts of this report, cannot be operated up to a plasma current of 2 MA because of the high power required for the multipol coils during the current rise time. Operation up to 1.6 MA plasma current is possible.

For double null operation the power requirements are much higher than for single null operation. Therefore the plasma current for double null operation is limited to about 1.2 MA. Fig. 4.3.3.2 shows the circuit diagram for SN 1 operation. Each coil has got a rectifier of its own because of the different currents. A supply system where the upper and lower multipol coils have different numbers of turns which are switched two by two in series is under investigation.

The coils V2o and V2u could also be used as a means for active vertical plasma stabilization. This and a solution employing independent stabilization coils has been investigated.

4.3.4 ICRH Heating

The most likely heating concept to be chosen for ASDEX UG is ICRH. The total heating power amounts to about 10 MW. Assuming an efficiency of 50 %, an electrical input power of 20 MW is necessary. This power will be provided by the fly wheel generators on the 3-phase AC level. The rectifier modules are considered to be part of the heating system.

4.4 Pulse Power for Reference Operation

Fig. 4.4.1 shows the power requirements for the toroidal field system (TF), the OH transformer (OH), the multipol coils (MP) and ICRH heating for the reference operation data of

B_o = 3.25 T and
I_p = 1.6 MA

in the case of single null operation (SN 1). The addition of these figures yields the total power P_t which is well below the maximum power available for a pulse length shorter than 10 s. The integral of P_t provides the total energy W_t required for reference operation. The energy which can be withdrawn from the fly wheel generators allows a pulse length of approx. 8 s.

In principle the circuits are the same as already shown in sect. 4.3.

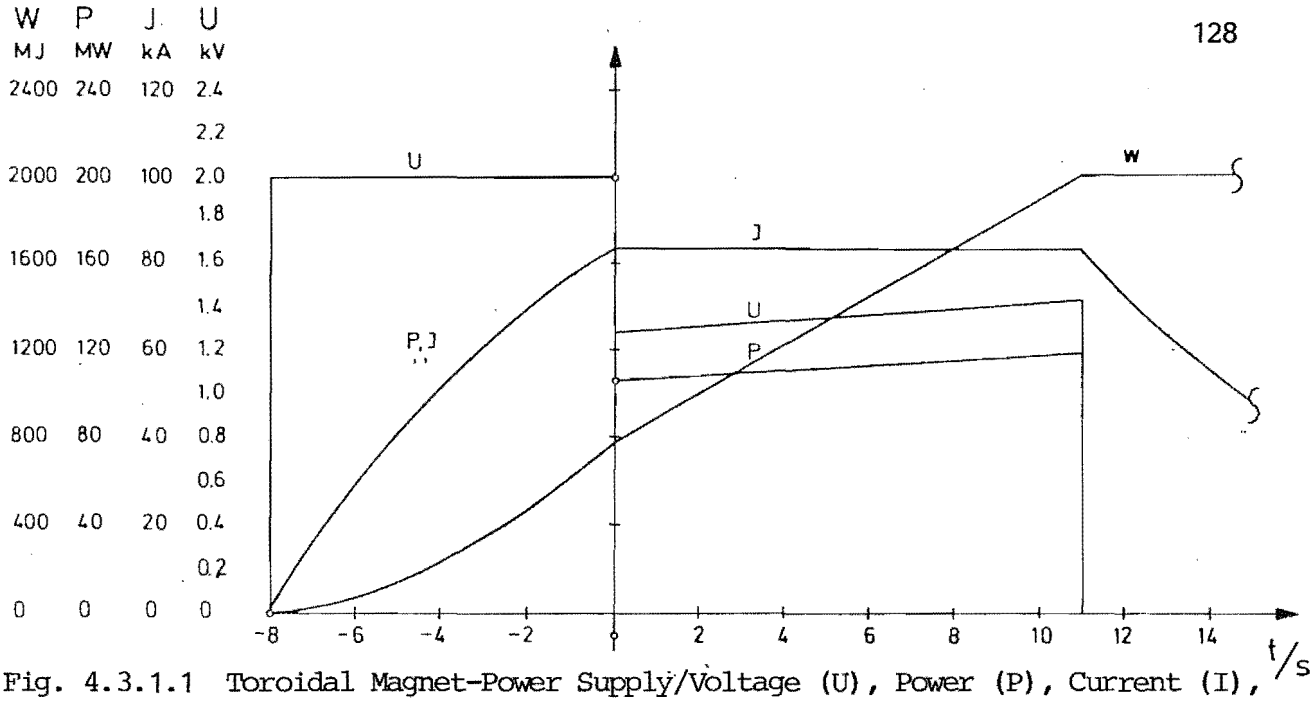

Fig. 4.3.1.1 Toroidal Magnet-Power Supply/Voltage (U), Power (P), Current (I), Energy (W) versus time; $B_o \approx 4$ T;

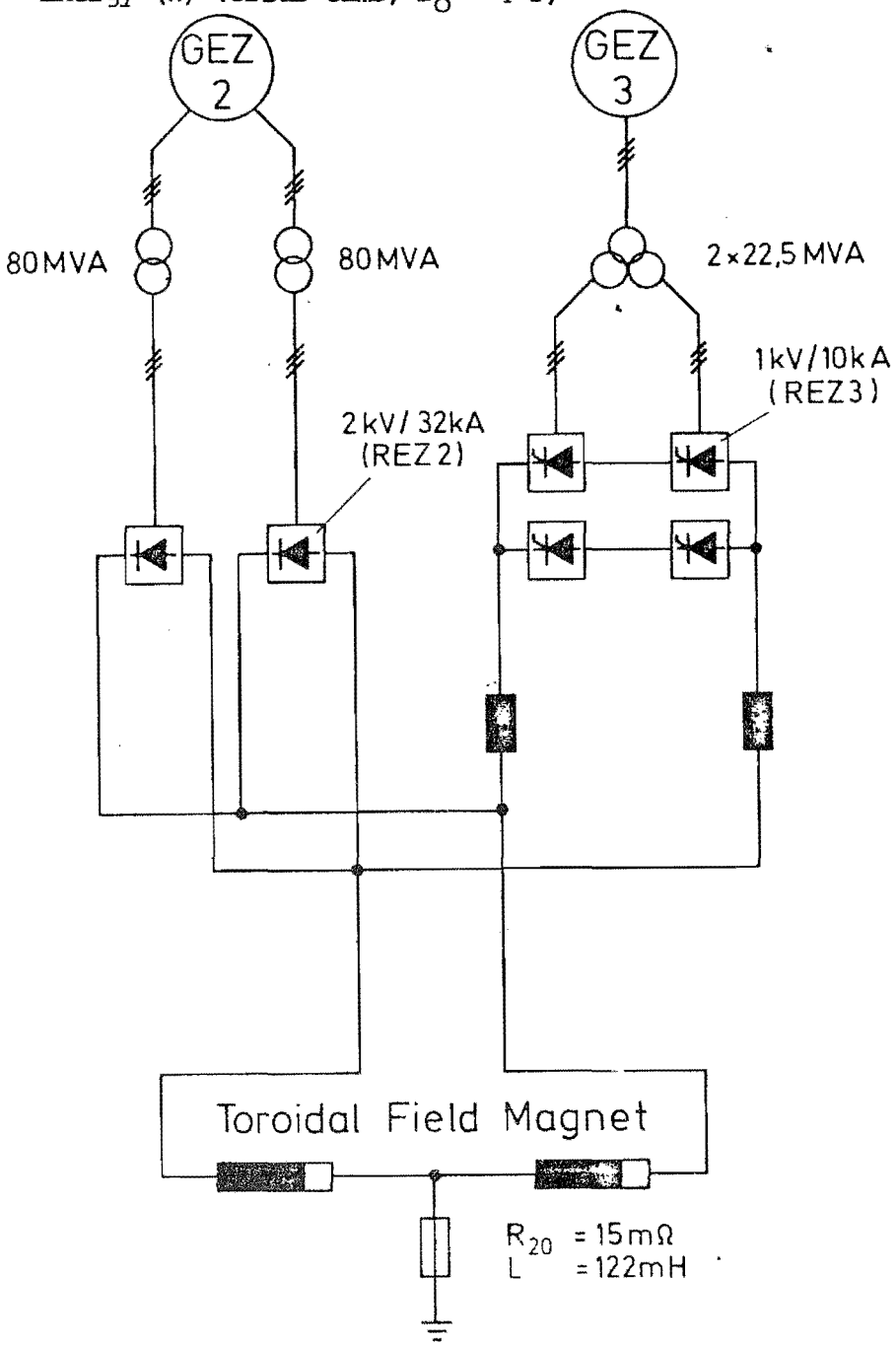

Fig. 4.3.1.2 Toroidal Field-Power Supply/Circuit Diagram;

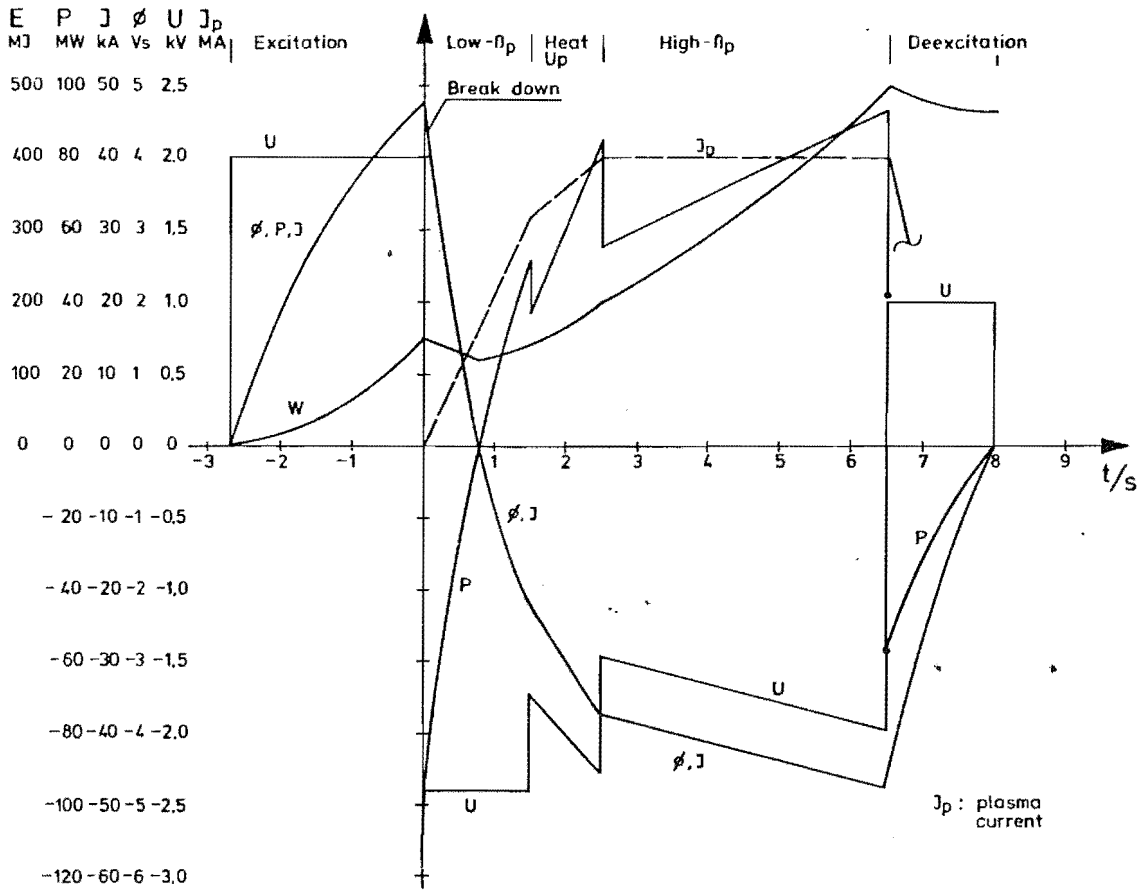

Fig. 4.3.2.1 OH-Transformer-Power Supply/Voltage (U), Current (J), Power (P), Energy (W), Flux (ø) versus Time (t)

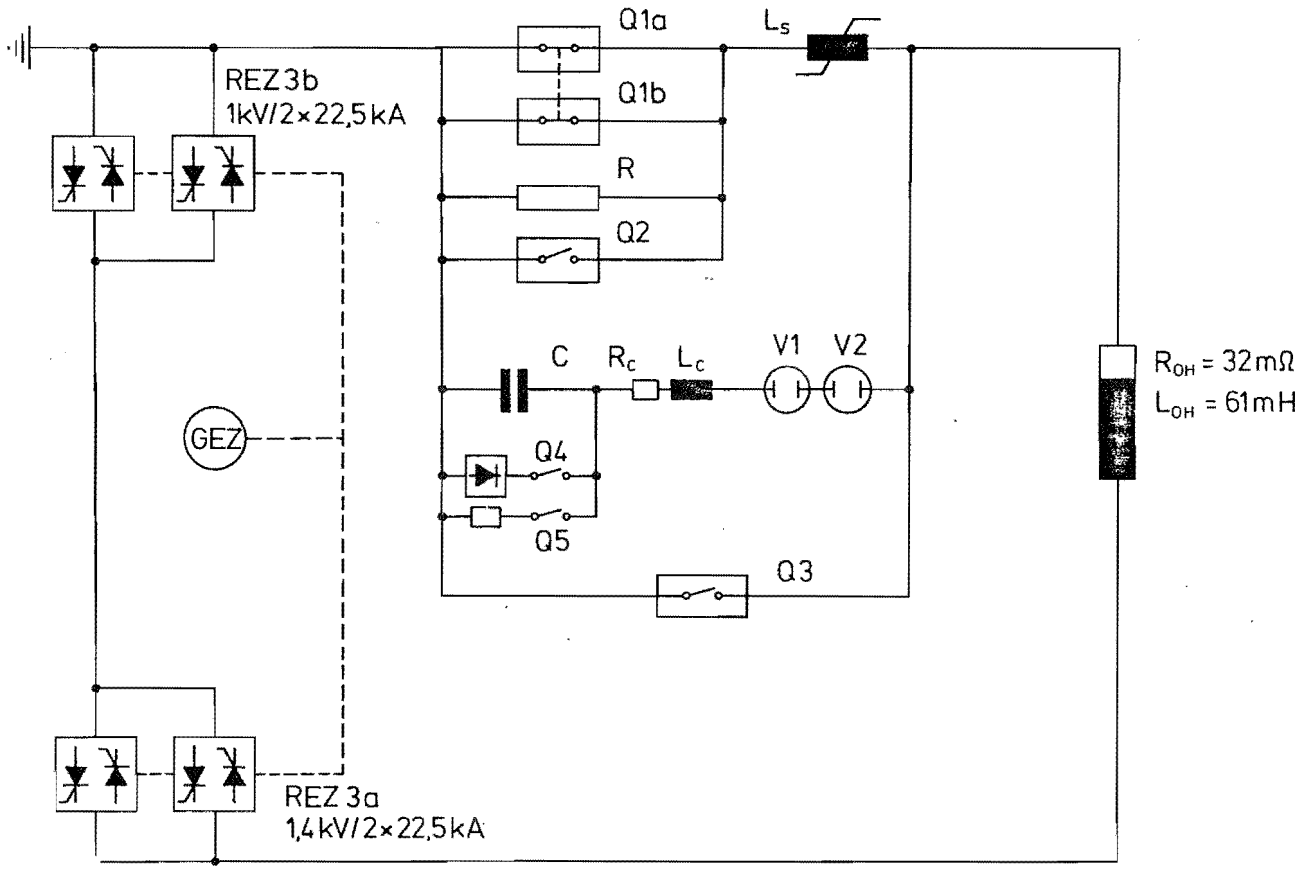

Fig. 4.3.2.2 OH-Transformer-Power Supply/Circuit Diagram

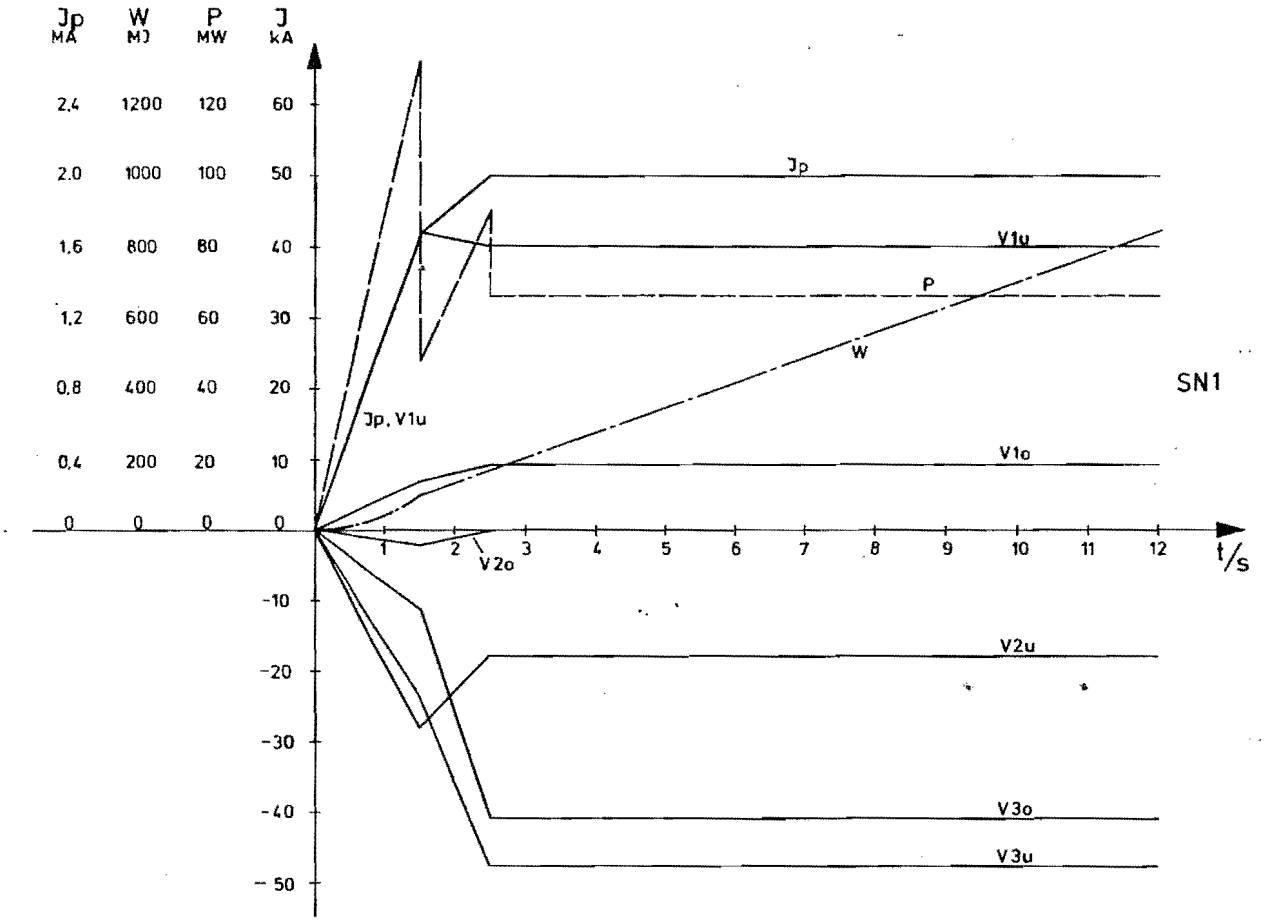

Fig. 4.3.3.1 Multipol System-Power Supply/Currents per coil (V), Plasma Current (I_p), Total Power (P) and Energy (W) versus time; Single Null Operation (SN1)

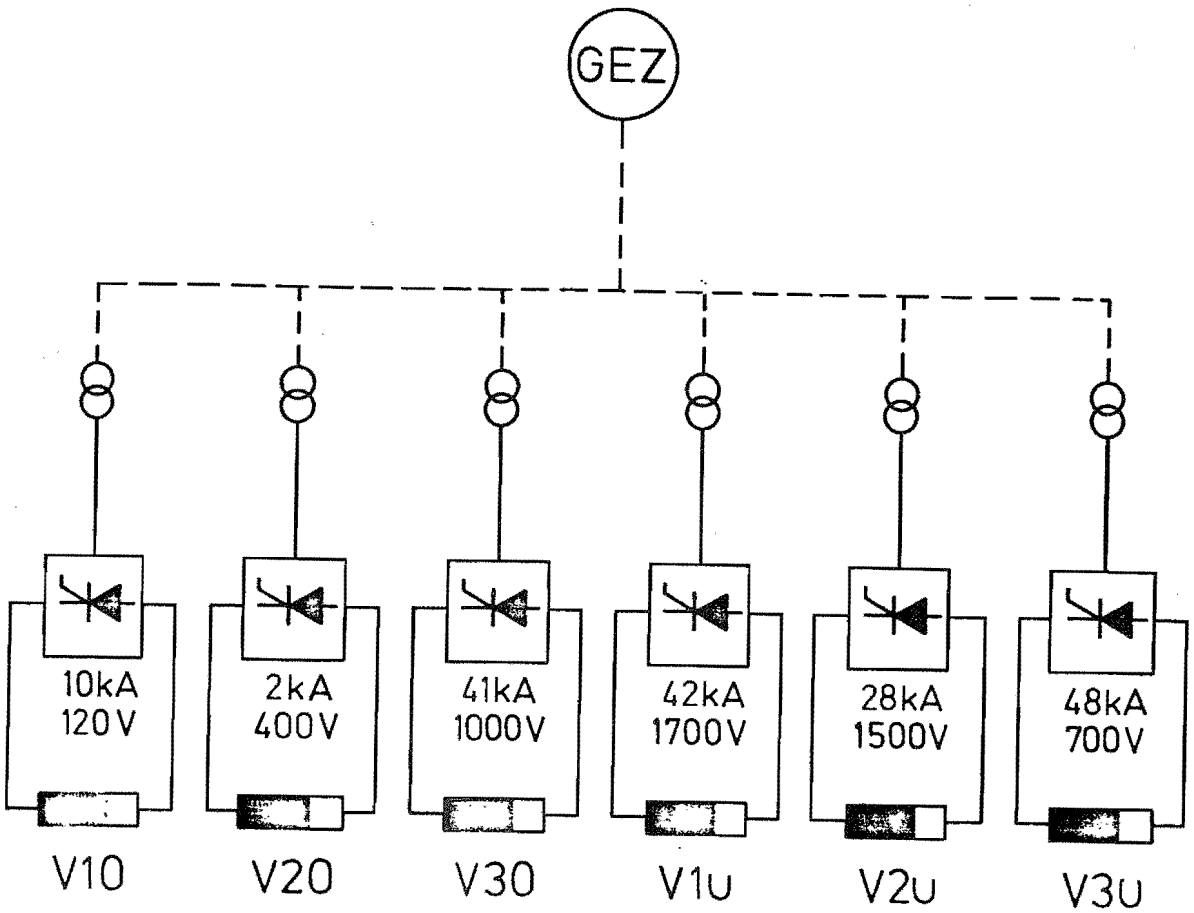

Fig. 4.3.3.2 Multipol System-Power Supply/Circuit Diagram

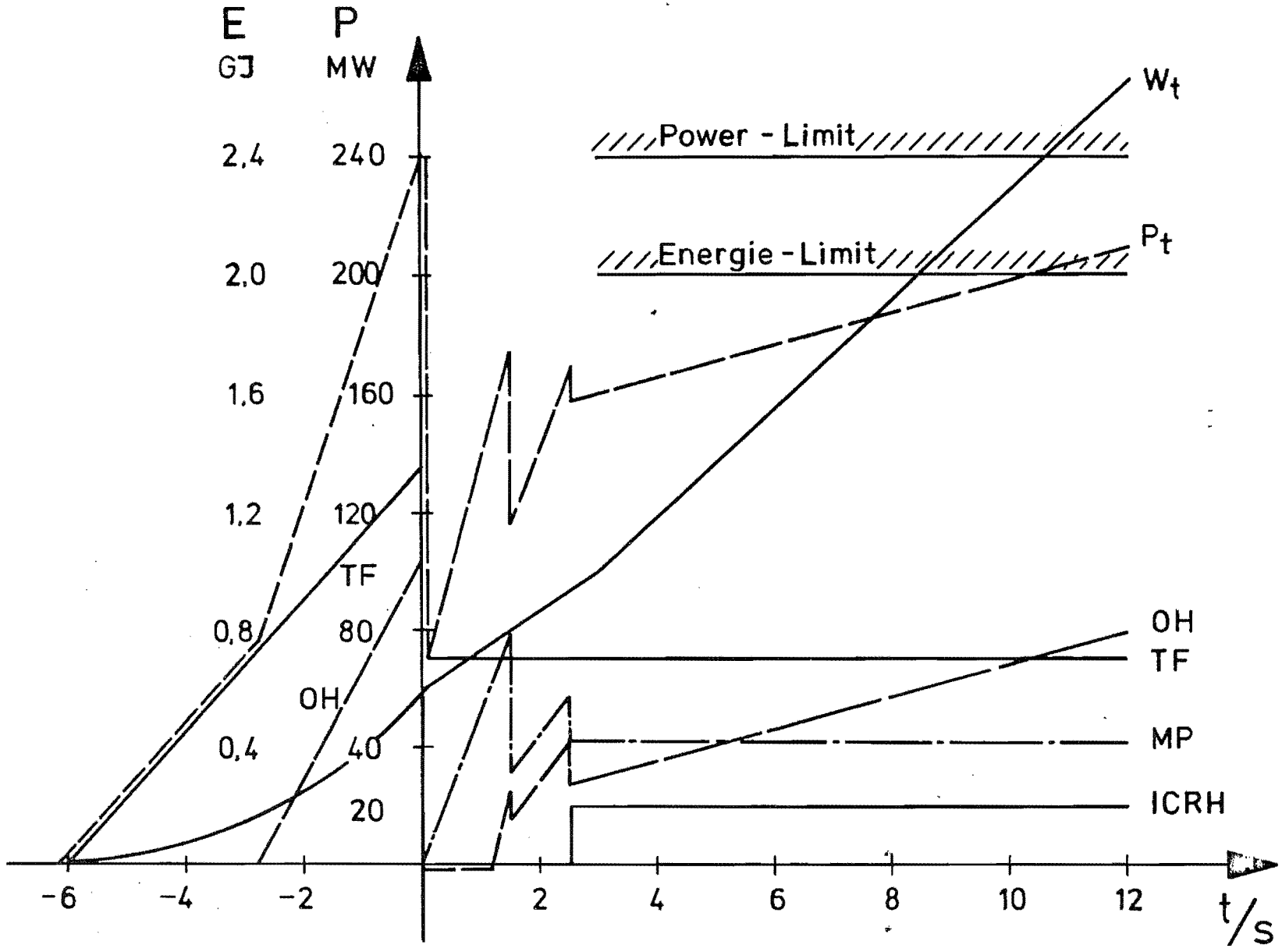

Fig. 4.4.1: Reference Operation/Power of Components and total Power (P_t) and Energy (W_t) versus time; B_o = 3.25 T, I_p = 1.6 MA, Single Null Operation.
The reference case of Table II, (page 7) yields larger discharge durations because of the 2.7 T reduced toroidal field.

5. Ion Cyclotron Resonance Heating

5.1 General Remarks

The ICRH system for ASDEX UG will be subject of a separate application for preferential support to be presented in due time. Some basic remarks will be given here.

ICRH shall be applied to ASDEX UG at the 2nd harmonic frequency of hydrogen in the range between 80 and 120 MHz with a total power of 12 MW for 10 sec (see sect. 2.2.4). Although ICRH has been successfully applied in recent years in the MW power range at several experiments, long-time heating at this power level and within this frequency range calls for further development, at least in the case of RF generators and antennae.

5.2 RF Generators

Long-pulse RF generators with MW power levels and with a tunable frequency range between 80 and 120 MHz have not been built up to now. Further development will be necessary, mainly because the output power of available tetrodes decreases in this frequency range caused by the screen grid load and because parasitic oscillations are a problem especially for tunable generators.

Experience with the industrial generator development for ASDEX and W VII will be helpful, first test results being available in late 1983. These 1.5 MW generators will be tunable, in principle, between 30 and 115 MHz (the output power being decreased above 80 MHz), but only tested at 12 fixed frequencies. This should be a possible concept for ASDEX UG too.

It is intended to invite industry to study contracts in order to check the possibilities to increase the output power of tetrodes in the required frequency range. This would be of large economical interest, since the valve takes only about 10 % of the generator cost but determines its power and thereby the number of parallel generators required.

The two RF generators for ASDEX / W VII can be applied to

ASDEX UG too within their parameter limits.

5.3 Antennae

The development of antennae for long-pulse heating at MW power levels is the main ICRH task of the next years. Four European groups in Brussels, Culham, Fontenay-aux-Roses and Garching are working in this field and are in contact with each other. The first MW antennae designed for pulse lengths of few seconds will be operational in TEXTOR in 1983 and in ASDEX in 1984; cooled ASDEX antennae for 10 s and antennae for JET will follow. The antennae for ASDEX UG will fit in this development work and experience with other experiments will be used.

Up to now, preliminary calculations and a very rough design has been worked out in order to demonstrate the proposed device's capability to accommodate an antenna of suitable performance. A folded (JET-type) and an ASDEX-like antenna have been taken into account. The space required being larger for an ASDEX-type antenna, this one has been worked out in more detail.

The electrical design is based upon 2-dimensional plasma antenna coupling calculations /1/ whose results (specific inductivity, capacity and resistivity) are used to model the dependences in the 3rd dimension by transmission line theory. The model for the plasma antenna coupling calculations is shown in Fig. 5.1. The distances plasma - antenna and Faraday screen - central conductor are compromises in order not to interrupt the energy flow to the divertor still allowing a good coupling, and in order to adjust both the voltage in the antenna and in the feeding system at moderate levels.

For a radiated power of 1 MW at 100 MHz and a 30 Ω feeding line the following characteristic antenna data were found:

spec. inductivity	1.3 nH/cm
spec. capacity	3.6 pF/cm
spec. resistivity	0.25 Ω/cm
antenna length	40 cm
electrical length /λ_o	0.27
input voltage	12.9 kV
VSWR	3.1

The frequency dependence of the antenna's input impedance is shown in Fig. 5.2.

The total ICRH antenna system for ASDEX UG will be composed of 8 single antennas arranged along the toroidal direction of the outer circumference of the experiment. Each

antenna consists of two identical dipoles above and below the experiment's midplane and fed by opposite phases. Supposing as above, a power radiating capability of 1 MW for one dipol, the total arrangement should be able to transmit a total HF power to the plasma of $P_{tot} \approx 16$ MW

The present conception of the basic constructive set-up of a single antenna is shown in Fig. 5.3. The antenna is now shaped to match best the particular plasma shape of the single null operation. An antenna shape which is a compromise for the two operation modes will be looked for.

The feeding configuration is conditioned by the total poloidal geometry of the experiment and may suggest the use of antennae of the folded dipol type (like JET). Calculations for the electrical design of such an antenna are being carried out.

Screening the energy flux to the antennae carried by charged particles along the field lines, the guard limiters are exposed to a thermal loading of up to 50...100 W/cm requiring active cooling measures. Plasma radiation, remaining particle flux and HF losses may lead in the Faraday screen to a power dissipation of the order of 30 W/cm . Since active cooling may turn out as too complicated and pure radiation cooling must be relied on, temperatures of the Faraday screen of up to 350 C must be coped with.

Ref.:

/1/ M. Soell: Proc. 3rd Joint Varenna-Grenoble Int. Symp., Grenoble 1982, pp 415-421.

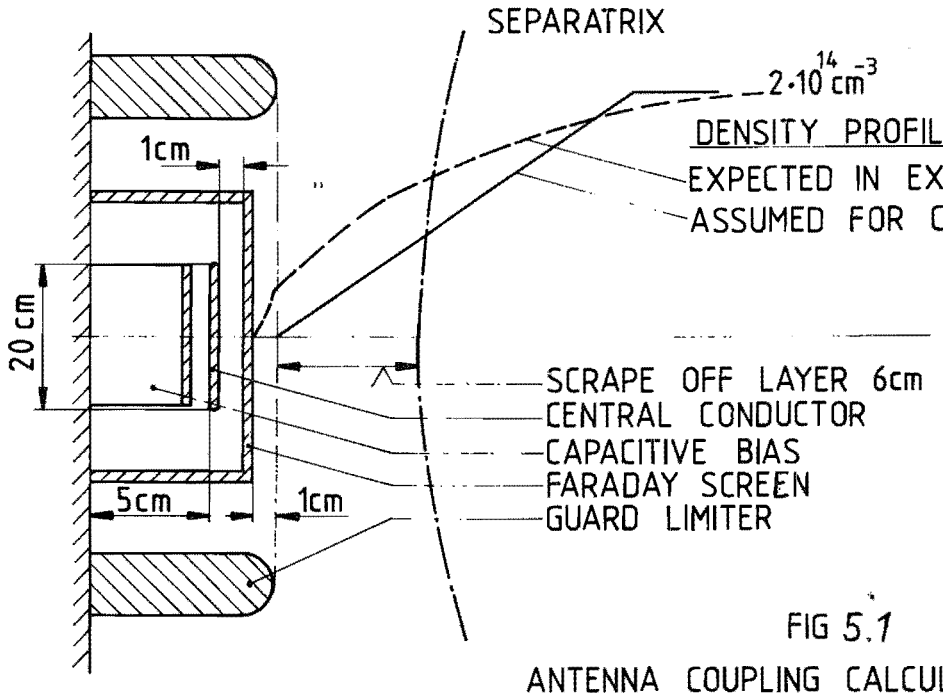

FIG 5.1

ANTENNA COUPLING CALCULATION MODEL

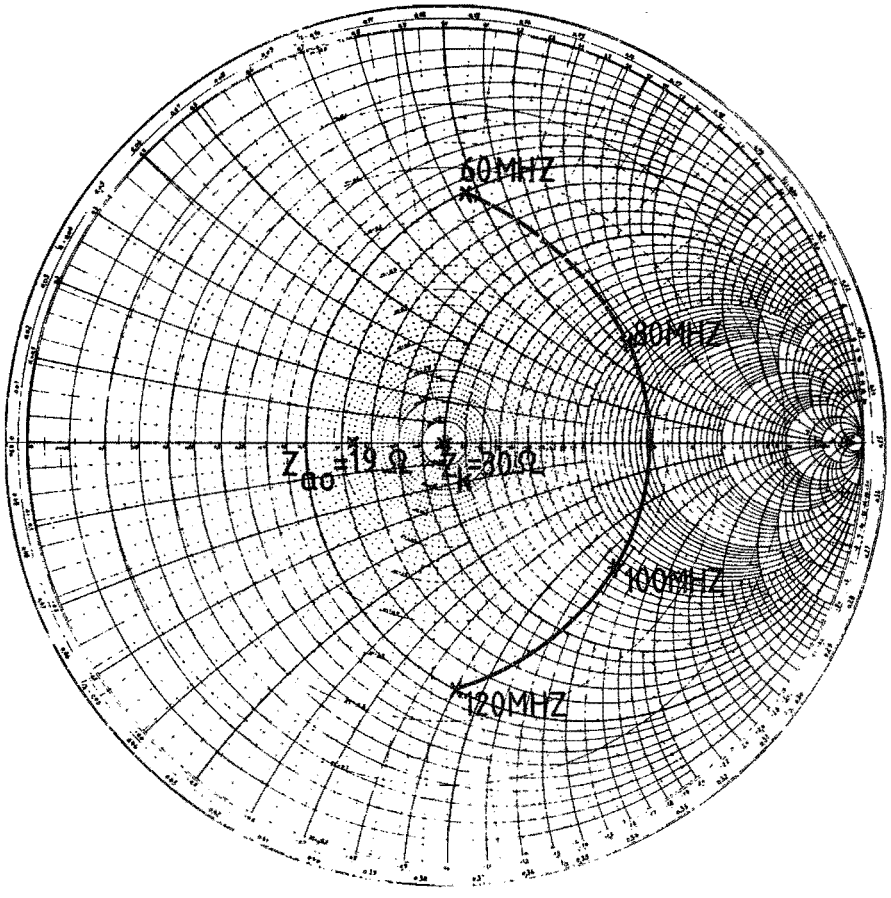

FIG 5.2

ANTENNA INPUT IMPEDANCE

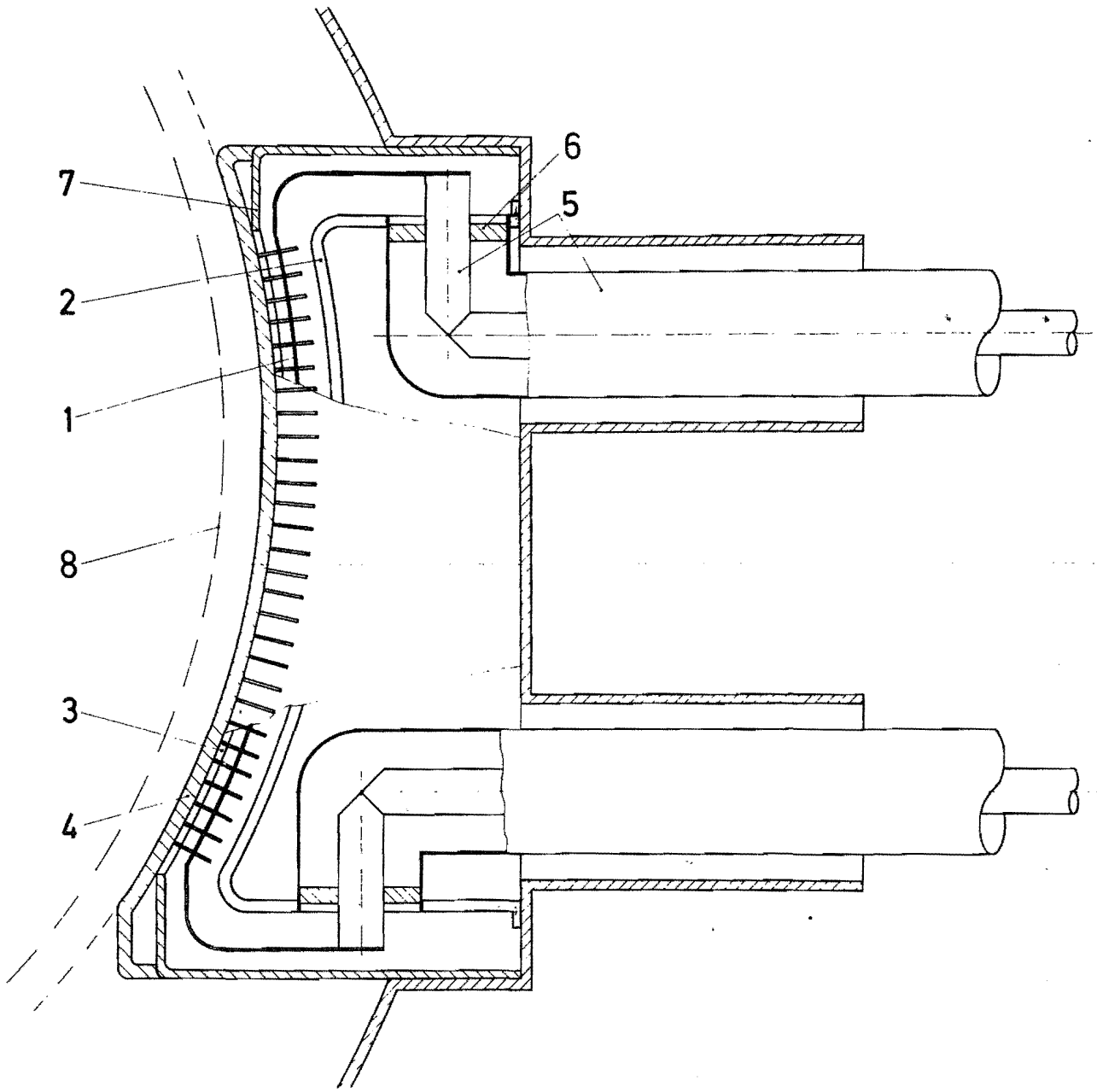

Fig.5.3 Schematic view of an ICRH antenna for ASDEX UG (single null operation)

1 central conductor	5 coaxial feeder
2 return conductor	6 support
3 Faraday screen	7 antenna casing
4 antenna limiter	8 separatrix

6. The Periphery of the Tokamak System

6.1 Building and Radiation Shielding

ASDEX UG is envisaged to be located in the southern part of IPP's experiment hall L6. The total area available is approximately 1500 m^2. Within the rectangular radiation shield 600 m^2 are planned to accommodate the tokamak system. The useful height of the hall is 10 m at present. This will be increased to 13 m by lowering the floor.

The dimensions of the radiation shield have not yet been finally determined. For shielding the X-rays, a concrete wall of 1 m thickness is sufficient. In the case of D-D operation at maximum parameters, both a wall and a ceiling, each 2.1 m thick, also made of concrete, will be necessary.

The foundations of the tokamak system and the radiation shield will be integrated into a plane floor plate. This plate will also bear the supporting structure of the diagnostics platform. Oscillation damping will be taken care of by a special design.

On the area of 1500 m^2 mentioned above, the following installations have to be accommodated besides the experiment itself: monitoring and control facilities, diagnostics, computers, cooling systems and switch gears.

The time estimated to perform the modifications of the experiment hall is 4 to 6 months. The work can be carried out without disturbing the operation of ASDEX which is situated some 50 m away from the future ASDEX UG experiment.

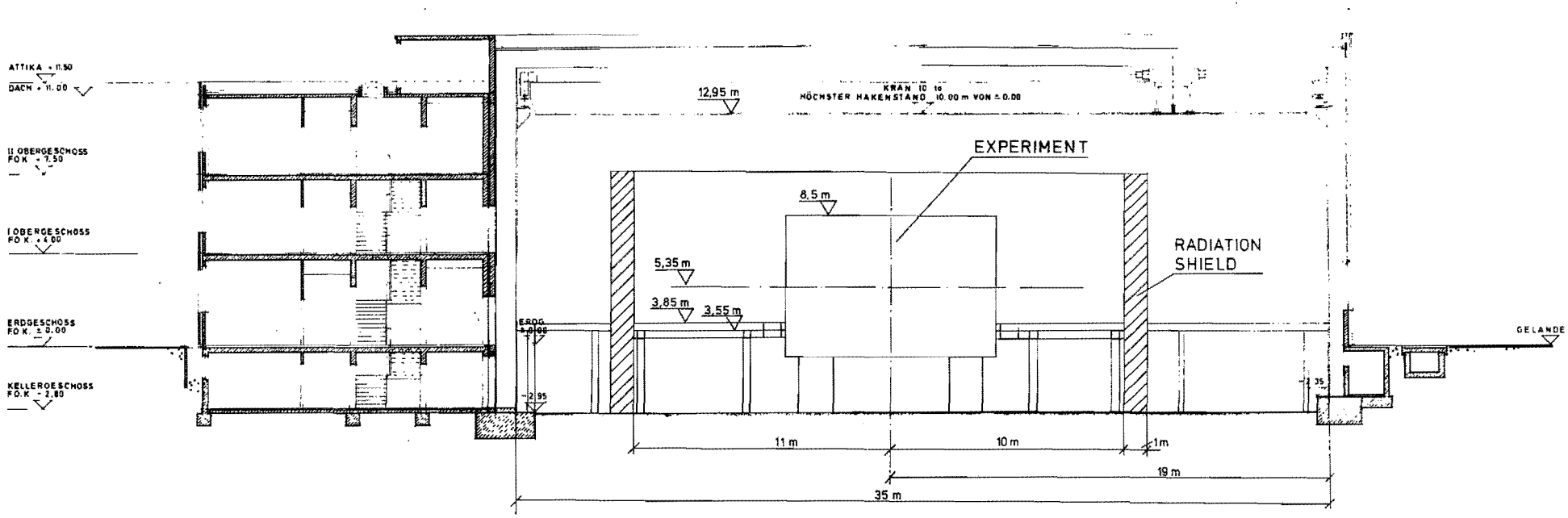

Fig. 6.1.1 Vertical Cut View of Experiment Hall L6

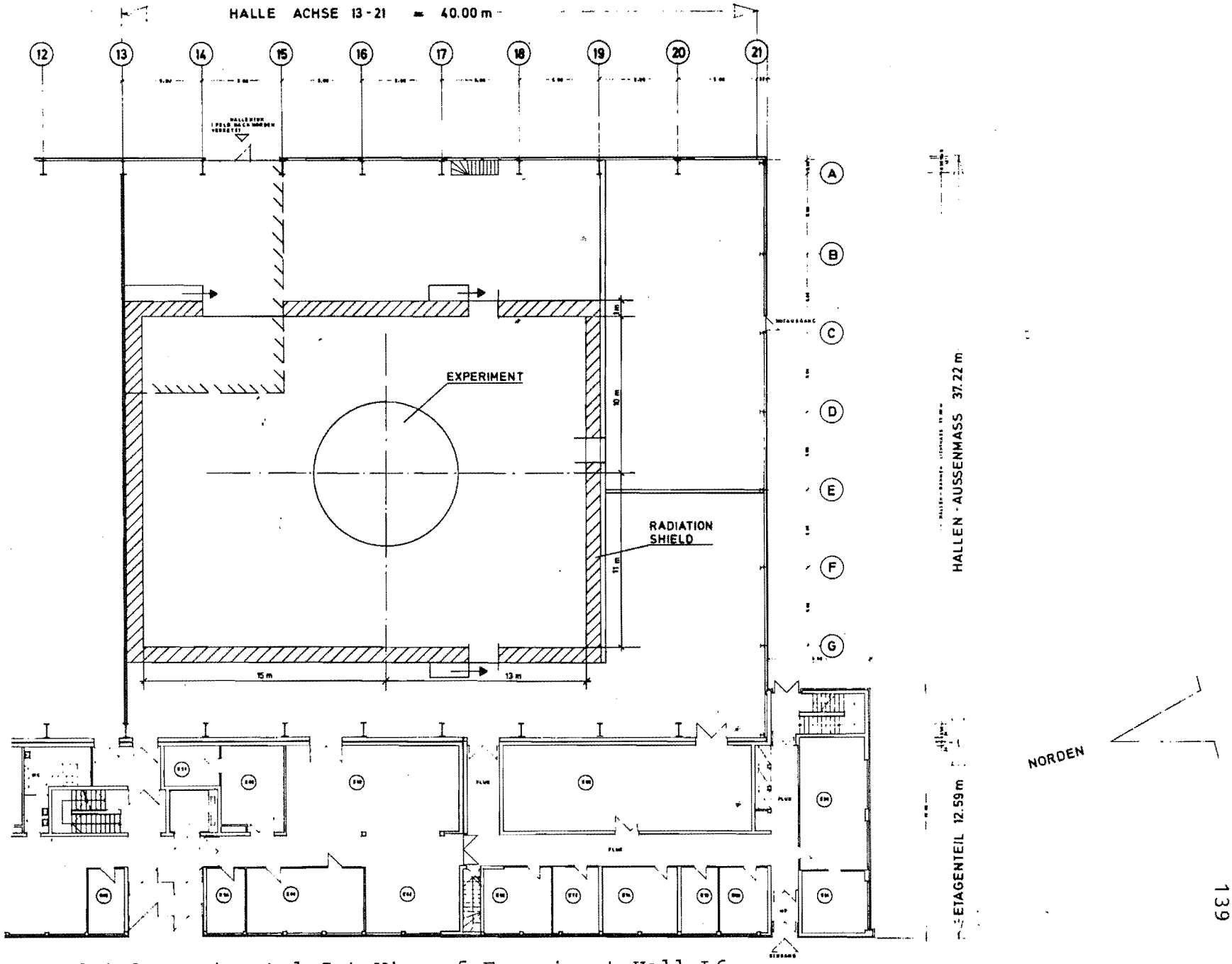

Fig. 6.1.2 Horizontal Cut View of Experiment Hall L6

7. Accompanying Theoretical Programme

To make maximum use of ASDEX UG results for extrapolation to NET and other future reactor designs, models and numerical codes for their interpretation have to be developed. Early availability of these theoretical tools will also help to apply the experience gained on ASDEX to an optimized design of the detailed geometry of the divertor region of ASDEX UG, to the selection of the necessary diagnostic methods and to the layout of the experimental programme.

Following the principal aims of ASDEX UG, the emphasis of this work is on understanding and modelling the action of divertors and pump limiters. However, also in three other points the outcome of these combined theoretical and experimental studies is expected to determine the ASDEX UG programme. They concern the physical problems of

- helium pumping
- deep hydrogen refuelling
- current drive,

and thus the possible need for helium injection, pellet injection and lower hybrid equipment.

7.1 Divertor and Pump Limiter Modelling

Aim of our development work in this area is the capability for a two-dimensional description of the hydrogen and impurity plasma dynamics in the scrape-off, linked to transport models for the bulk plasma, and to the correct boundary condition on target plates or walls. This plasma model has to be complemented by a Monte Carlo code for the neutral dynamics of hydrogen and impurity atoms and molecules, which - because of the geometry (e.g. of the pumping ducts) and the lack of the homogenizing effect of the magnetic field - has to allow even for three-dimensional variations.

In the following we first give a brief survey of the codes presently available to us (through own development work, or as contributed from other laboratories) and of their principle achievements to date, to be followed by an outline of our future development work.

Plasma boundary modelling codes available at IPP:

(a) 1-D electrostatic Monte Carlo code: solves electron and hydrogen ion single particle equations of motion in given, homogeneous magnetic field of arbitrary orientation and in electric fields computed self-consistently from Poisson's equation.

Achievements: clarification of structure of electrostatic sheath in front of material walls for oblique incidence of field lines, including effects of secondary electron emission. Resulting angular and energy distribution for hydrogen ions have also been used for evaluation of expected, averaged sputtering yield. The model was also applied to study dynamics in a collision-free ionization zone in front of walls.

(b) 1-D fluid model for plasma dynamics parallel to B: solves continuity, momentum and separate electron and ion energy equations including finite electron and ion heat conductivity and neutral-plasma interaction terms (ionization, CX energy and momentum exchange, radiation and dissociation energy losses).

Achievements: explanation of low Mach number flow and large parallel temperature gradients observed in ASDEX. (In combination with a strongly simplified model for the neutral particle household of the divertor): prediction of three regimes of divertor recycling - including the so-called energy flow limited regime - also found in experiments.

(c) 1-D multi-fluid model for impurity transport parallel to field lines: The continuity and momentum equations are solved for the frictional flow of the different ionization stages of an impurity in the hydrogen-plasma background computed by the code described above. Also included are ionization and recombination, the effects of the thermoelectric and the ambipolar acceleration fields and the thermal forces arising from the electron and ion temperature gradients of the background plasma.

Achievements: Outline the role of impurity - hydrogen ion friction in determining the impact energy of impurity ions at the target plates. Quantitative assessment of the conditions for formation of self-sputtering impurity avalanches, taking into account the difference in ionization state at the electrostatic sheath entrance between impurities diffusing out of the bulk plasma and those produced by sputtering at the target plates. Demonstrate the importance of the thermal forces onto impurities arising from temperature gradients of the background

plasma for the impurity flow in the scrape-off.

(d) BALDUR-code (developed by PPPL) for the plasma transport perpendicular to the flux surfaces, extended by us through inclusion of plasma-wall interaction models and finite rate description of the impurity ionization stages.

Achievements at IPP: Clarification of necessary conditions for formation of a protective radiation layer in the outer plasma layer. Demonstrate impossibility of producing such radiation layers with low-Z impurities in fusion plasmas (even taking into account non-coronal effects).

(e) 2-D model for hydrogen-plasma dynamics in the scrape-off layer. Parallel plasma flow and energy transport as in model (b) combined with perpendicular particle diffusion and electron and ion heat conduction.

Status: Comparison test runs with similar code - though independently developed and differently implemented - by P. Braams, showing good agreement.

(f) DEGAS - a two or three-dimensional Monte Carlo code for the dynamics of neutral molecules and atoms (developed by PPPL) including the interaction with walls and with a given plasma.

Status at IPP: The ASDEX divertor geometry has been set up in the code and stand-alone calculations for the hydrogen and helium gas dynamics in the target chamber have been carried out for pre-set plasma conditions.

Planned extensions:

(a) Combined neutral particle - plasma scrape-off calculations. The available 1-D scrape-off plasma code (case (b) of previous section) will be combined with DEGAS. Immediate aim is the quantitative simulation of the ASDEX scrape-off dynamics, using redundancies in the available experimental information (neutral pressure measurements and scrape-off density and temperature measurements at different positions along the field lines) to determine also unknown wall properties.

(b) Extension of the 2-D plasma scrape-off plasma model. At present calculations are done in a rectangle; the code will be converted to the true scrape-off geometry. Fundamental theoretical work is needed to clarify the connection between anomalous diffusion coefficients and

the components of the electrical conductivity tensor, as well as the need of concurrent solution of an equation for the two-dimensional current distribution in the scrape-off.

(c) 2-D impurity transport model. Extension of the 1-D finite rate impurity transport models to a 2-D situation are planned to study impurity transport in the scrape-off and also in certain situations in the bulk plasma, where two-dimensional effects are to be expected (e.g. impurity injection experiments or neutral injection - induced CX recombination).

7.2 Helium Pumping

Investigations spurred by the INTOR study have shown this to be a crucial and far from trivial problem. Besides the obvious particularity , that in a fusion reactor helium will have a source in the center, the lack of charge exchange, the high ionization energy, and its relatively low mass combine to make its recycling behaviour different from both that of any other impurity and of hydrogen. Monte Carlo calculations with the DEGAS code indicate that these differences will play a much more decisive role in an open divertor case than in a geometry like ASDEX, where the smallness of the entrance slits alone ensures already a high helium compression ratio. Recent investigations of the impurity dynamics in the scrape-off have, furthermore, shown that in addition to the friction force exerted by the hydrogen plasma flow, thermal forces arising from temperature gradients can have a comparative and opposing effect, retarding thereby the helium ion flow into the pumping chamber.

These theoretical results underline the necessity of quantitative experiments on ASDEX UG to form a basis for NET. The principal problem in any related experiment consists in determining the helium ion content in the bulk plasma. Further studies will have to show, whether this number can be determined with sufficient accuracy from global balances and measurements of the neutral helium pressures, whether the helium behaviour can be simulated by using the better diagnoseable neon, whether significant information about α-particle transport could be derived from the injection of fast neutral helium atoms, and to what extent special diagnostic methods need to be developed.

7.3 Pellet Refuelling

Even for only modest reduction of the hydrogen recycling rate below 1, plasma density profiles and - in a reactor - the ratio between hydrogen to helium pressure in the pumping chamber can be significantly affected by depositing part of the refuelling flux deep in the plasma.

Pellet refuelling would also be a necessary for a low-density, high-temperature scrape-off layer regime, which is presently considered less promising than the high density plasma boundary. In this alternative regime, most of the particles diffusing out of the bulk plasma are assumed to be trapped in the target chamber and ultimately pumped. In combination with deep refuelling of the hydrogen, it is thus hoped to suppress CX sputtering, and to reduce - for a given plasma density - the absolute magnitude of the particle flux that has to be pumped.

Pellet injection might finally also be a powerful method to extend the presently observed density limit in tokamaks, in case this turns out to be linked to the recycling fluxes in the boundary zone or in any other way to the plasma boundary density: keeping the latter parameters constant, pellet refuelling would allow to raise the peak and average plasma densities.

It is presently not decided whether any of these arguments will finally lead to the use of pellet injectors in a reactor, although most of the beneficial effects could already be obtained with a fairly shallow penetration depth of pellets, which only needs to be raised by a significant factor over the gas-puff refuelling length. A still open question is also whether pellet ablation results in effective in-situ ionization of the ablated atoms, or gives rise to a significant fraction of fast CX neutrals. In the latter case, suppression of CX sputtering would obviously require a deeper pellet penetration.

Adoption of pellet injection on ASDEX UG and selection of injector parameters thus still depends on results of further experimental and theoretical work. Experiments are proceeding on ASDEX; on the theoretical side the BALDUR transport code has been extended to allow an arbitrary fraction of the ablated hydrogen atoms to be started as neutrals.

Pellet injection has also shown to be a powerful tool for active plasma diagnostics.

7.4 Current Drive

Non-inductive current drive, considered to be essential for extending the tokamak reactor pulse length beyond the 1000 sec range, will be studied already on ASDEX and TORE-2, using lower hybrid waves. Most of the basic physics issues currently under investigation (origin and parameter dependence of the observed density limit; explanation for the 'filling up' of the electron distribution in the region below the nominal phase velocity of the injected lower hybrid wave) will presumably be clarified by the time of coming into operation of ASDEX UG.

However, even below the density limit, the observed current drive efficiencies as reported at the Baltimore conference, follow the relation

$$I_{p,LH} \lesssim 10^{19} \frac{P_{LH}}{n_e R} \quad [\mathrm{m.k.s.A}]$$

which, after insertion of the nominal INTOR values, would predict a continuous LH power requirement of nearly 600 MW.

The presently most realistic scenarios therefore involve a cyclic variation in the plasma density, with the low density phase used to drive the plasma current by LH against an externally applied electric field. This is, of course, equivalent to a re-charging of the OH transformer coil (utilizing also of that part of the storable flux which during the first cycle is required to cover the inductive flux consumption of the plasma), which can subsequently be used for a conventional, inductive drive of the plasma current in the operation - density phase. (As the dependence on plasma density is common also to other current drive methods (e.g. N.I.), such scenarios, possibly involving also cyclic variations in the Z_{eff}, are of quite universal interest.)

Basic requirements on the tokamak system for a proof of the principle of such scenarios are a very long pulse duration at somewhat reduced parameters, and the capability for cyclic density variation as inherent in a divertor device.

Evaluation of the above expression for the efficiency shows that a LH power of approximately 3 MW should suffice to drive a plasma current of 800 kA even for densities up to $2 \times 10^{19}\ m^{-3}$. This current would correspond (at $q = 3$) to a magnetic field requirement of 1.8 T, and all three parameters (heating power, plasma current and B_t) are consistent with D.C. operation of the ASDEX UG tokamak system.

Further details, particularly of the current drive system, will depend, of course, on the outcome of the experiments on ASDEX and elsewhere, and results of the theoretical effort also in course at IPP.

8. Survey of Diagnostics

The survey of diagnostics as given below served up to now exclusively two purposes: firstly to ajust the tokamak system design to diagnostic needs and secondly to activate possible support by other experienced laboratories for development and application of special diagnostics on ASDEX UG.

The diagnostics for ASDEX UG can be divided into two categories:
- investigation of the bulk plasma;
- investigation of the boundary layer and divertor region.

A survey over both areas is given by the following two tables. Nearly all diagnostic methods are well proven, although some of them need development or adjustment to be applied in ASDEX UG. The tokamak system, in particular the vacuum vessel, has been designed compatible with the requirements of these diagnostics. This is indicated by denoting the location of the single diagnostic method in the tables. (Names of the ports see Fig. 8.1.) As an example the arrangements of Thomson scattering for measurement of T_e - and n_e - profiles are shown in Figs. 8.2 and 8.3.

The total amount of data which have to be acquired and handled for the quoted diagnostic amounts to 10 M bytes per discharge (i.e. 5×10^6 real numbers).

The diagnostics enumerated below is sufficient and capable in order to investigate the physical problems and aims of ASDEX UG.

Table I: Plasma bulk diagnostics (A)
(larger development required yes = Y, no = N)

	Quantity to be measured	Diagnostics		Location
A 1	Current	Induction probes		Inner Wall of the vacuum vessel
A 2	Loop Voltage	voltage loops		
A 3	MHD activities	small probes		
A 5	Electron density	microwave interferometry	N	inner wall of the vacuum vessel
A 6		FIR interferometry	Y	7 (EO/EU+DO/DU)
A 7		Thomson scattering	Y	13(DO/DU+EO/EU,A)
A 7	Electron temperature	Thomson scattering	N	
A 8		ELECTRON CYclotron emission	N	3 A
A 9	Ion temperature	charge exchange neutrals	Y	1 (GO + A)
A10		VUV-/ soft X-ray spectroscopy	N/Y	9 (A + CO)
A11				
A12		neutron diagn.	N	outside of torus
A13	total radiation	bolometer cameras	Y	5 (A + CC + CU)
A14		soft x-ray cameras	Y	
A15		hard x-ray detectors	N	11 A
A16	gross overview	photographic diagnostic (visible region)	N	2 (CC + CU)
A17		IR-TV camera	N	3 (CO + CU)

A18	transport of particles	pellet injection	Y	15 A
A19	energy deposition and transport	FIR collective Thomson scattering (fluctuations)	Y	7 (A + CU)
A2		microwave scattering	N	inner wall of the vacuum vessel

Table II: Diagnostics for boundary and divertor region (B)

	Quantity to measured	Diagnostics		Location
B 1	electron density & temp.	Langmuir probes	Y	fast moving
B 2		microwave interferometry	N	inside vacuum vessel
B 3		Thomson scattering		13 (Co/Cu) SEE ALSO A 7
B 4		lithium beam diagnostics	Y	
B 5	ion temperature	charge exchange neutrals	N	16 (Co+Cu) 11 (Co+Cu)
B6	impurity atoms and ions	spectroscopy	N	15 Cu
B 7		laser fluoresc. spectroscopy	Y	9 (Eo/Fo + Cu)
B 8	neutral hydrogen	spectroscopy of H, H2	N	
B 9		fluorescence/absorption of Lyα /Hα	Y	7 Co 3 (Eo+Eu)
B 5		Charge exchange neutrals		
B10	divert.plates heat shield	thermography	N	3 A
B11		thermo couples	N	mounted on div. plates

B12		divertor plate probes	Y	13 (FU)
B13	plasma-wall interaction	wall probes	N	inner wall of vacuum vessel
B14		vacuum ports	Y	14 (Cu+Co)
B15		removable parts of divert.plates	Y	13 Fo
B16	gas pressure in divertor	pressure probes	N	no separate port
B17		quadrupole mass SPECTROMETER	N	no separate PORT

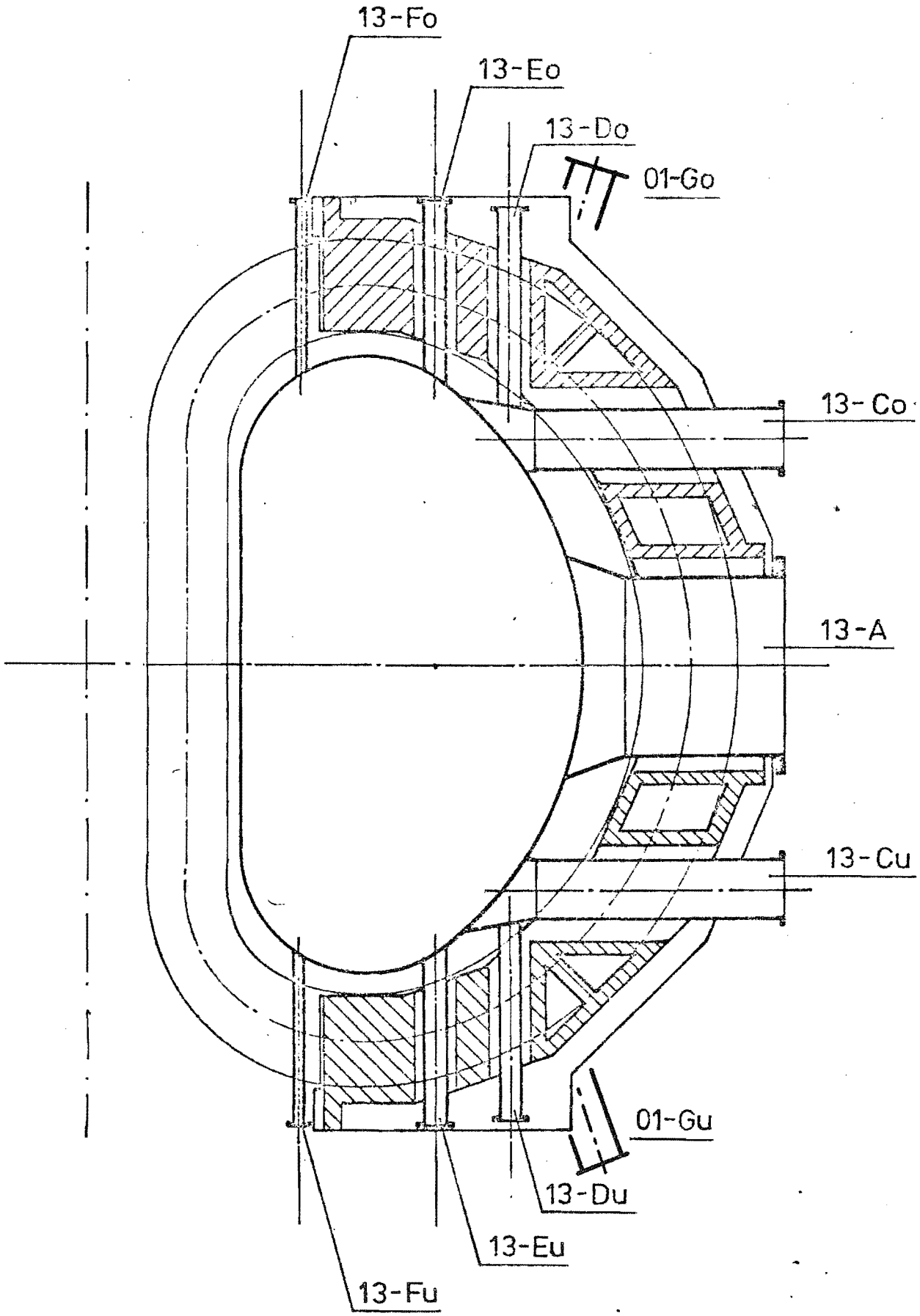

Fig. 8.1 Names of the diagnostic ports used in the table. Numbers indicate the toroidal plane

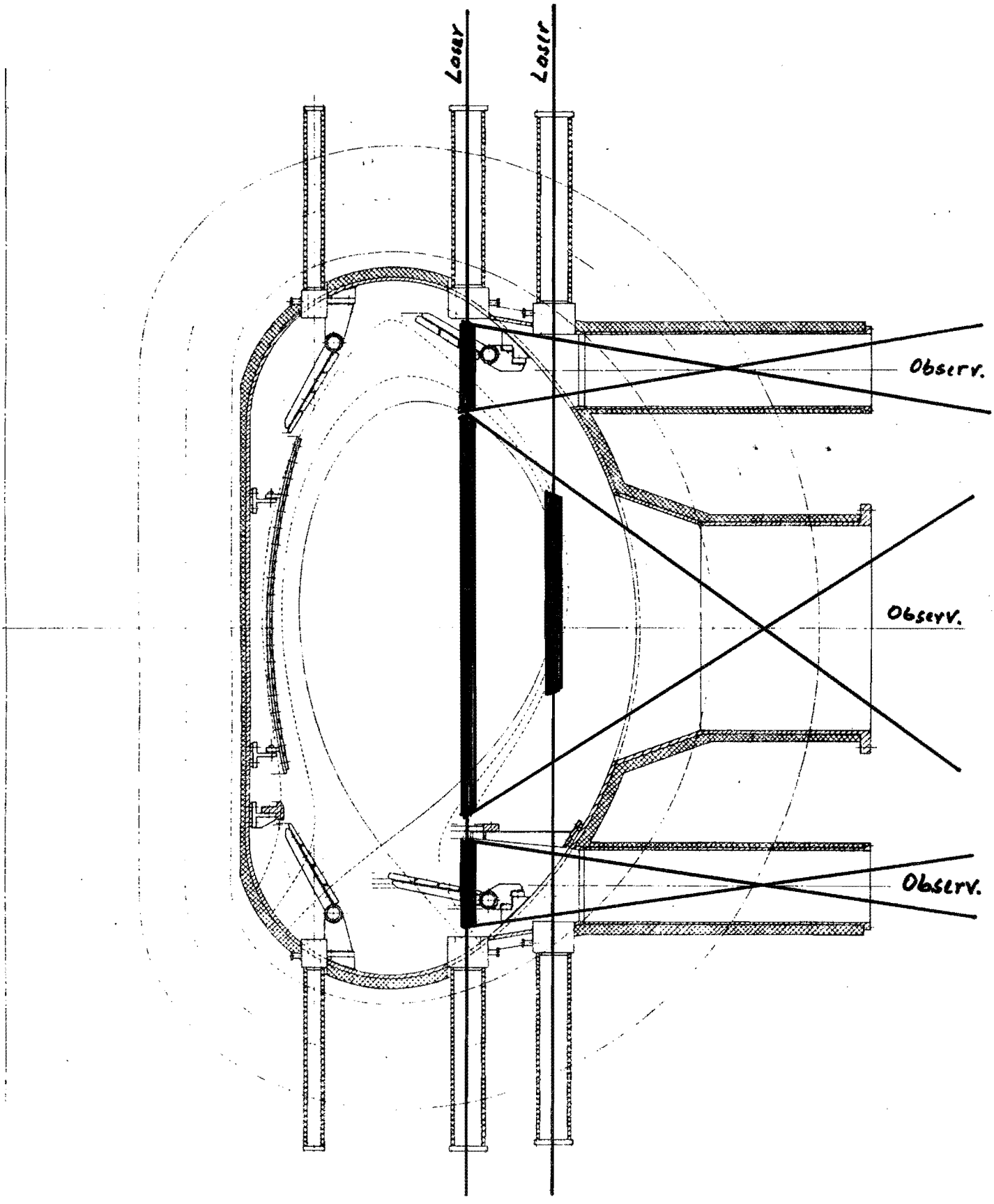

Fig. 8.2 Example for measurement of vertical profiles of electron temperature and density

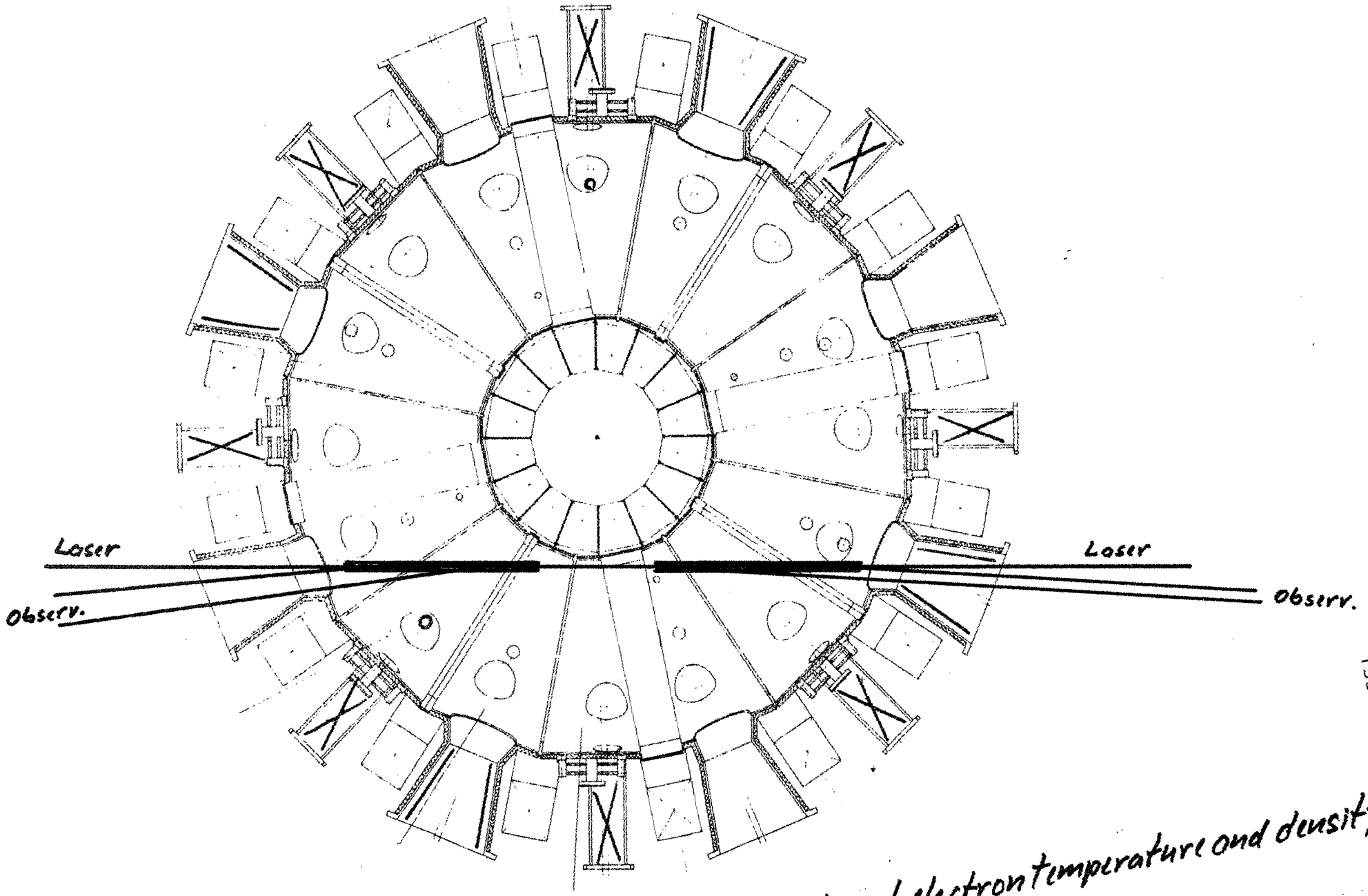

Fig. 8.3

... for measurement of horizontal profiles of electron temperature and density

9. Control, Data Acquisition and Data Handling

The control and safety system of the tokamak machine and components shall be as direct and redundant as possible and with the least interlinkage with the data processing system. Diagnostic data required for (feedback) control shall be fed into two channels, one serving the control input, the other the data acquisition system. The control and safety concept shall be conceptually worked out by an experienced industrial company.

The data acquisition and handling system is presently designed by the IPP computer centre supported by experts from ASDEX and W VII. It has to handle up to 10 Mbytes from 30 diagnostics for each discharge. The present concept foresees essentially a two-stage system. The first stage located at the experiment provides each diagnostic with adequate processing modules (e.g. CAMAC Crates) for data reception, ordering, reduction and evaluation by minor computations. Each module is equipped with adequate computing facility , terminal and display, and eventually with plotting facility. Limited storage will also be provided.

All raw data are transferred by fast transfer lines to the computer centre (second stage), where the data are ordered, stored and evaluated by larger programmes and filed, the majority within the 5 to 10 min intervals between discharges. For this purpose a powerful computer (Siemens 7.880) is available.

Each terminal at each diagnostic processing module allows to communicate with the local computer as well as with the central computer. Timing, triggering and all necessary control, including automatic control, has to be provided there. Each diagnostic processing module should be capable of working independently from any other diagnostic module or any other computer, and eventually independently from the tokamak operation.

One sufficiently simple and well documented software system shall be provided which applies to each processing module and local computer as well as to the central computer. The data file system has certainly to cover all diagnostic settings, timing and gauge factors.